

Investigation of electrical stimulation of the optic nerve for artificial vision

Présentée le 18 juin 2021

Faculté des sciences et techniques de l'ingénieur
Chaire Medtronic en Neuroingénierie
Programme doctoral en génie électrique

pour l'obtention du grade de Docteur ès Sciences

par

Vivien GAILLET

Acceptée sur proposition du jury

Prof. D. N. A. Van De Ville, président du jury
Prof. D. Ghezzi, directeur de thèse
Prof. M. Capogrosso, rapporteur
Prof. E. Fernández Jover, rapporteur
Prof. M. Herzog, rapporteur

“They can cut all the flowers, but they cannot stop the coming of Spring.”

Pablo Neruda

Aknowledgments

First of all, I would like to thank my thesis supervisor Diego Ghezzi for welcoming me into his lab and for his unflinching determination throughout this whole project. I also would like to thank my thesis defense committee for taking the time to read and evaluate my thesis.

To my colleagues of the LNE, I feel really lucky to have met and worked with such a wonderful group of people; I could not have wished for better colleagues! Then to the many students I supervised during my thesis; your help was instrumental in bringing this project so far, I would have achieved much less without it.

Of course, my life would definitely be less fun and interesting without my long-time groups of friends from la Broye and Ouest de Lausanne; thanks for reminding me there is more to life than work, and may our friendships last a lifetime!

I am also thankful for the unconditional support of my parents throughout my whole life, and to my brother Christophe for always being available to hang out with me when I need it. They say you can't choose your family, but I would not change it for anything in the world.

And finally, I am convinced I could not have gotten where I am in life without Julie to both support me through the bad times and be there to celebrate the good ones with me. Thank you for being such an incredibly kind and caring life partner.

Résumé

Grâce à de récentes avancées technologiques en micro-électronique et en bio-ingénierie, il est désormais possible de restaurer des perceptions sensorielles perdues ou défectueuses en interférant le système nerveux avec des appareils électroniques. Le but étant d'ainsi reproduire artificiellement l'encodage électrique des signaux neuronaux des organes ou tissus sensoriels manquants ou défectueux, comme en témoigne le développement des implants cochléaires permettant la restauration de l'audition chez les patients sourds. Cela rend le traitement de la cécité, une condition très handicapante qui diminue grandement la qualité de vie des personnes qui en souffrent, un but concret envisageable aujourd'hui, et ainsi de nombreux groupes tentent actuellement d'appliquer le même principe des implants cochléaires à la restauration de la vue. Jusqu'à présent, l'approche privilégiée a été les implants rétiniens en raison de leur proximité avec les cellules défectueuses, les photorécepteurs, minimisant ainsi la quantité d'encodage du signal neuronal qui doit être reproduite, et en raison du nombre raisonnable de sites de stimulation que la rétine peut accueillir.

Plusieurs prototypes ont déjà démontré la possibilité de restaurer un certain degré de vision fonctionnelle, quoiqu'encore très rudimentaire à ce stade. Cependant, contrairement à l'ouïe, la vue est sens extrêmement complexe, impliquant plusieurs types cellulaires formant des circuits très élaborés, ce qui rend les avantages des implants rétiniens moins flagrant, rendant des approches alternatives telles que des prothèses du nerf optique ou du cortex visuel intéressante à explorer. Nous pensons que la stimulation électrique du nerf optique est une approche attractive pour plusieurs raisons ; tout d'abord, elle ne nécessite pas de que l'œil soit transparent. Deuxièmement, elle peut traiter certaines conditions telles que les traumatismes oculaires ou le décollement de la rétine que les implants rétiniens ne peuvent pas traiter. Enfin, grâce à l'organisation des axones du nerf optique, elle devrait vraisemblablement uniquement stimuler des axones provenant de la même région du champ visuel, ce qui n'est pas le cas avec les implants épirétiniens ; en effet ils sont connus pour stimuler de façon indésirable des axones qui passent au-dessus des noyaux cellulaires qu'ils ciblent, produisant ainsi des phosphènes incurvés et allongés limitant la résolution maximale atteignable par l'implant.

Dans cette thèse, nous présentons un nouveau design d'électrodes intraneurales, l'OpticSELINE, qui vise à améliorer la sélectivité et la stabilité des « électrodes-manchons » extra-neurales précédemment utilisées dans la stimulation du nerf optique. Nous avons d'abord caractérisé l'amélioration des propriétés mécaniques et électriques de l'électrode, puis procédé à l'évaluation de sa capacité de stimulation in vivo chez le lapin. En parallèle de montrer qu'il est possible de moduler l'amplitude de l'activation corticale en augmentant ou diminuant l'amplitude du courant stimulant, nous avons implémenté un modèle hybride utilisant la méthode des éléments finis pour estimer les dimensions des portions du nerf optique activées par les protocoles de stimulation électrique que nous utilisons. A l'aide d'une analyse en composantes indépendantes, nous avons mis en place un protocole permettant d'isoler les composants du signal liés sélectivement à une seule ou à une paire d'électrodes de stimulation. Nous nous sommes ensuite concentrés sur le développement de nouveaux algorithmes plus avancés pour analyser les différents motifs d'activation corticale. Nous avons d'abord développé un classificateur basé sur une machine à vecteurs de support qui nous a permis d'identifier avec précision à la fois le stimulus visuel ou l'électrode de stimulation qui à l'origine d'un motif donné d'activation corticale parmi un total de respectivement dix et huit stimuli potentiel. Enfin, nous avons développé un modèle de régression qui nous a également permis de prédire avec précision à la fois le stimulus visuel ou l'électrode de stimulation, sans avoir rencontré au préalable les motifs d'activation corticaux sur

lesquels il a été testé durant sa phase d'entraînement, ce qui permet d'avoir une capacité d'extrapolation améliorée par rapport au classificateur.

Dans l'ensemble, les travaux présentés dans cette thèse mettent en évidence de nouvelles stratégies complémentaires abordant différents aspects du développement d'une neuroprothèse visuelle basée sur la stimulation du nerf optique, qui, nous l'espérons, conduiront à une exploration plus approfondie de cette approche et la rapprochant d'un emploi clinique.

Mots-clés

Stimulation Électrique · Nerf Optique · Électrode Intraneural · Neuroprothèse Visuelle · Vision Artificielle · Électroencéphalographie Intracrânienne · Analyse en Composantes Indépendantes · Modèle Hybride · Régression Linéaire · Stimulation Visuel

Abstract

Thanks to recent technological advances in microelectronics and bioengineering, it is now possible to restore lost or impaired sensory modalities by interfering the nervous system with electronic devices and artificially reproducing the electrical encoding of the neural signals of the missing or defective sensory organs or tissues, as evidenced by the successful development of cochlear implants allow the restoration of hearing in deaf patients. This makes the treatment of blindness, a very impairing condition that significantly decreases the quality of life of the person it affects, a plausible possibility today, and many groups are currently attempting to apply the same principle of cochlear implants to sight restoration. So far, the preferred approach has been retinal implants due to their proximity to the defective cells, the photoreceptors, which minimizes the amount of processing of the neural signal that needs to be reproduced, and due to the reasonable number of stimulating sites that the retina can accommodate. Several devices have already demonstrated the possibility of restoring some degree of functional vision, albeit still very rudimentary. However, unlike hearing, vision is an extremely complex sensory modality, involving several cell types forming elaborate circuitry, which makes the advantages of retinal implants less definitive, and other alternative approaches such as optic nerve or cortical prosthesis still worth exploring. We believe the optic nerve stimulation is an attractive approach for several reasons; firstly, it does not require optical transparency. Secondly, it can address specific conditions such as severe eye trauma or retinal detachment where retinal implants cannot be employed. Finally, thanks to the organization of the optic nerve axonal fibers, it may likely result in the activation of axons originating from the same region of the visual field. This is not the case with epiretinal implants, which have been reported to stimulate undesired axons of passage in addition to the somas of their cellular targets, resulting in curved and elongated phosphenes that limit the implant's achievable resolution.

In this thesis, we introduce a novel intraneural electrode design, the OpticSELINE, which aims at improving the selectivity and stability of the extra-neural cuff-electrodes previously used in optic nerve stimulation. We first characterized the device's improved mechanical and electrical properties and then proceeded to evaluate its stimulation capacity *in vivo* in the rabbit. In parallel to demonstrating the ability to modulate the magnitude of the cortical activation through the increase or decrease of the stimulation current, we implemented a hybrid finite element computational model to estimate the dimensions of the nerve portions activated by our electrical stimulation protocols. Using independent component analysis (ICA), we also developed a workflow that allows isolating components of the signal selectively related to a single or a pair of stimulating electrodes. We then focused on the development of new and improved algorithms to analyze the cortical activation patterns. We first developed a support machine vector (SVM)-based classifier that allowed us to accurately identify both the visual stimulus or the stimulating electrode that elicited a given cortical activation pattern amongst ten and eight total potential stimuli. Finally, we developed a regression model that also allowed us to accurately predict both the visual stimulus or the stimulating electrode, without having encountered the cortical activation patterns it was tested on during its training phase, resulting in an improved extrapolation capacity compared to the classifier.

Altogether, the work presented in this thesis highlights novel complementary strategies to tackle different aspects of the development of an optic nerve-based visual neuroprosthesis, which hopefully will lead to a more in-depth investigation of this approach and eventually bring it a step forward to clinical applications.

Keywords

Electrical stimulation · Optic Nerve · Intra-neural Electrode · Visual Neuroprosthesis · Artificial Vision · Electro-corticography · Independent Component Analysis · Hybrid Model · Linear Regression · Visual Stimulation

Contents

Aknowledgments	ii
Résumé	iii
Mots-clés	iv
Abstract	v
Keywords	vi
List of Figures	x
List of Equations	12
List of Abbreviations	13
Chapter 1 Introduction	15
1.1 The visual system	15
1.1.1 Anatomy of the eye	15
1.1.2 The retina	16
1.1.3 The optic nerve, the optic chiasma, and optic tract.....	21
1.1.4 The lateral geniculate nucleus and the optic radiations	24
1.1.5 The primary visual cortex.....	25
1.2 Blindness and retinal dystrophies	26
1.2.1 Blindness	26
1.2.2 Age-related macular degeneration and retinitis pigmentosa.....	27
1.3 Visual Neuroprostheses	29
1.3.1 Definition and principle.....	29
1.3.2 Retinal implants.....	32
1.3.3 Optic nerve implants.....	34
1.3.4 Lateral geniculate nucleus prostheses	36
1.3.5 Cortical prostheses	36
1.3.6 Overview of interfaces for neural stimulation.....	37
1.4 Thesis motivations and organization	39
Chapter 2 Spatially selective activation of the visual cortex via intraneural stimulation of the optic nerve 41	

2.1	Abstract	41
2.2	Introduction	41
2.3	Results	42
2.3.1	Electrode array design and characterization	42
2.3.2	Visual stimulation	45
2.3.3	Electrical stimulation.....	46
2.3.4	Cortical activation maps.....	48
2.3.5	Selectivity of optic-nerve stimulation	51
2.4	Discussion	53
2.4.1	Outlook	55
2.5	Methods	55
2.5.1	Electrode microfabrication.....	55
2.5.2	Electrochemical characterization.....	56
2.5.3	Mechanical tests.....	56
2.5.4	Animal handling and surgery.....	56
2.5.5	Optic-nerve anatomy	57
2.5.6	Electrophysiology.....	57
2.5.7	Blind source separation.....	58
2.5.8	Hybrid FEA model and NEURON simulation	59
2.5.9	Statistical analysis and graphical representation.....	60
2.6	Aknowledgent	60
2.7	Supplementary Material	61
Chapter 3 A machine-learning algorithm correctly classifies cortical evoked potentials from both natural retinal stimulation and electrical stimulation of the optic nerve		
70		
3.1	Abstract	70
3.2	Introduction	71
3.3	Material and Methods	73
3.3.1	Animal handling and surgery.....	73
3.3.2	Electrophysiological recording and stimulation.....	73
3.3.3	Signal processing and feature extraction	74
3.3.4	Classification and regression	74
3.4	Results	75
3.4.1	Patterned visual stimulation.....	75
3.4.2	Patterned electrical stimulation	80
3.5	Discussion	86
3.6	Conclusion	88
3.7	Aknowledgent	88
Chapter 4 Conclusion.....		
89		
4.1	Achieved results	89
4.2	Future developments	90

4.2.1	Mapping of the optic nerve.....	90
4.2.2	Assessment of the OpticSELINE position inside the optic nerve.....	91
4.2.3	Assessment of the ECoG array electrodes RFs.....	91
4.2.4	Alternative cortical activity recording methods	92
4.2.5	Machine learning algorithm improvement	93
4.2.6	Animal model	93
4.2.7	Increasing the number of stimulation sites.....	94
4.2.8	Field shaping stimulation strategies	94
4.3	Outlook	96
	References	97
	Curriculum Vitae	118

List of Figures

Figure 1-1 Overview of the human visual system.....	16
Figure 1-2 Photoreceptors anatomy and distribution	17
Figure 1-3 The three main parallel pathways.....	19
Figure 1-4 Receptive fields overview.....	20
Figure 1-5 Anatomy of the optic nerve	22
Figure 1-6 Optic nerve inner fibers organization.....	23
Figure 1-7 Overview of the primary visual cortex organization	26
Figure 1-8 Visual acuity definition	27
Figure 1-9 Age-related macular degeneration and retinitis pigmentosa.....	28
Figure 1-10 Principle of electrical stimulation.....	30
Figure 1-11 Visual neuroprosthesis principle and main elements	31
Figure 1-12 Anatomical targets for visual prostheses along the visual path.....	32
Figure 1-13 Summary of the studies on electrical stimulation of the optic nerve in humans.....	35
Figure 1-14 Different nerve interface for electrical stimulation	38
Figure 2-1 The intraneural electrode array OpticSELINE.....	43
Figure 2-2 Electrochemical and mechanical characterization.....	44
Figure 2-3 Visually evoked cortical potentials.....	45
Figure 2-4 Electrically evoked cortical potentials.....	46
Figure 2-5 Cortical activation maps.....	48
Figure 2-6 Distribution map of the independent components within the optic nerve	50
Figure 2-7 Probability activation map of the optic nerve	52
Figure 2-8 High-frequency stimulation of the optic nerve.....	53
Supplementary Figure 2-1.....	61
Supplementary Figure 2-2	62
Supplementary Figure 2-3	63
Supplementary Figure 2-4	64
Supplementary Figure 2-5	65
Supplementary Figure 2-6	66
Supplementary Figure 2-7	66
Supplementary Figure 2-8	67
Supplementary Figure 2-9	68

Supplementary Figure 2-10	68
Figure 3-1	76
Figure 3-2	78
Figure 3-3	79
Figure 3-4	81
Figure 3-5	82
Figure 3-6	84
Figure 3-7	85
Figure 3-8	86
Figure 4-1	92
Figure 4-2	95

List of Equations

Equation 2:1 Laplace formulation.	59
Equation 2:2 Dirichlet boundary conditions.	59

List of Abbreviations

AMD	Age-related macular degeneration	OPL	Outer plexiform layer
CNS	Central nervous system	PNS	Peripheral nervous system
ECoG	Electrocorticography	RF	Receptive field
EEP	Electrically-evoked potential	RGC	Retinal ganglion cell
FEA	Finite element method	RMSE	Root mean squared error
FINE	Flat interface neural electrode	RNFL	Retinal nerve fiber layer
ICA	Independent component analysis	RP	Retinitis pigmentosa
INL	Inner nuclear layer	RPE	Retinal pigmented epithelium
IPL	Inner plexiform layer	SELINE	Self-opening intraneural electrode
LGN	Lateral geniculate nucleus	TIME	Transverse intrafascicular multichannel electrodes
LIFE	Longitudinal intrafascicular electrodes	VEP	Visually-evoked potential
ONL	Outer nuclear layer		

Chapter 1 Introduction

In this introductory chapter, I will present concepts relevant to the understanding of the work done during my Ph.D., which goal is to explore the use of electrical stimulation of the optic nerve for artificial vision. In the first section of this chapter, I will describe the general organization of the visual system in order to introduce the different existing artificial vision approaches. In the second section of this chapter, I will briefly discuss two of the main conditions visual neuroprosthesis can address. Finally, in the last section, I will introduce the principle of electrical stimulation, and summarize the different approaches for artificial vision and discuss their specific advantages and drawbacks.

1.1 The visual system

The main anatomical structure of the human visual system that can be potential targets for artificial vision are the retinas, the optic nerves, the optic chiasma, the optic tracts, the lateral geniculate nuclei (LGNs), the optic radiations, and the primary visual cortices (V1), which together form the primary visual pathway. Each of them will be individually discussed in the next paragraphs (Figure 1-1a).

1.1.1 Anatomy of the eye

The human eye is a spherical structure of approximately 24 mm in diameter, filled with the vitreous, a clear gel-like substance that gives the eye its spherical shape¹. It is surrounded by the wall of the eye, which is formed by the sclera, the white outer protective layer of the eye. On the interior side of the sclera lays the choroid, the vasculature bed that delivers oxygen to the outer layer of the retina², which is made of thin layered sheets of nervous tissue covering the interior surface of the bottom three quarters of the eye in charge of converting incoming light rays into a neural signal³. In between the choroid and the retina is found the retinal pigmented epithelium (RPE). It is involved in the transport of nutrients toward the retina, the management of waste products discarded by the photoreceptor layer, and the recycling of compounds originating from the phototransduction cycle. It also plays a protective role by absorbing high-energy light and toxic oxygen reactive species(Figure 1-1b)^{4,5}.

The cornea is a curved and transparent tissue that is the first anatomical structure that incoming light rays traverse when entering the eye. It is responsible for most of the optical focusing that takes place in the eye³. After the cornea, the light rays travel through the anterior chamber, a space filled with aqueous humor. They then enter the pupil, the eye's aperture, which diameter can be modulated by the widening or tightening of the iris, the annular structure surrounding it, in order to control the amount of light entering the eye. Next, they traverse the lens, a convex and transparent structure which curvature can be increased by the tightening of the ciliary muscles to complete the focusing of the light rays originating from close objects on the retina when necessary³. Lastly, they travel through the interior bulk of the eye, filled with the vitreous humor, before finally reaching the retina (Figure 1-1b).

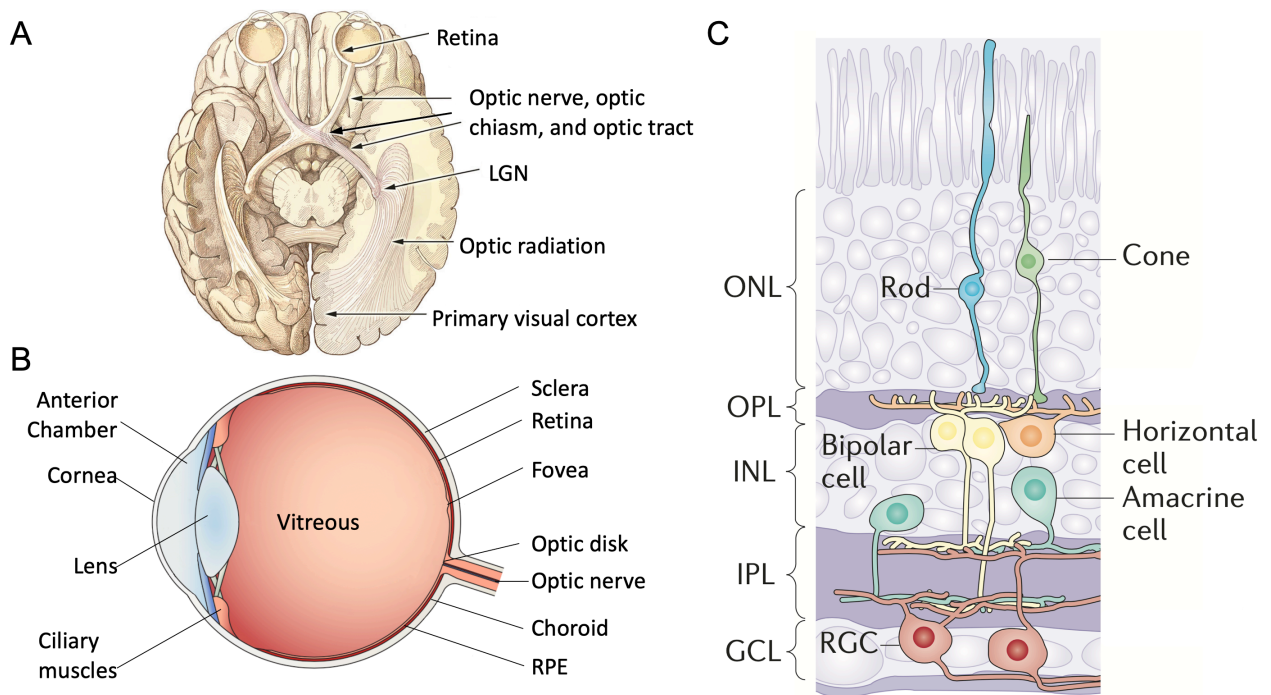


Figure 1-1 | Overview of the human visual system. (a) Horizontal cut of the brain with the anatomical structures that constitutes the primary visual pathway, which can potential targets for the implantation of a visual prosthesis, in descending order from the eye to the primary visual cortex. Adapted from Mirochnik and Pezaris⁶. **(b)** Anatomy of the eye. The light rays enter the eye through the cornea, traverse the anterior chamber, the lens, the vitreous, to finally reach the retina, where they are absorbed and transformed into a neural signal. Adapted from Goetz and Palanker, 2016⁷. **(c)** Retinal organization and the main cell types present, with the three nuclear layers; the outer nuclear layer (ONL), the inner nuclear layer (INL), and the ganglion cell layer (GCL), and the two plexiform layers; the outer plexiform layer (OPL) and the inner plexiform layer (IPL). Light is transformed into a neural signal by the cones and the rods, which is relayed through the bipolar cells to the RGCs that send it to the brain for further processing. From Euler et al., 2014⁸.

1.1.2 The retina

1.1.2.1 Organization of the retina

As first uncovered by Ramon y Cajal more than a century ago, the retina can be divided into three principal layers containing neuron somas, namely the outer and inner nuclear layers (ONL and INL) and the ganglion cell layer (GCL). They are each separated by the two plexiform layers, the outer and inner plexiform layers (OPL and IPL) composed of the axons and dendrites of the neurons found in the nuclear layers (Figure 1-1c)⁹.

The most outer layer of the retina, the ONL, contains the photoreceptors, the cells responsible for the crucial task of converting the incoming photons into a neural signal. In humans, there are two different types of photoreceptors in the retina, the rods and the cones. These neurons have similar architectures; they can be divided into two segments, the outer and inner segments. The outer segment contains the membrane discs where the conversion of light to neural signal occurs, a process called phototransduction detailed in section 1.1.2.2. The first portion of the inner segment contains the standard cellular organelles, such as the mitochondria and the ribosomes, and the second portion the nucleus. The last part of the photoreceptor is the synaptic terminal which connects it to other neurons in the retina (Figure 1-2a)¹⁰. Rods allow us to see in dim light (scotopic condition) and saturate in bright light, while cones are sensitive to bright light (photopic condition) and allow us to perceive colors and finer details¹¹. Cones are principally found in the macula, an area of approximately 5 mm in diameter in the center of the retina. They reach a peak density of 168,000 cones /

mm² in its center, an approximately 1.5 mm in diameter elliptic area called the fovea, which forms a small depression in the retina as all the other layers of the retina are pushed aside to allow better light penetration, and is responsible for our sharp central vision. Their density then drops in an exponential manner when moving away from it^{12,13}. On the other hand, rods are absent of the fovea, and are the most abundant in its close periphery, attaining a peak density along an elliptic ring at approximately 10 degrees of eccentricity, after which their density gradually declines when moving toward the periphery of the retina¹⁴ (Figure 1-2b).

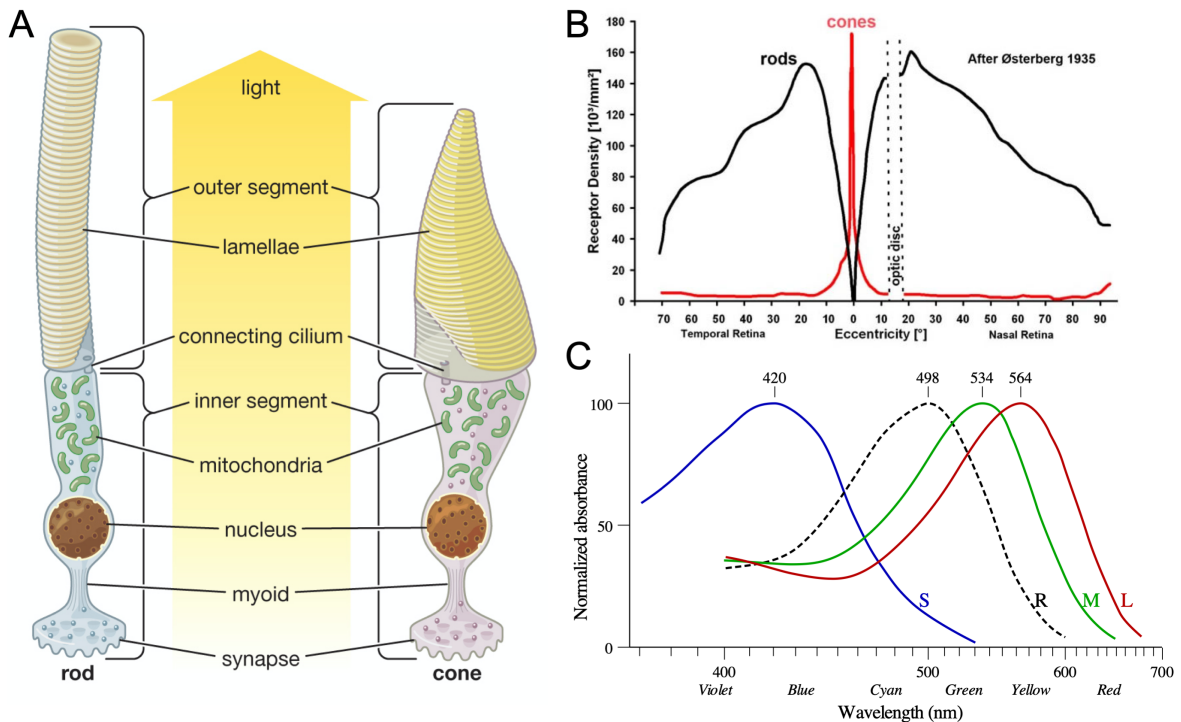


Figure 1-2 | Photoreceptors anatomy and distribution. (a) Rod and cone anatomy. In the dark, rods and cones are in an active state. The phototransduction is initiated in the membrane of their disc in their outer segment by the absorption of a photon by the 11-cis retinal molecule to consequently undergo a conformational change. This initiates a cascade of biochemical reactions that ultimately leads to hyperpolarization of the photoreceptors, which leads them to decrease their continuous release of glutamate. In the inner segment is found the standard organelles forming the inner cell machinery, and its lower portion the cell nucleus. They have a very short axon or myoid followed by a synaptic terminal that connects them to downstream neurons in the inner retina circuitry. Rods are maximally active in dim light conditions, while cones take over in bright light conditions. From Encyclopædia Britannica¹⁰. **(b)** Rods and cones density as a function of the eccentricity. The highest cone density is found in the center of the fovea and decreases steeply with eccentricity. Rods are absent from the retina and reach their highest density at approximately 10 degrees of eccentricity. The central retina is cone-dominated, while the periphery is rod-dominated. From Webvision: The Organization of the Retina and Visual System¹⁵ (originally from Østerberg, 1935¹⁶). **(c)** Cones and Rods absorbance as a function of the wavelength, with the peak absorbance of the three types of cones in the retina and the rods. Humans have three types of cones, the S-, M-, and L- and cones, each tuned for a specific wavelength of 420, 434, 564 nm. It's their combined activity that allows us to distinguish colors. Adapted from Bowmaker and Dartnall 1979¹⁷.

A single type of rods and three different types of cones are found in the human retina. These three types of cones are the S-, M-, and L-cones, referring to the width of the wavelengths to which they are the most sensitive (S, M, and L standing here for short, middle, and long wavelengths). They are also called the blue, green, and red cones, here referring to the color corresponding to the wavelength to which they are the most sensitive. They respectively have a peak absorbance of light with a 420, 533, and 564 nm wavelength¹⁸(Figure 1-2c). S-cones are the less frequent of the retina, representing only 10% of the total number of cones, and are absent from the fovea^{19,20}. Of the remaining cones, approximately 2/3rd are L cones, and 1/3rd are M cones^{21,22}.

In the next retinal layer, the IPL, are found three types of interneurons, the bipolar, amacrine, and horizontal cells (Figure 1-1c). The bipolar cells relay the visual signal they receive from the photoreceptors in the OPL to the retinal ganglion cells (RGCs) in the IPL^{23,24}. Bipolar cells receive input exclusively from cones or rods but never from both. There are at least 13 distinct types of bipolar cells in the human retina, with only one receiving its input from rods and the rest from cones^{25,26}.

Horizontal cells are interneurons connecting photoreceptors with one another in the OPL and are involved in lateral inhibition, which accentuates spatial differences in the photoreceptors' degree of activation. They contribute to the creation of center-surround receptive fields (RFs) in the bipolar cells^{27,28,29}.

Lastly, the retina contains over 30 different types of amacrine cells, which play a role in the integration and modulation of the visual signal^{30,31}. They form their synapse in the IPL and receive their input from bipolar cells and other amacrine cells, which they subsequently transmit to bipolar cells, other amacrine cells, or the RGCs²⁴.

In the last nuclear layer, the GCL, are found the RGCs, which are the first neurons of the retina to produce action potentials (all-or-nothing response) instead of graded potentials (Figure 1-1c). They receive their input from bipolar and amacrine cells and transmit it down to the brain through the optic nerve formed by their axons. There are only about 1.2 million axons in the optic nerve, compared to a total of approximately 130 million photoreceptors in the retina³². Due to this anatomical bottleneck of information, the retina's output must be drastically condensed while conserving the maximum information possible. There are more than 20 different ganglion cell types found in the retina to achieve this complex task, akin to an elaborate video compression algorithm²⁶. The majority of them are specialized in extracting and encoding specific aspects of the visual scene, such as amongst others the spatial or temporal frequencies (Figure 1-3b and c), the sign of the contrast, or the color, resulting in at least a dozen parallel pathways transmitted to the brain for additional processing³³.

Out of all these different types of RGC, three well-characterized populations of RGC make up approximately 90% of all the total number of RGCs of the retina (Figure 1-3a)^{20,34}: the midget, parasol, and bistratified ganglion cells. They have complementary roles in vision and are the origin of three anatomically well separated parallel pathways projecting to the two lateral geniculate nuclei (LGNs), respectively called the parvo-, magno-, and koniocellular pathways. The midget ganglion cells are the most abundant of the three, representing approximately 70% of the cells projecting to the LGNs³⁴. They have a slow axonal conductivity and typically have small RFs³⁵⁻³⁸. They are sensitive only to relatively large luminance contrasts and can detect high spatial contrast frequencies, but only low temporal ones (Figure 1-3b and c). Midget ganglion cells are involved in color vision, as they distinguish red and green color, and in fine details and depth perception^{30,39-41}.

The second most abundant RGCs are the parasol ganglion cells, which represent approximately 10% of the cells that project to the LGNs³⁴. They have a fast axonal conductivity and typically have larger RFs³⁵⁻³⁸. They are sensitive to low luminance contrast and can detect high temporal contrast frequencies, but only low spatial ones (Figure 1-3b and c). Parasol ganglion cells do not contribute to color perception but instead are involved in motion perception^{30,39-41}.

The third important pathway is the koniocellular pathways, which originates at least in part from the bistratified ganglion cells. They represent about 8% of the cells that project to the LGNs³⁴, and receive their input from S-cones and therefore are involved in our perception of the blue color²⁰.

The RFs (the area of the retina where a change in luminosity will result in a change of the cell's activity) of all these different RGCs are each arranged in mosaic tilings covering the entire surface of the retina, which ensures that any point of the retina is linked to each of these parallel pathways⁴². The RFs of the RGCs are the most compact in the fovea (the midget ganglion cells actually receive their input from a single bipolar cell), and broaden with increased eccentricity^{43,38,44}.

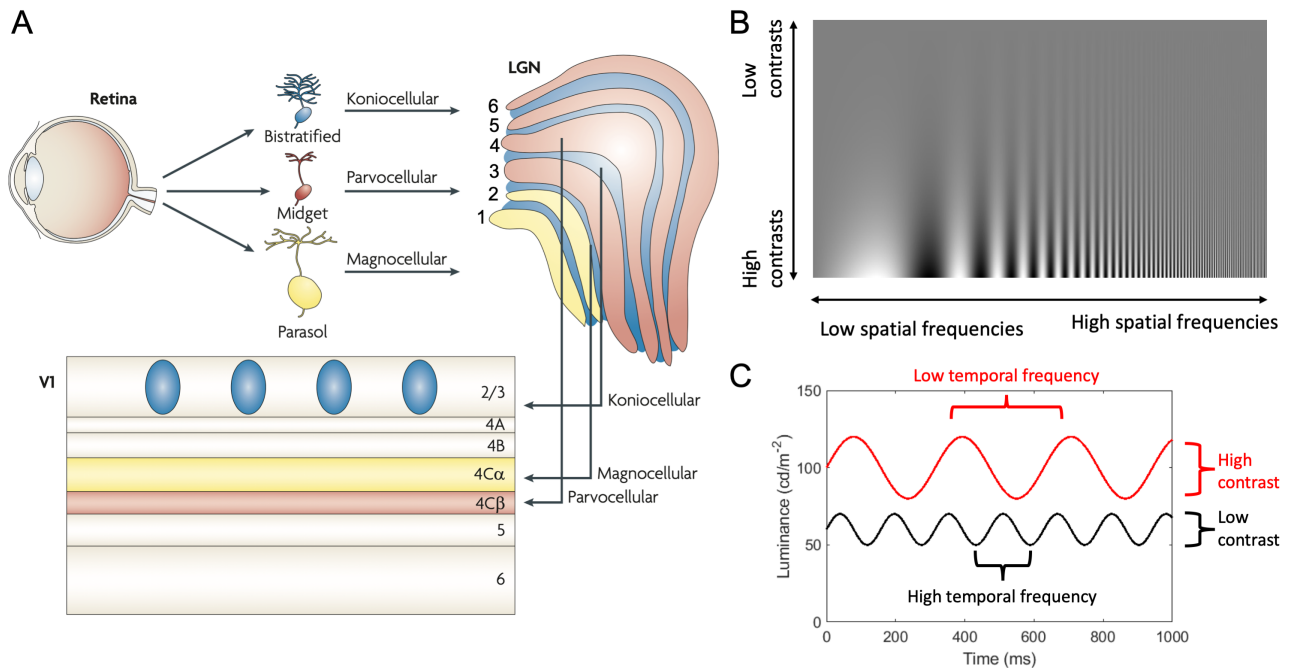


Figure 1-3 | The three main parallel pathways. (a) The three main RGC cell types, the midget, parasol, and bistratified ganglion cells, and the anatomical segregation of their respective associated pathways, the parvo-, magno-, and koniocellular pathways in the two structures containing cell bodies along the visual path, the LGN, and V1. The midget ganglion cells are the smallest of the three and have the narrowest RFs. They are part of the parvocellular pathway that projects to the four top layers of the LGN. Layers 4 and 6 of the LGN receive their inputs from the contralateral eye, while layers 3 and 5 receive their inputs from the ipsilateral one. The relay neurons the midget ganglion cells connect to in the LGN project to the layer 4C β of V1. The parasol ganglion cells are the largest of the three and have the broadest RFs. They are part of the magnocellular pathway that projects to the two deepest layers of the LGN. Layer 1 of the LGN receives its input from the contralateral eye, while layer 2 receives its input from the ipsilateral one. The relay neurons the parasol ganglion cells connect to in the LGN project to the layer 4C α of V1. The bistratified ganglion cells project to LGN neurons found in between the six layers, which themselves project to cytochrome oxidase blobs in layers 2 and 3 of V1. Adapted from Nassi and Callaway, 2019⁴⁵. **(b)** Contrast and spatial frequency. Here is plotted a Campbell-Robson contrast sensitivity chart. A high contrast represents a large change in luminance (bottom of the plot), and a low contrast a small one (top of the plot). A low spatial frequency corresponds to relatively far apart dots, or presently a luminance sine wave with a large period (left of the plot), while a high spatial frequency inversely corresponds to close dots, or presently a luminance sine wave with a short period (right of the plot). Interestingly the contrast sensitivity of the human eye is not constant. Instead, it is dependent on the spatial frequency and forms an inverted U-shape that reaches its maximum for intermediate spatial frequencies. From Larabi et al., 2009⁴⁶. **(c)** Contrast and temporal frequency. Temporal frequency corresponds to the speed of flickering of a light dot, for instance, or as illustrated to how fast the luminance sine waves oscillate. Midget cells are sensitive to high spatial frequencies but low temporal ones, while parasol cells are sensitive to high temporal frequencies but low spatial ones.

On top of the GCL is found the retinal nerve fiber layer (RNFL), the last layer of the retina. It is formed of the unmyelinated axons of the RGCs that coalesce to the optic disc, where they make a 90 degrees bifurcation to form the bundle of axons that is the optic nerve.

1.1.2.2 Phototransduction and center-surround receptive fields

In the dark, photoreceptors are in a constant active state: they are depolarized and continuously release the neurotransmitter glutamate⁴⁷. The process of phototransduction is initiated by the absorption of

a photon by the chromophore retinal, a molecule found inside the transmembrane protein opsin embedded in the membrane of the disks found in the outer segment of the photoreceptors. This causes the 11-cis retinal molecule to undergo a conformation change to its all-trans form, triggering a signal transduction cascade that ends with the closing of the GMP-gated cation channels of the photoreceptors. This results in the hyperpolarization of the photoreceptor, which ultimately leads to a decrease in the release of glutamate^{48–51}. Photoreceptors are non-spiking neurons; the more intense their illumination, the lower the quantity of glutamate they release⁵².

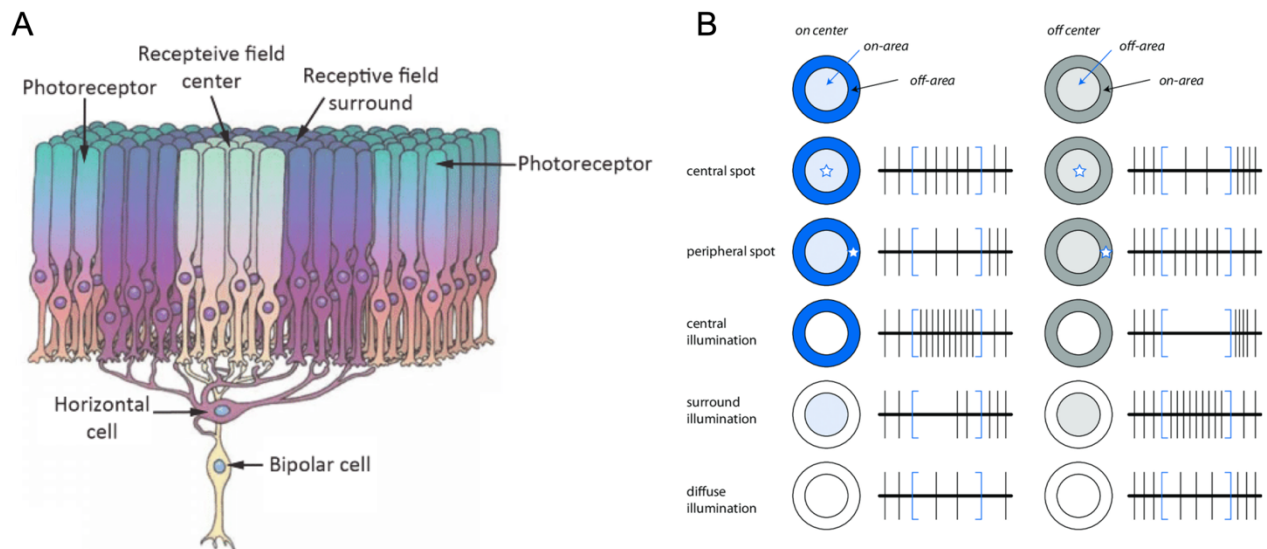


Figure 1-4 | Receptive fields overview. (a) Anatomy of the RF of a bipolar cell. The axons of the photoreceptors in the center of the RF are in direct contact with the dendritic tree of the bipolar cells. The photoreceptors in the surround of the RF are only in indirect contact with the dendritic tree of the bipolar cell through the intermediate of the horizontal cell. From Eye Pathology: An Atlas and Text⁵³. (b) ON- and OFF-center RGC change in spiking-rate following a transient change in the illumination of its RF. Blue and gray correspond to the whole surface of RF's surround kept in the dark, light blue and light gray correspond to the whole surface of an RF's center kept in the dark, white corresponds to the illumination of the whole RF's surround or center, the tiny white star corresponds to a spot of light illuminating only a fraction of the total surface of an RF's surround or center. From Zurak 2018⁵⁴.

Bipolar cells are the earliest cells in the visual pathway to have an RF, which is the approximately circular area of photoreceptors that influences the bipolar cells' responses^{55,56}. A bipolar cell is only directly connected to the photoreceptors in the center of its RF. The photoreceptors in the surround of its RF can also influence the bipolar cell's response, but only indirectly through the intermediate of the horizontal cells connecting them and the photoreceptors in the center of its RF. Horizontal cells deliver negative feedback to the photoreceptors in the center of the RF. In the dark, the horizontal cells are depolarized by the glutamate released on their dendritic tree by the photoreceptors of the surround of the RF. This leads them to also release glutamate, which causes the hyperpolarization of the photoreceptors in the center of the RF that receive their output. When illuminated, the horizontal cells hyperpolarize since they receive less glutamate and stop releasing glutamate, which leads to the depolarization of the photoreceptors in the center of the RF that receive their output^{57–61}. Due to the involvement of the horizontal cells, illuminating photoreceptors in the surround of its RF has the opposite effect on a bipolar cell than illuminating the ones in the center of its RF; this is called a center-surround organization (Figure 1-4a)⁶². Depending on the types of glutamate receptors they have, bipolar cells can exhibit two types of reaction when they receive glutamate: the OFF-center bipolar cells have ionotropic glutamate receptors, which make them depolarize when they receive glutamate effectively mirroring the behavior of the photoreceptor in its RF's center^{63,64}. They are therefore maximally active

when the center of their RF is in the dark while the surround of their RF is illuminated. The ON-center bipolar cells exhibit the exact opposite behavior; they have metabotropic glutamate receptors, which make them hyperpolarize when they receive glutamate, effectively changing the sign of the activation of the photoreceptors in its RF's center^{65,66}. Thus, they are the most activated when the center of their RF is illuminated while the surround of their RF is in the dark (Figure 1-4b).

When bipolar cells are activated, they also release glutamate. As all the RGCs possess only ionotropic receptors, they replicate the activation of the bipolar cells they are connected to; therefore, an RGC connected to OFF-center bipolar cells is itself OFF-center, while a RGC connected to ON-center bipolar cells is itself ON-center⁶⁷.

1.1.3 The optic nerve, the optic chiasma, and optic tract

The optic nerve is a 35 to 55 mm cylindrical structure made of the axons of the RGCs^{68,69}. Unlike what its name suggests, it is technically part of the central nervous system (CNS) and not from the peripheral nervous system (PNS). As part of the CNS, it is surrounded by the three meningeal layers, the dura, the arachnoid, and the pia mater (Figure 1-5a)^{70,71}. Additionally, it is the oligodendrocytes instead of the Schwann cells that are responsible for the myelination of its axons; they wrap around the axons forming concentric myelin sheets, which electrically insulates the axons. Thanks to myelination, myelinated axons have a conduction velocity of approximately an order of magnitude larger than their unmyelinated counterparts^{72,73}. There are two other types of glial cells (non-neuronal cells) found in the optic nerve, the astrocytes and the microglial cells. Astrocytes play a supporting role in neural tissue as they provide stability to the RGCs axon. They also separate them from the connective tissues and blood vessels and contribute to their fasciculation^{68,74-76}. Microglial cells are quiescent in healthy tissues and become activated only in case of neuronal damage, where they play a role in the phagocytosis of apoptotic cells, cellular debris, or bacteria and viruses^{68,77-80}.

The optic nerve can be split into four main segments based on their anatomical locations (Figure 1-5b). The first segment of the optic nerve is the optic disc, which measures about 1 mm in length. It is located where the RGC axons exit the eyeball through a hole in the sclera, filled with a sieve-like structure called the lamina cribrosa made out of several layers of intermingled collagen fibers. In a healthy eye, the lamina cribrosa contains 550 to 650 openings of a diameter ranging from 10 to 100 μm ^{81,82}. This anatomical structure is thought to play a role in preserving the pressure difference between the interior and the exterior of the eyeball. When the pressure builds up in the eyeball, the lamina cribrosa is posteriorly displaced, which pinches its openings that damage the axons that traverse it in the process, making it one of the causes of the nerve damage that occurs in glaucoma^{83,84}. The other connective tissues found in the optic nerve form the extra-fascicular matrix, which separates the axonal fibers of the optic nerve in fascicles. The number of fascicles varies between 100 and 300 depending on the position along the length of the nerve (Figure 1-5e)⁸⁵.

The second segment of the optic nerve is the intraorbital segment, which is about 25 mm in length. The optic nerve fibers become myelinated once they exit the eyeball, making this region double in diameter from 1.5 to 3 mm. The central retinal artery and the central retinal vein, which provide the blood supply to all layers of the retina beside the photoreceptor layer, enter the optic nerve at about 10 mm from the eyeball. The optic nerve then enters the skull through the optic canal, forming the intracanalicular segment, which length varies between 4 to 10 mm. The last segment is the intracranial segment that represents the final 10 mm of the nerve^{68,69}.

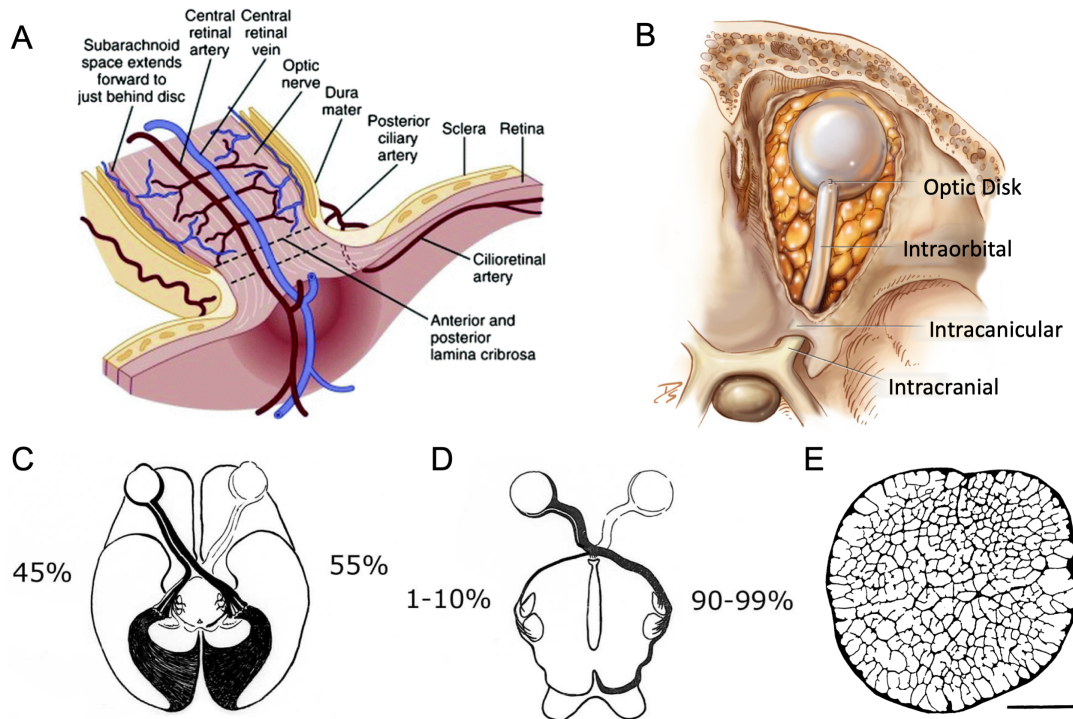


Figure 1-5 | Anatomy of the optic nerve. (a) Optic head anatomy. The axons of the retina's RGCs converge to the optic nerve head, where they take a sharp turn and exit the eyeball through an opening in the sclera, filled by a sieve-like connecting tissue called the lamina cribrosa. The central retinal artery and veins that supply blood to the inner retina enter the eyeball through the optic nerve center. The optic nerve is surrounded by the three meningeal layers present in the CNS, the dura mater, the cerebrospinal fluid, and the pia mater. From *Abnormalities of the optic nerve and retina*⁸⁶. (b) The optic nerve's four different anatomical segments: the optic disk, the intraorbital, the intracranial, and the intracranial segments are respectively approximately 1, 25, 7, and 10 mm long. Adapted from *Atlas of Endoscopic Sinus and Skull Base Surgery*, 2nd edition, 2019⁸⁷. (c and d) Percentage of optic nerve fibers decussation at the optic chiasma for primates and rodents. In primates, which have a very large binocular visual field, approximately half of the optic nerve fibers decussate at the chiasm. In rodents and other vertebrate species with lateral eyes, it is most of the fibers that decussate. From *Webvision*¹⁵ (e) Fascicular organization of the optic nerve in the intraorbital segment. The number of fascicles varies between 100 and 300 depending on the position along the optic nerve. The scale bar is 1 mm. From *Jeffery et al.*, 1995⁸⁵.

At the end of the intracranial segment, the optic nerves of both eyes meet at the optic chiasm. A fraction of the optic nerve fibers originating from the nasal side of the retina decussates (cross the midline toward the contralateral side of the brain), while the remaining ones originating from the temporal side continue toward the ipsilateral side of the brain. The fibers of each eye that did not cross the chiasma combine with the fibers of the opposite eye that crossed the chiasma to form the optic tracts which are the post-chiasmatic extensions of the optic nerves that further project to the brain. Depending on the species, a different fraction of the optic nerve fibers will decussate. In humans and in other vertebrate species with a large overlap between the visual field of each eye, there is an approximately evenly split with 55% crossed and 45% uncrossed fibers (Figure 1-5c)^{88,89}. On the other hand, the majority of fibers decussate (between 90% and 99% crossed fibers in the case of rodents) in vertebrate species with lateral eyes and with little overlap between the visual field of each eye, such as rodents or rabbits (the animal model we use) (Figure 1-5d). Some conditions, such as albinism, result in anomalies in the visual system; indeed, albino patients have a misrouting of the uncrossed fibers, with a ratio of crossed and uncrossed fibers of 80% to 20%, which leads to an absence of normal binocular vision in the affected individual⁹⁰⁻⁹³. This decrease in the number of uncrossed fibers in albino individuals has been reported in several other mammalian species⁹⁴⁻⁹⁶.

In primates, due to the presence of the fovea, the organization of the axonal fibers at the level of the optic disc does not match the retinal organization of the RGCs somas they originate from. The axonal fibers originating from the macula known to form the papillomacular bundle enter the optic nerve through its most

temporal side. No axonal fibers pass on top of the fovea and go around it instead to permit a maximal visual acuity in the fovea. Therefore, the superior and inferior arcuate bundles formed by the axons of the RGCs located further temporally than the fovea circumvent it and the papillomacular to enter the optic nerve from above and below the macular axonal fibers. The axons originating from the superior and inferior temporal retinal quadrants respectively enter the optic nerve through its upper and lower side. Finally, the axonal fibers originating from the nasal retinal quadrants enter the optic nerve through its most nasal side (Figure 1-6a). The axonal fibers gradually reorganize along the optic nerve, and by the time both optic nerves merge at the chiasma, the fibers originating from the macula will have shifted to a central position in the optic nerve. At this level, the axonal fibers found in the four quadrants of the optic nerve originate from the respectively corresponding quadrants of the retina⁹⁷⁻¹⁰⁰. This correspondence between the mapping of a portion of the visual system and the mapping of the retina is a property called retinotopy, and the optic nerve in the prechiasmatic area is the earliest portion of the visual path to exhibit this property. Since RGCs have much more compact RFs in the macular area than in the periphery, the representation of the macular area is greatly magnified compared to the periphery in the optic nerve, with 90% of the total number of axonal fibers that constitute the optic nerve originating from the macular area⁶⁹.

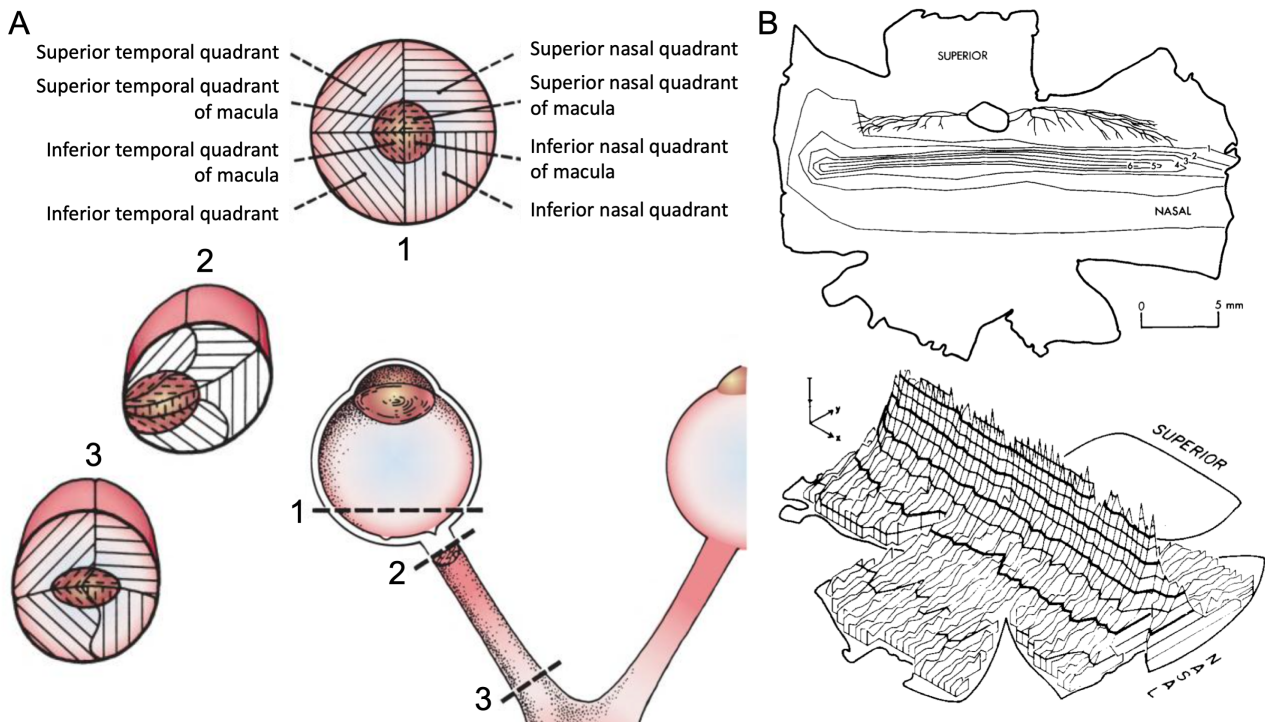


Figure 1-6 | Optic nerve inner fibers organization. (a) Location of the four quadrants of the retina inside the optic nerve in the optic disc and the pre-chiasmatic area. Due to the temporal location of the macular area relative to the optic disc, it enters temporally in the optic nerve and gradually shifts toward a central position by the time the optic nerve reaches the chiasma. From DeJong's *the Neurologic Examination*¹⁰¹. **(b)** The rabbit's visual streak. Like several vertebrate species with very lateral eyes, the rabbit has a visual streak instead of a fovea. It consists of a narrow band with a very high density of RGCs located below the optic disc and taking up almost the whole width of the retina. The top and bottom are a 2D and a 3D view of the iso-contour lines, where the number indicates the number of thousand RGC per mm². From Hughes, 1971¹⁰² and Oyster et al., 1981¹⁰³.

The interior organization of the optic nerve of rodents and rabbits is not well studied, probably due to a lack of incentives, and knowledge about them is very sparse. In the rabbit, Lashley says: "Brouwer reported that in the rabbit the exact topographical distribution of the elements of the retina is not preserved by the fibers in the optic nerve but that there is a tendency for the fibers from the four quadrants of the retina to be grouped in corresponding quadrants of the nerve. He does not state whether this is true throughout the

length of the nerve.”(from Lashley 1930¹⁰⁴ about Brouwer 1923¹⁰⁵), suggesting that some sort of crude retinotopic organization might be present in the rabbit’s optic nerve. Concerning the rat, he goes on to say: “In the rat the optic nerve is 7 to 8 mm in length. For a short distance back of the bulb the fibers tend to be grouped in a sector of the nerve corresponding to the sector of the retina which has been injured. Within less than 1 mm. they are scattered throughout the entire nerve although for a short distance they remain somewhat more concentrated in the quadrant of the nerve corresponding to the locus of the retinal injury. As the nerve approaches the chiasma the distribution of the granules becomes still more irregular and from the limited material at hand I have not been able to determine any consistency of arrangement near the chiasma.”(from Lashley 1930¹⁰⁴), suggesting that a retinotopic organization is only present in the first portion of the nerve, but is lost at the chiasma. This appears to be more recently confirmed by Tsuruga and colleagues in the mouse, where the retinotopy is conserved for the first millimeter of the nerve but is lost by the third¹⁰⁶.

Regardless, one can assume a markedly different fibers organization in the optic disc of the rabbit compared to primates since they lack a fovea. Indeed, they instead have a visual streak, a narrow horizontal band with a very high density of RGCs located below the optic disc that spans most of the retina. The peak RGCs density is found in the middle of it and decreases steeply when vertically moving away from it (Figure 1-6b)¹⁰³.

Optic nerve axons are smaller than typical peripheral nerve axons, with an average diameter of 0.72 μm in humans, a dimension that appears conserved in rabbits and other mammalian species^{107–109}. In the retina, and therefore likely in the optic nerve as well, it appears that parasol RGCs have larger axonal diameters than midget ones, and both see their diameter increase with eccentricity¹¹⁰. More precisely, it has been reported that the retina’s axons are the smallest in the papillomacular bundle, then slightly larger in the upper and lower arcuate bundles, and reach their maximal diameter in the periphery¹¹¹.

1.1.4 The lateral geniculate nucleus and the optic radiations

The LGNs, a pair of small stratified anatomical structures, are part of the thalamus. They serve as relays for the visual signal between the retinas and both V1 hemispheres and receive the input of 90% of the RGCs of the retinas¹¹². Each LGN has six distinctive layers in primates. The two ventral ones are the magnocellular layers and receive their input from the parasol ganglion cells. The four dorsal layers are the parvocellular layers and receive their input from the midget ganglion. The neurons in the magnocellular layers have larger cell bodies than the ones in the parvocellular layers^{113–116}. In between the magnocellular and parvocellular layers are the koniocellular layers, which contain very small cells that form synapses with bistratified blue-sensitive ganglion cells (Figure 1-3a)¹¹⁷.

As mentioned earlier, the axons originating from both retinas arriving at the LGN form a synapse with neurons from the LGN, though the axons of each retina arrive in distinctly separated layers: the neurons found in layers 1, 4, and 6 form synapses with axons originating from the contralateral eye, while the neurons found in layers 2, 3, and 5 form synapses with axons originating from the ipsilateral eye¹¹⁸. Each layer of the LGN is organized in a retinotopic manner; neighboring neurons in the LGN correspond to neighboring region of the visual field (Figure 1-3a). Like in the optic nerve, the portion of the LGN that corresponds to the center of the visual field is also magnified¹¹⁹. Neurons in the LGN have a center-surround organization comparable to the one of the RGCs¹²⁰. The axons of the neurons that exit the LGN form the optic radiations, which project to the primary visual cortex.

1.1.5 The primary visual cortex

Each hemisphere of the primary visual cortex (V1), which is located occipitally in the skull, receive its input exclusively from the contralateral half of the visual field. V1 is the main area of the brain that integrates and processes the visual signal originating from the retina. Like the other cortical regions, it can be divided into six principal layers¹²¹. Most of the optic radiations project to layer 4, which can be separated into four sublayers: 4A, 4B, 4C α , and 4C β ^{122,123}. The axons of the magnocellular pathway arrive in sublayer 4C α , and the majority of axons of the parvocellular pathway arrive in sublayer 4C β (some arrive in sublayer 4a as well)^{123–125}. Finally, the axons of the koniocellular pathway project to aggregated patches of neurons called cytochrome oxidase blobs in layers 2 and 3 (Figure 1-3a)^{124,126,127}.

V1 is organized retinotopically with a magnified representation of the central visual field (Figure 1-7a)^{128,129}. The magnification factor (M), defined as “the diameter in the primary visual cortex onto which 1 deg of the visual field project.” by Daniel and Whitteridge, is the largest in the center of the V1 representation of the fovea and gradually decreases with eccentricity¹³⁰. The inverse of M was shown to increase approximately linearly with eccentricity¹³¹.

The neurons found in the sublayer 4C share their center-surround organization of their RFs with the LGN neurons from which they receive their input^{122,132,133}. However, the RFs found in the other layers have different and more elaborate organizations; neurons named simple cells have RFs that can be separated in different elongated antagonistic ON and OFF regions, which make them selectively tuned to a specific spatial frequency and stimulus orientation. The second type of neurons named complex cells exhibit a similar spatial frequency and orientation selectivity, but their RFs do not have distinct on and off regions, and they can consequently be activated by a darker or lighter bar presented anywhere on their RFs^{134,135}.

An important characteristic of the neurons in the cortex is their columnar organization, first discovered in the somatosensory cortex, which refers to the property of a cortical column (a group of neurons vertically aligned through the layers of the cortex, approximately perpendicular to the cortical layers) to share some distinct functional features¹³⁶. Two columnar organizations found in the primary visual cortex are the orientation and ocular dominance columnar organizations. Orientation columns contain neurons that respond preferentially to bar stimuli with a certain orientation; their spiking frequency augments when the orientation of the bar is gradually rotated. Ocular dominance columns contain neurons that respond preferentially when one of the two eyes are stimulated (Figure 1-7b and c)^{135,137–139}. These two types of columns are not organized randomly over the surface of V1, the orientation columns form pinwheel-like patterns, where the preferred orientation gradually shifts around the pinwheel center, and the ocular dominance columns are arranged in an intermingling stripes-like pattern^{139–141}(Figure 1-7d and e).

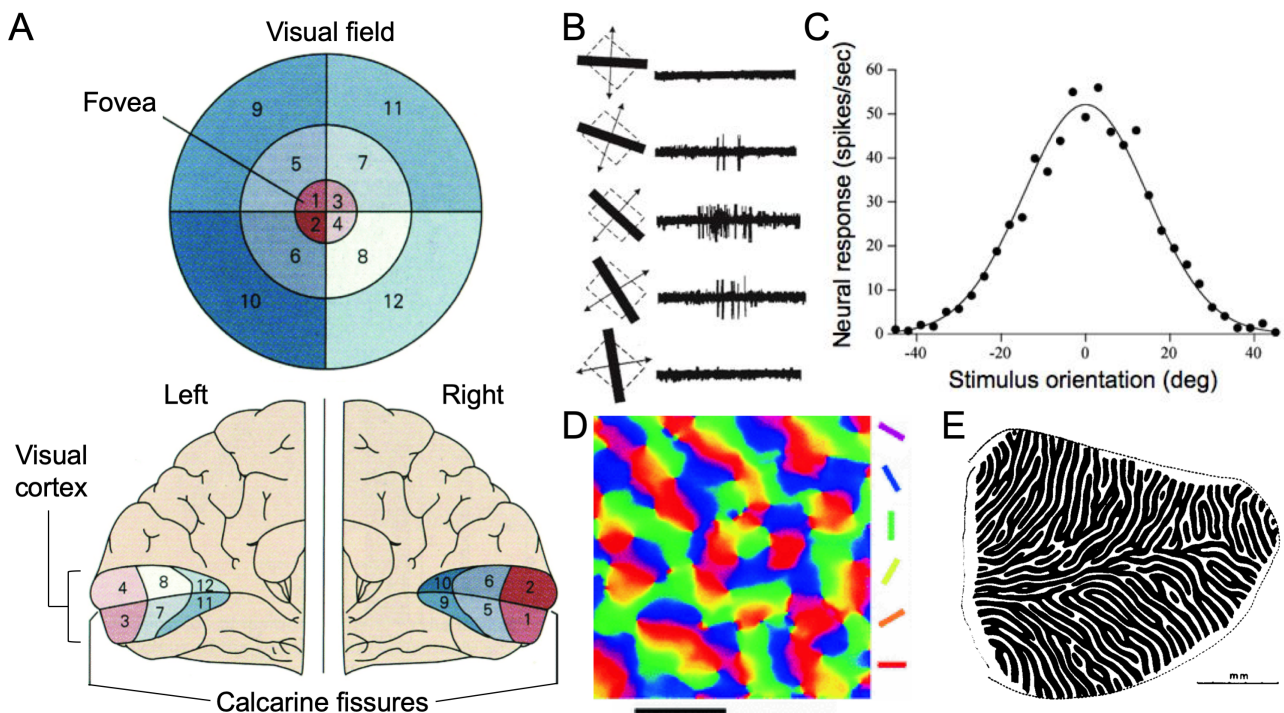


Figure 1-7 | Overview of the primary visual cortex organization. (a) Primary visual cortex retinotopy and magnification of the central visual field. The representation of the macular area in V1 is greatly magnified compared to its actual retinal surface. Shown here is the relative size of the portions of the visual field (top), which representations are the same surface in V1 (bottom). Each V1 hemisphere receives input exclusively from the contralateral half of the visual field. Adapted from Paulun et al., 2018¹⁴². (b and c) The response of a complex cell of the monkey striate cortex to the presentation of a moving bar in its RF at different orientations and the associated tuning curve with the spiking rate as a function of the bar orientation. Adapted from Hebel and Wiesel, 1968¹³⁷ (d) Orientation preference map in monkey striated cortex. The scale bar 1 mm. Adapted from Sadeh and Rotter, 2013¹⁴³ (originally from Blasdel and Salama, 1986¹⁴⁴). (e) Ocular dominance map in V1 of the monkey. Black regions receive input from one eye and white regions from the other eye. The scale bar 5 mm. Adapted from Oster and Bressloff, 2006¹⁴⁵ (Originally from Hubel and Wiesel, 1977¹⁴⁶).

1.2 Blindness and retinal dystrophies

1.2.1 Blindness

The standard visual acuity of a healthy person is defined as the ability to correctly identify written letters on line 20/20 of a Snellen chart. This is equivalent to being able to perceive two points 1 minute of arc ($1/60^{\text{th}}$ of a degree) apart as separated (Figure 1-8a). Visual acuity is measured as a ratio compared to standard acuity, so a 20/200 visual acuity means that the smallest object you can distinguish at 20 feet away would still be barely distinguishable at 200 feet for a person with a healthy visual acuity. Vision acuity is related to the cone density, and therefore is not homogenous over our whole visual field; our maximal visual acuity is present in the center of the fovea and drops rapidly with increased eccentricity (Figure 1-8b)^{1,2}. The commonly understood definition of blindness, the total loss of light sensitivity, is intuitive, but it may be over-restrictive as very few conditions actually result in a total absence of light perception. For the purpose of this thesis, the legal definition of blindness, which consists of either a visual acuity lower than 20/200 or 20/400 depending on the country or a visual field smaller than 20° on the better eye, is more appropriate and is the one that will be used^{147–150}.

On rare occasions, blindness can be congenital, but more often than not, it is a condition that is acquired during one's lifetime, following injuries, or due to a retinal degenerative disease. Blindness, especially when

acquired at a late stage in life, has a dramatic effect on the quality of life of the patient suffering from this condition. Indeed, it makes maintaining professional activities close to impossible, effectuating daily routine tasks very difficult, and overall results in an important loss of independence. Blindness may also be an added financial burden for the person affected and their family and can often have a negative impact on their mental health, potentially leading to anxiety and depression^{151–153}. Worldwide, the two leading causes of blindness are cataract, and uncorrected refractive errors, followed by glaucoma and age-related macular degeneration (AMD), which respectively account for approximately 35%, 20%, 10%, and 9% of the cases of blindness worldwide^{154,155}. With more than 45 million blind people worldwide, a number that is estimated to more than double by 2050, blindness represents a major health issue for our society^{154,156}.

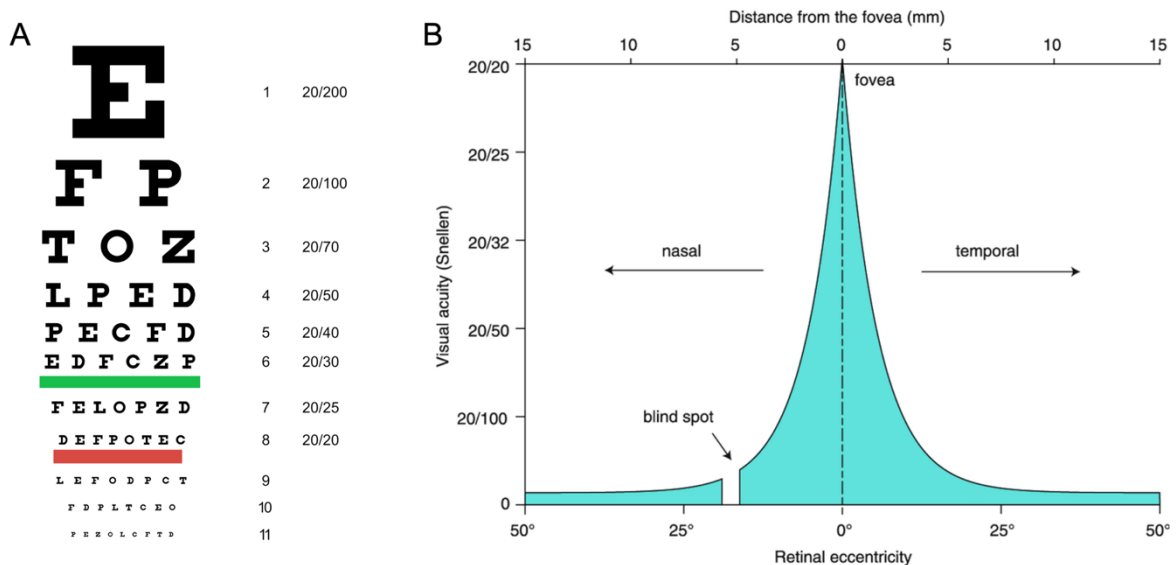


Figure 1-8 | Visual acuity definition. (a) Typical Snellen chart, with the different sized letter and their corresponding visual acuity. The visual acuity of someone is determined by the last line someone can read correctly on a Snellen chart. (b) Acuity as a function of eccentricity. The maximal visual acuity is found in the fovea and decreases steeply with increased eccentricity. From Lambertus and al., 2017¹⁵⁷.

1.2.2 Age-related macular degeneration and retinitis pigmentosa

Not only is it the fourth cause of blindness worldwide, but AMD is also the leading cause of blindness in the Global North, and currently has no cure^{158,159}. This disease is late-onset, and its first clinical signs usually appear above the age of 55¹⁶⁰. The older the population, the higher the number of cases; early signs of potential AMD are present in 18% of people between 65 and 74 and in 30% of people above 74¹⁶¹. As its name suggests, the disease consists of a gradual degradation of the central visual field. The causes of AMD are not yet fully understood, but several genetic predispositions and aggravating environmental risk factors, such as smoking, hypertension, or high cholesterol, have also been identified^{162–168}.

This disease has two forms, the “dry” and the “wet” one. The dry form progresses to the wet form in 10 to 15% of the cases¹⁶⁰. The dry form of the disease is characterized by the accumulation of cellular debris between the retina and the choroid, called drusen (visible yellowish spots on an eye fundus). They originate from the inflammation and cellular death of the RPE in the macular area, which obstructs the diffusion of nutrients from the choroidal vessels to the photoreceptor layer (Figure 1-9d and g). The wet form is characterized by abnormal choroidal neovascularization that leads to fluid leakage in the extracellular space between the neural retina and the RPE. Both forms result in photoreceptors’ death, though it occurs at an accelerated rate in

the wet form, which ultimately leads to the loss of central vision (Figure 1-9e and h). Typically, 3 to 10 degrees of the central visual field is totally lost, but this surface can increase with the progression of the disease, though some peripheral degree vision remains preserved in most cases (Figure 1-9a and b)^{7,169–171}. In severe cases of AMD, the visual acuity of the patient can reach low levels from 20/100 up to 20/800¹⁷².

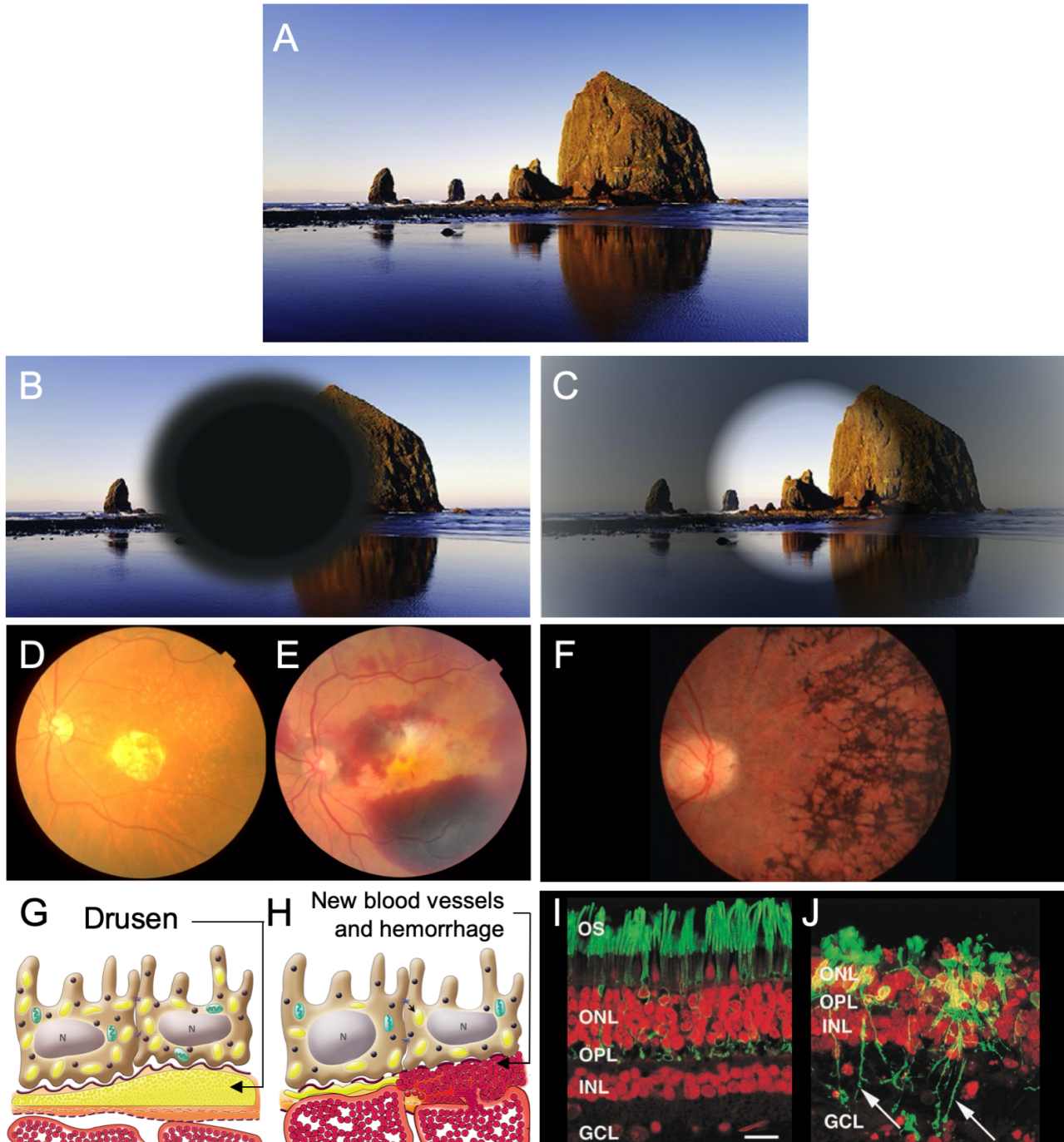


Figure 1-9 | Age-related macular degeneration and retinitis pigmentosa. Normal vision (a) and simulated AMD (b) and RP vision (c), showing the loss of the central visual field and the tunnel vision characteristic of the two diseases. Adapted from Yue et al., 2016¹⁷³. (d and e) Fundus image of a retina with the dry and wet forms of AMD displaying visible drusen in the macular area of the first panel and abnormal neo-vasculature in the second. Adapted from Parvini et al., 2014¹⁷⁴. (f) Fundus image of a retina with RP displaying the typical presence of dark pigments. Adapted from *Maladies de la rétine, Encyclopédie de la vue*¹⁷⁵. (g and h) Schematic side view of the choroid and the RPE with the characteristic apparition of drusen and abnormal neo-vasculature, respectively. Adapted from Parvini et al., 2014¹⁷⁴. (i and j) Immunolabeling of rod in (green) and other retinal cells (red) of a normal and a retinitis pigmentosa retina. The vast majority of the remaining rods have lost their outer segments. Arrows point at some abnormal rods neurites that have extended even further than the INL to terminate in the GCL. Fariss and Milam, 2000¹⁷⁶.

A second important type of chronic degenerative disease of the retina is retinitis pigmentosa (RP), which is an inherited retinal dystrophy affecting an estimate of 1 in 4000 people worldwide^{177,178}. It is a heterogeneous group of genetic disorders, with so far more than 60 identified genes involved in the different forms of the diseases^{179–181}. It can be inherited in a variety of ways, either in an autosomal dominant, recessive, or X-linked fashion, and the age of onset may vary from childhood to late stages of life^{178,180}. However, it manifests itself in the same manner, independently of its variant. The first noticeable sign of the disease is night blindness, as the early stage of the disease is characterized by progressive death of the rods starting from the mid-periphery and progressing toward the periphery. The second stage of the disease is characterized by a complete loss of peripheral vision, called tunnel-vision, where only 3 to 10 degrees of the central visual field are spared (Figure 1-9c, f, i, and j)¹⁵⁸. While most forms of the disease predominantly affect the rod, in the disease's most advanced stage, the cones degenerate as well, which can lead to a drastic visual acuity decline or even complete blindness^{177,182–184}.

In patients with AMD, the RGC layer remains mostly unaffected, with only about 7% of the RGC dying, and the number of cells found in the INL remained unchanged or can even increase¹⁸⁵. In RP, it appears that the integrity of the retina is more impaired, with 88% of the inner nuclear layer and 48% of the RGCs conserved in patients with moderate RP and with 78% of the inner nuclear layer and 30% of the RGCs conserved in patients with advanced RP^{186,187}. However, since both diseases currently have no cure, it still makes them attractive conditions to be addressed with a visual prosthesis, even though only a fraction of the RGCs are conserved in advanced stages of RP.

1.3 Visual Neuroprostheses

1.3.1 Definition and principle

As the name suggests, neuroprosthetic devices are prosthesis that interacts with the nervous system. Their goal is to restore a lost function caused by a missing or defective limb or organ/tissue. They can be divided into three categories, sensory, motor, and cognitive neuroprostheses, according to the type of function they aim to restore. They can also be broadly separated into categories according to the directionality of their interaction with the nervous system. Sensory neuroprostheses, which aim at restoring a lost sensory modality, mainly stimulate a remaining healthy portion of the nervous system to mimic a missing nervous input. On the other hand, motor neuroprostheses, which aim at restoring some lost motor function, mainly record and decode the activity of the remaining healthy portion of the nervous system in order to for instance to move an artificial limb. Though there also exist several applications involving both the decoding and encoding of neural signals.

In recent years, research groups have explored various novel neuromodulation approaches ranging from thermal¹⁸⁸, magnetic¹⁸⁹, or biochemical stimulation¹⁹⁰, but the unequivocally most commonly used approach has been electrical stimulation, perhaps unsurprisingly as neurons themselves naturally use electrical signals to communicate with one another. Indeed, most neurons do so by using axon potentials, which are fast transient membrane depolarizations that travel along the neuron's axon up to the axon's terminals, where the membrane depolarization results in the release of neurotransmitter that triggers the activation or the inhibition of the neurons they form a synapse with. The propagation of an action potential relies on the consecutive opening and closing of different voltage-gated ion channels, transmembrane proteins that allow the passage of specific ions through the axon's membrane, which opening and closing are triggered by a change

in the axon membrane potential (the difference between the intracellular and extracellular potential). More specifically, the propagation of an action potential is initiated when the negative resting transmembrane potential is raised above a certain threshold (Figure 1-10a)^{191–193}.

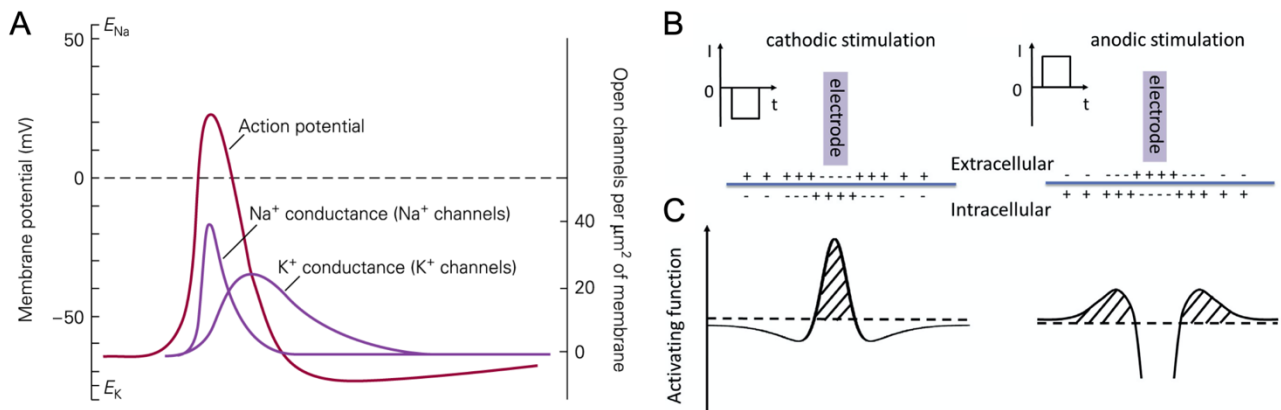


Figure 1-10 | Principle of electrical stimulation. (a) Detailed action potential cycle. When the neuron's resting membrane potential is brought from -70 mV to above the threshold potential of -55 mV, sodium channels open. This initiates an inflow of sodium ions in the neuron that further depolarizes the neuron's membrane. When the membrane potential becomes positive, the sodium channels inactivate, and the potassium channels open. This halts the inflow of sodium ions and initiates the outflow of potassium ions bringing the membrane potential back to its resting potential with a short hyperpolarization period. The action potential travels from the neuron soma down its axons to the synapse. The curve in dark red is the membrane potential, and the two purple curves are the conductance of the sodium and potassium channels as a function of time. From Principles of Neural Science, Fifth Edition¹⁹³. (b) Cathodic and anodic stimulation. The injection of a current pulse results in a redistribution in the charges in the extracellular medium. A cathodic pulse results in the decrease of the extracellular potential just below the electrode, which leads to the depolarization of the axon's membrane. An anodic pulse has the opposite effect; it increases the extracellular potential just below the electrode, which results in the hyperpolarization of the axon's membrane. From Yue et al., 2016¹⁷³. (c) Cathodic and anodic stimulation activation function along the axon's length. The dashed areas indicate the positive activation or depolarization region of the axon. From Yue et al., 2016¹⁷³.

The principle of electrical stimulation relies on the manipulation of the extracellular potential to artificially increase the membrane potentials of the target neuron in order to elicit the propagation of an action potential (in some cases indirectly through the graded depolarization of non-spiking neurons that form synapses with actual spiking neurons, such as in subretinal stimulation of the bipolar cells). Current pulses of both polarities can be used to depolarize the neuron membrane, though stimulation thresholds are lower for cathodic current pulses than for anodic ones (Figure 1-10b). Rattay developed the activation function, which shows that the depolarization of an axonal membrane is approximately proportional to the second spatial derivatives of the extracellular potential along the axon (Figure 1-10c). This explains why an anodic current pulse can also result in axonal depolarization but only at higher current amplitudes, since while an anodal pulse results in the hyperpolarization of the axon directly below a stimulating electrode, it is flanked by two lower magnitude depolarization areas. It also explains a phenomenon called a cathodic block, which occurs when an axon is too close to the stimulating electrode when receiving a cathodal pulse; in such condition, the cathodic pulse results in a large depolarization of the axonal membrane just below the stimulating electrode, but the elicited action potential cannot pass the two flanking hyperpolarization areas^{194–197}. Additionally, the presence of the squared axonal radius in the denominator in the first term of the activation function means that large-diameter axonal fibers are recruited at a lower current threshold than small-diameter ones. This can have some adverse effects, such as in functional electrical stimulation in motor prosthesis applications, as muscle fibers which are innervated by large-diameter axonal fibers are naturally recruited last to accomplish high-intensity contraction, and thus can lead to fast fatigue of the muscles¹⁹⁸.

The electrical stimulation principle can be applied to any part of the nervous system, and therefore have a very broad range of potential applications; there have been several studies investigating the electrical stimulation of the brain, the spinal cord, and the peripheral nervous system. The following section will focus on its use in the field of visual prostheses, which goal is to use electrical stimulation to activate remaining healthy portions of the visual system in blind patients to artificially restore their sense of sight. This is meant to be achieved by a device that can elicit the controlled and selective apparition of phosphenes, which are artificial visual percepts resembling bright light spots, arranged in an organized manner in order to reproduce an image in the visual field of a blind patient (Figure 1-11a). A visual prosthesis relies on the brain's plasticity to eventually make sense with prolonged training of what may initially appear as a hard-to-disentangle arrangement of phosphenes closely after the prosthesis implantation (Figure 1-11b).

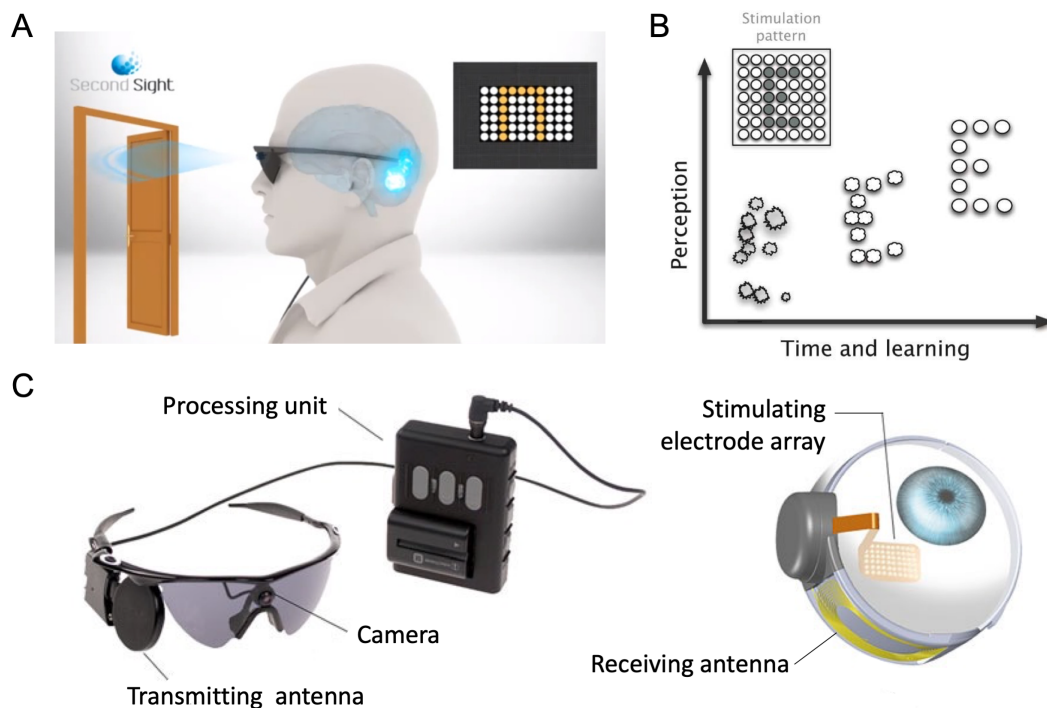


Figure 1-11 | Visual neuroprosthesis principle and main elements. (a) Principle of a visual neuroprosthesis. The principle of a visual neuroprosthesis consists of recording the visual scene with a camera, then converting the image in a combination of stimulating current pulses and finally stimulating a remaining healthy portion of the visual path to elicit the apparition of arranged phosphenes in the visual field of the patient, with the expectation they will interpret it as an image. From Second Sight¹⁹⁹. **(b)** Perception learning. A visual prosthesis relies on the patient's learning capacity and their ability to eventually make sense of what may initially appear as an uncoherent cloud of phosphenes. From Webvision¹⁵. **(c)** Example of the main components of a visual prosthetic system. All visual prosthetic systems (besides the latest photodiode retinal implants) are made out of a camera that captures the visual scene, a visual processing unit that transforms the camera input in a simplified and pixelized image and turns it into a series of corresponding current pulses, and a stimulator that the deliver the current pulses to the target neural tissue. Here is shown the example of the Argus II. From Dagnelie et al., 2017²⁰⁰.

A typical neuroprosthetic system consists first (in most cases) of a camera mounted on a pair of goggles to record the visual scene, a portable image processing unit to simplify and enhance the image, which may consist of processing steps such as edge detection, removal of low informative features, or contrast adjustment^{201,202}, before transforming it into the corresponding combination of electrical signals, and a stimulator to deliver a current pulse to the target anatomical structure (Figure 1-11c)²⁰⁰.

Since the experiments that lead to the first records of phosphene perception conducted about a century ago^{203,204}, scientists have attempted to use the retina, the optic nerve, the LGN, and the primary visual cortex as a potential target for phosphenes, with varying degrees of success (Figure 1-12).

The specific advantages and drawbacks of each approach will be detailed later, but a widely accepted principle is that stimulating the closest remaining portion of the visual path to the lesion / defective tissue causing blindness is advantageous since it minimizes the amount of natural processing of the visual signal the prosthetic device will have to reproduce. On the other hand, the further downstream the visual path the visual prosthesis is located, the larger number of diseases/conditions it can address.

1.3.2 Retinal implants

In recent years, retinal implants have become the most investigated approach for artificial vision due to the relative ease of their implantation and the diminished risks associated with it compared to other approaches, as well as the low level of processing of the visual signal they need to reproduce. Additionally, thanks to their pre-chiasmatic location on the visual path, approximately 3/4th of the visual field can be covered by the implantation of a single eye²⁰⁵.

Retinal implants can be separated into three categories according to the location of their implantation sites: epiretinal implants are positioned above the nerve fiber layer, with one of its faces in direct contact with the vitreous. Subretinal implants are placed in an incision between the RPE and what remains of the photoreceptor layer. Lastly, the suprachoroidal implants are placed in an incision between the choroid and the sclera, or in some cases directly on top of the sclera (Figure 1-12)³².

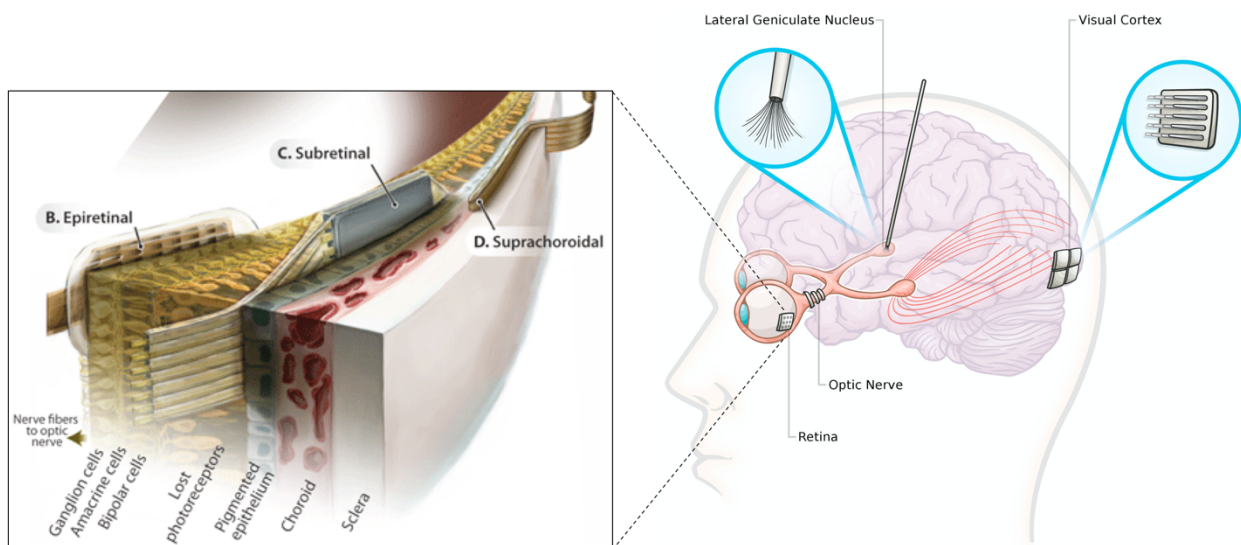


Figure 1-12 | Anatomical targets for visual prostheses along the visual path. At the level of the retina, there are three possible anatomical implantation locations: the suprachoroidal location, which is in a pocket in between the sclera and the choroid, the subretinal location, in a pocket between the degenerating photoreceptor layer and the RPE / instead of the photoreceptor layer, and the epiretinal location, which is on top of the RNFL layer. The subretinal one is the closest to the bipolar cells, the most upstream remaining cells of the visual path in conditions such as AMD or RP. The other investigated anatomical targets for a visual prosthesis are the optic nerve, the LGN, and V1. Adapted from Zrenner, 2013³² and Lewis et al., 2015²⁰⁶.

Thanks to their location, epiretinal implants are the ones requiring the less complex implantation procedure²⁰⁷. Furthermore, their direct contact with the relatively large volume of the vitreous makes them the best at heat dissipation²⁰⁸. However, the epiretinal location also has disadvantages: the presence of the retinal nerve fiber layer in between the electrodes and the RGC somas makes it difficult to stimulate them individually without simultaneously stimulating the RGCs axons that converge to the optic disc and pass just below the electrodes. This causes the phosphenes to have an elongated shape, as reported by patients

implanted with the Argus II, which can ultimately meaningfully worsen the expected visual acuity an epiretinal implant can restore²⁰⁹. However, it has recently been shown that this phenomenon can be mitigated by using longer pulses (more than 10 ms). Indeed, these longer pulses are preferentially recruiting the bipolar cells (called a network-mediated response) instead of the RGCs and their axons, resulting in a more focalized activation²¹⁰. An additional disadvantage of epiretinal implants is their anchorage based on the use of tacks. Indeed, it can result in retinal damage and long-term mechanical stability issues, which can lead to increased stimulating current thresholds due to the increased distance between the electrodes and the retina^{211–213}.

New epiretinal implants, like the POLYRETINA, are fabricated using flexible substrates such as PDMS, which enable to roll them to inject them through the small transscleral incision and to then unroll them once inside the eyeball. This permits to design of implants that conform to the eye curvature and cover the whole retina, and important improvement compared to stiffer previously developed devices, such as the Argus II, which were limited to only cover a small portion of the central retina²¹⁴.

The location of subretinal implants makes their implantation procedure more complex than their epiretinal counterparts, but on the other hand, they do not require any mechanical fixation to the retina as they are compressed in-between retinal layers which ensures their stability²¹⁵. Their closer contact with the target cells is also advantageous as it lowers their stimulation thresholds²¹⁶. However, due to their location in-between retinal layers, they have a poor heat dissipation capacity, which, paired with the fact that they may interfere with the diffusion of nutrient transport from the RPE, limits their maximal dimension that can be implanted without risks for the integrity of the retina²¹⁶. Furthermore, their maximal width is also constrained by the small space available to fit them between the degenerating photoreceptor layer and the RPE. This makes them usable only in conditions where a small portion of the visual field is lost, such as AMD, while condition like RP, or extremely late-stage and severe forms of AMD, require a full-field prosthesis such as epiretinal or optic nerve implants (which will be discussed in the next section). However, perhaps the greatest appeal of this approach is their target cells; indeed, unlike epiretinal implants that principally target the RGCs, they target the inner retinal circuitry and therefore are assumed to be able to restore a more naturalistic form of vision by better exploiting its natural processing^{215,217}.

Unlike the two other approaches already mentioned, suprachoroidal implants do not require a transvitreal surgery, making their implantation procedure less challenging²¹⁶. Nevertheless, it is not completely without safety issues, as the close proximity with the choroid vasculature results in some risk of hemorrhage, but also advantageously provides good heat dissipation capacity²¹⁶. Their location between the sclera and the choroid ensures they have good mechanical stability²¹⁸. While maybe less invasive, suprachoroidal implants are the furthest away from their target cells, the inner neurons of the retina. Hence, they require the highest current threshold to stimulate them, which aggravates the risk of damages due to over-stimulation and greatly diminishes their ability to deliver a focalized stimulation as a result of the larger current spread²¹⁹. This limitation makes the prospect of ever restoring a useful level of visual acuity with this approach more unlikely than with epiretinal or subretinal implants, which may explain the lower interest that has been given to this approach compared to the two others.

While the first retinal implants used standard electrode arrays to stimulate neurons, newer implants now use intraocular photo-diodes to stimulate them instead^{220,221}. This novel technological advancement can provide two improvements over to earlier approaches: it can either remove the need for internal powering supply or enable a camera-free system, and would be able to do both at once if the photocurrents generated were large enough to stimulate the retinal neurons on their own in normal light conditions. The photodiodes of

the PRIMA subretinal implant and the POLYRETINA epiretinal implant are directly powered by near-infrared light, that is intended to be projected on the retina by a setup pairing specialized goggles and a camera, that would enable combining the powering of the device and the visual information transmission in the same signal^{220,221}. This wireless power transmission totally removes the necessity of a permanent transscleral incision that was required to power older devices, which presented a risk of functional failure and chronic inflammatory reactions. Additionally, this enables the system to conduct more advanced image processing outside of the eye, which is typically constrained by the small size of other subretinal implants, which greatly minimizes the amount of internal circuitry that can be dedicated to this task^{222,223}. The Alpha-IMS design instead incorporates photo-diodes powered by a transmitter-receiver radiofrequency system. This removes the need for an external camera and permits to use of the natural movement of the eye instead, where other designs require the implanted patients to learn the unnatural and unintuitive process of scanning the visual scene by moving their head instead of their eyes, as the artificial images recreated would appear to follow the eye movement since the camera remains stationary²²²⁻²²⁴.

This is possible exclusively with retinal prostheses and not with prostheses stimulating any other part of the visual system, though technological advances in eye-tracking could potentially solve this issue in the future by making the camera follow the eye movement. Photodiode technology can be applied only to epi- and subretinal implants since the RPE would block the light access to a suprachoroidal implant, further consolidating the appeal of the first two approaches over the last one.

1.3.3 Optic nerve implants

Optic nerve stimulation in humans was first investigated two decades ago by Veraart and colleagues, who implanted a four-contact self-sizing cuff electrode around the intraocular portion of the optic nerve of a blind volunteer with late-stage retinitis pigmentosa²²⁵. They were able to elicit the apparition of phosphenes on a large portion of the visual field, with a satisfactory retinotopic matching between the electrode location and the phosphene position in the visual field (Figure 1-13a, b, and c). In a second study, by selecting a subset of the elicited phosphenes, they designed a close loop visual prosthetic system with a goggle-mounted camera, which permitted the volunteer to correctly identify character-like symbol and their orientation after a training period (Figure 1-13d and e)²²⁶. A second patient was implanted in a following study, confirming the ability of optic nerve stimulation to be used to artificially restore vision^{227,228}.

Despite this initial success, only a single human study targeting the optic disc of a patient instead of the nerve took place since²²⁹. The other recent studies are now focussing on the investigation of penetrating electrodes in animals as a way to improve the poor selectivity and mechanical stability of the cuff-electrode, as demonstrated by the progress in selectivity made in the field of peripheric nerve stimulation, with intraneural electrodes such as the TIME, LIFE, or SELINE electrode²³⁰⁻²³². One example of such approach is the C-sight project that investigates an optic nerve implant design based on electrical stimulation of the intraorbital segment of the optic nerve with penetrating metal electrodes in rabbits and cats^{233,234}.

Optic nerve prostheses target the RGC axons and thus share their cellular targets with epiretinal implants. However, unlike epiretinal prostheses, they stimulate the RGCs exclusively and not the remaining inner retina circuitry nor the axon of passage. While the latter is definitely advantageous, the former is up for debate. Indeed, even if stimulating the inner retina may result in a more naturalistic prosthetic vision, this relies on the assumption that the functional integrity of its inner circuitry is mostly conserved. This does not appear to be the case in a condition like retinitis pigmentosa, where important synaptic remodeling and

reorganization have been reported to take place in the inner retina, which could impair the effectiveness of the simulation^{235–239}.

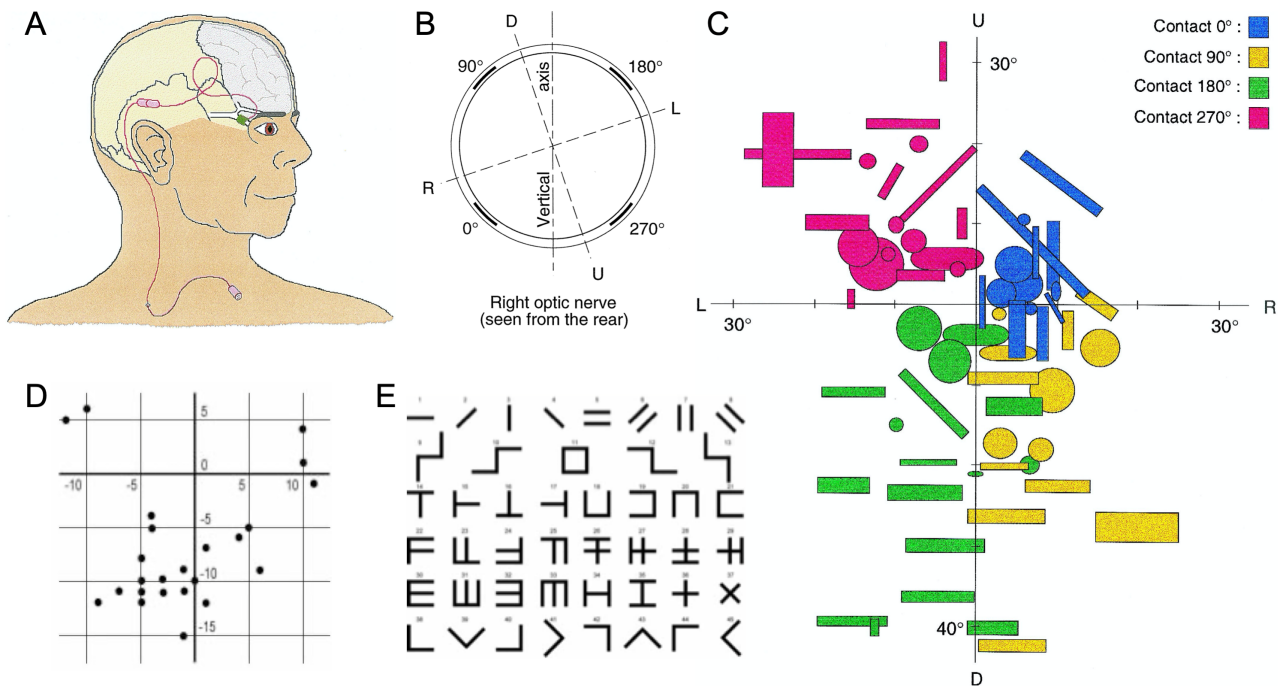


Figure 1-13 | Summary of the studies on electrical stimulation of the optic nerve in humans. (a) Schematic of the optic nerve stimulation setup. A four-contact self-sizing cuff-electrode is implanted around the pre-chiasmatic portion of the optic nerve of the blind patient. From Veraart et al., 1998²²⁵. (b) The orientation of the cuff-electrode around the optic nerve relative to the visual field axis. The four contacts of the cuff-electrode were slightly rotated in respect to the two visual field axes. The letters U, D, R, and L stand for the up, down, right, and left portions of the visual field and their respective representation in the optic nerve, which are inverted compared to the actual visual field. From Veraart et al., 1998²²⁵. (c) Retinotopy of the phosphenes produces with the four electrodes. The phosphenes are produced in the expected quadrants of the visual field based on the electrode locations. From Veraart et al., 1998²²⁵. (d) Selected phosphenes for the pattern recognition task. These are the phosphenes that were selected for the close-loop pattern recognition task. From Veraart et al., 2003²²⁶. (e) The list of the character-like symbols used during the pattern recognition task. The bottom line displays the L-shaped symbols used in a second task consisting of a pattern orientation discrimination. The volunteer reached approximately 60% and 100% scores in the 1st and 2nd tasks with a discrimination time of approximately 60 and 10 seconds respectively over the two days of the experiment. From Veraart et al., 2003²²⁶.

On the one hand, the small cross-section of the optic nerve is advantageous since it enables straightforward access to neurons originating from the whole visual field, something that retinal prostheses have struggled with in the past. On the other hand, this small size also raises the main technical concern with electrical stimulation of the optic nerve, which is the potential limitations in the maximal number of stimulating sites the optic nerve could accommodate compared to larger anatomical structures like the retina and V1. However, unlike the retina and V1, which are surfaces, the optic nerve is a volume and thus could accommodate a series of implants along its length, which could greatly increase the total number of stimulating sites available. Additionally, the fact that it is a volume also ensures that the optic nerve implants have a better long-term anchorage and mechanical stability than epiretinal implants and also guarantees a closer contact with their target cells. Optic nerve implants also have a broader range of applications than retinal implants, as they could potentially be used to address conditions such as severe trauma such as retinal detachment or eyeball trauma, or corneal opacities as they do not require optical transparency. Overall, optic nerve implants, like recent epiretinal implants, seem the best suited to address conditions such as retinitis pigmentosa, where most of the visual field is affected, while subretinal implants can be used to address AMD since it does not require full-field coverage as only the central visual field is affected.

1.3.4 Lateral geniculate nucleus prostheses

The LGN has initially been discarded as a potential target, presumably due to its location deep into the brain, which renders its access more impractical than other approaches. However, there has been a renewed interest in LGN stimulation following the recent development of deep brain stimulation, which has demonstrated that the thalamus is relatively easily surgically accessible^{240,241}.

Thanks to its location downstream in the visual path, an LGN prosthesis would be able to address conditions where the RGCs are lost, unlike retinal or optic nerve prostheses, such as glaucoma or ocular trauma. Additionally, the compact size of the LGN paired with the overrepresentation of the central visual field on its surface would allow developing a prosthesis that could combine a wide visual field with a high acuity central vision^{242,243}. Additionally, the anatomical segregation of the parvocellular pathway believed to encode fine details, and the magnocellular pathway that transmits motion-related signals could be advantageous to encode a more naturalistic neuroprosthetic input. The specific layers organization of the LGN could also potentially permit the restoration of color vision, something technically impossible when stimulating upstream anatomical structures of the visual path^{243,244}.

One disadvantage of the approach is that it requires a bi-lateral implant to cover the entirety of the visual field due to the post-chiasmatic location of the LGN²⁴². Furthermore, an LGN visual prosthesis would require the use of multiple electrodes spread into the small volume of the LGN in order to fully take advantage of its anatomical structure, something that the current large deep brain stimulation devices, which consist of only a few electrodes located on a single shaft, are not designed for.

Overall the LGN is an attractive target for the implantation of a neuroprosthetic device; however, the approach is in its infancy, so its feasibility remains speculative at this stage.

1.3.5 Cortical prostheses

Probably due to its very straight-forward access and its large surface area, the primary visual cortex was the first investigated target for a visual prosthesis, more than 50 years, with a pioneering study led by Brindley and Lewin where they induced phosphene using cortical electrical stimulation in a blind volunteer that she described as “like a star in the sky.”²⁴⁵.

These initial findings led to the development and the implantation of the first modern-day visual prosthesis prototype developed by Dobbelle, which consisted of an 8-by-8 electrode array placed on top of the surface of the occipital cortex of a blind volunteer, which allowed them to decipher 6 inches-tall character at a distance of 5 feet^{246–248}. This first attempt was followed by several complications and challenges, such as the absence of control on the number of phosphenes produced by each electrode, the interaction between the phosphenes produced, and pain and sporadic seizures caused by the high currents used^{246,249,250}. Furthermore, despite its large surface area, most of the visual cortex is located deep inside the calcarine fissure, which renders surface electrodes impractical²⁰⁷. In order to solve these issues, recent cortical implants have adopted intracortical microelectrodes arrays, such as the Utah array, which require lower current threshold thanks to their more intimate proximity with their neuronal targets and thus represent fewer risks of damage for the brain tissue²⁵¹.

In addition to its anatomical location, which facilitates its surgical access, its position at the end of the visual path also renders the visual cortex attractive compared to other upstream locations, since targeting it can

address all causes of blindness, except for cortical injuries and strokes²⁰⁶. However, the visual cortex is organized in a much more complex manner than upstream portions of the visual path, with neurons specifically tuned for different colors or stimuli orientations, making it unlikely to be able to evoke simple uniformly shaped phosphenes upon stimulation, and will likely need implants with stimulations paradigms specifically adapted for each individual patient^{207,252,253}.

1.3.6 Overview of interfaces for neural stimulation

There exists a large number of devices that can be used to stimulate the peripheral nervous system and the optic nerve. Two aspects of nerve interfaces are commonly used to classify them; their selectivity and their invasiveness, which are generally correlated²⁵⁴. Indeed, a device with high selectivity, which can be defined as the ability to stimulate a large number of small axonal sub-populations independently, requires that its electrodes are in close contact with these targets sub-population. This can only be achieved by puncturing the nerve to insert the device through it, which increases its invasiveness. The implantation of a device triggers an immune reaction called the foreign body response, which consists of an inflammatory reaction followed by the encapsulation of the device in a fibrotic tissue layer²⁵⁵. The high impedance of the fibrotic encapsulation increases the current thresholds necessary to recruit the neurons in the close vicinity of the device's electrodes, which can ultimately reduce the precision of the stimulation and alter the long-term performance of the device in chronic implantation conditions. The choice of the device must therefore be motivated by the level of selectivity requested by its specific target application to avoid excessive levels of invasiveness in order to minimize the foreign body response.

The least invasive types of nerve interfaces are the extraneural ones, which are located outside of the nerve. The cuff electrodes were the first types of nerve interface to be developed and form the main class of extraneural nerve interfaces. They generally consist of an insulating cylinder with electrodes on its inner surface that is wrapped around the nerve. While these devices are considered to be the least invasive nerve interface, they may still result in nerve damages; a too tight fit may compress the nerve, while a too-loose fit may result in an uneven spread of the pressure with increased pressure points at the extremities of the device. Cuff electrodes have poor selectivity since fibers in the central portion of the nerve have higher activation thresholds than the fibers in the periphery of the nerve in closer contact with their stimulating sites, making it impossible to stimulate the central fibers without also stimulating the fibers of the periphery of the nerve with standard current pulses²⁵⁶.

The flat interface neural electrode (FINE), a second extraneural device, aims to improve the selectivity of the cuff electrode by flattening the nerve in order to bring the fibers from the inner portion of the nerve closer to its stimulation sites²⁵⁷. This flattening of the nerve increases the perimeter of the nerve while maintaining its cross-section surface area, which allows having a larger number of stimulation sites than a cuff electrode for a nerve of the same diameter²⁵⁸.

The next types of nerve interfaces are the intraneural devices, which puncture the nerve's outer layer and penetrate through it, allowing for a much closer contact with the axons located in the inner portion of the nerve, and therefore improving their selectivity compared to extraneural electrodes. The first example of such type of device is the longitudinal intrafascicular electrode (LIFE), a thread-like device implanted along the nerve length²⁵⁹. The latest version of the device is polyimide-based and contains several stimulation sites along the length of the device²⁶⁰.

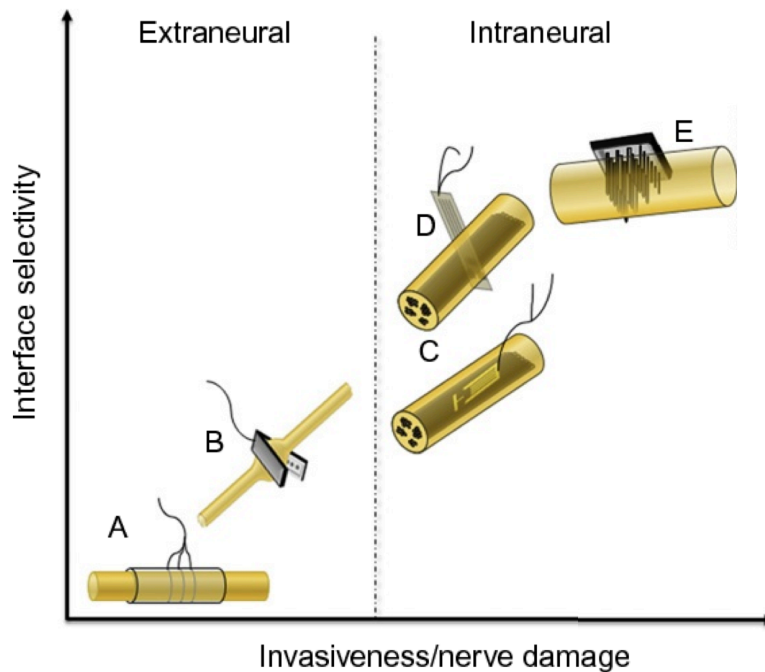


Figure 1-14 Different nerve interface for electrical stimulation. Schematic representation of the different stimulating nerve interface and their respective invasiveness and selectivity with the cuff electrode (a), the FINE (b), the LIFE (c), the TIME (d), and the Utah slanted array (e). Modified from Del Valle and Navarro 2013²⁵⁴.

A similar device is the transverse intrafascicular multichannel electrode (TIME), which is implanted perpendicularly to the nerve instead of parallelly to it like the LIFE, thus allowing to stimulate a large number of different axonal fibers population²⁶¹. The TIME has been shown to change position slightly in chronic conditions, therefore impairing its ability to consistently stimulate the same axonal populations²⁶². This led to the development of the self-opening intraneural electrode (SELINE), a modified version of the TIME which presents the particularity of having tiny wings on its sides that spread open inside the nerve upon retraction after its initial insertion. This guarantees an improved anchorage than the TIME electrode and therefore an improved selectivity in chronic implantation conditions^{232,263,264}. A slightly modified version of the original SELINE design optimized for optic nerve stimulation was used for the animal experiments reported in this thesis and will be described in more detail in the following chapter.

The last important intraneural electrode is the Utah slanted electrode array, an array of penetrating electrodes made out of silicone shanks of different lengths derived from the Utah electrode array initially designed as a cortical interface²⁶⁵. The latest version of the Utah slanted array has the highest electrode density of all the intraneural nerve interfaces, with a density of 25 electrodes per squared millimeters²⁶⁶. Since it is made out of silicone which is stiffer than the substrates typically used for the fabrication of the other nerve interfaces such as polyimide, it is also the device with the largest mechanical mismatch between it and the target neural tissue, which has been linked to increased foreign body response²⁶⁷. There has also been reports of poor insertion and only partial penetration through the perineurium in a human study²⁶⁸.

1.4 Thesis motivations and organization

Vision is arguably the sense which loss has the most negative impact on one's quality of life. Finding ways to restore even a rudimentary level of vision in blind patients thus has the potential to positively impact the lives of millions of people worldwide.

While several causes of blindness are treatable, others, such as AMD and retinitis pigmentosa, currently have no cure. In this context, visual prostheses have recently emerged as promising tools to potentially address these conditions. Electrical stimulation of the optic nerve presents several advantages compared to more commonly explored strategies for vision restoration, such as retinal and cortical implants: it requires a less complex surgical implantation procedure, is less invasive, and allows an easy access to cells originating from the whole visual field. We believe these advantages make it a compelling approach for vision restoration worthy of investigation.

So far, electrical stimulation of the optic nerve in humans has been limited to two preclinical studies where two patients were implanted with a stimulating nerve-cuff electrode. Due to the location of their stimulating electrodes, these types of interfaces are known to have poor selectivity, especially when it comes to stimulating the central portion of a nerve. This would greatly limit the quality of the image they can recreate and ultimately their usefulness to the blind patient. Furthermore, cuff electrodes have poor anchorage, which may lead to the displacement of their stimulating sites, and thus limit their potential use to design successful visual prostheses, as it would require to be able to elicit phosphenes at consistent locations over long implantation periods.

We propose to use an adapted version of the SELINE (self-opening intraneural electrode), which selectivity has previously been demonstrated in the rat sciatic nerve, in order to overcome the limitation of the cuff electrode. Indeed, we believe that the intraneural nature of the device will allow to selectively recruit the axonal fibers found deep in the center of the optic nerve and that its four self-opening wings, which have shown a never achieved stability that will be crucial for long term implantation. Furthermore, the SELINE is made in polyimide, which has a decreased stiffness and thus a decreased mechanical mismatch with the optic nerve compared to other potential multi-electrode arrays, such as the Utah slanted electrode array or other penetrating electrodes that have been used in optic nerve stimulation, which has already shown to improve the biocompatibility of the device and minimize the foreign body response its implantation elicits^{265,269}.

In our opinion, the optimal implantation location along the optic nerve is in the pre-chiasmatic region close to the optic chiasma, where the optic nerve fibers are retinotopically arranged. Unlike an intra-orbital implantation, this also avoids the risk of puncturing the central retinal vein and artery, which enter the optic nerve approximately at 10 mm from the eyeball.

The objective of the thesis is to develop a new experimental framework both in terms of *in vivo* animal experiments and data analysis that can be used for the validation of intraneural electrodes for vision restoration, such as the OpticSELINE used in the experiments reported in this thesis, as well as future improved devices not yet designed.

The results of the work conducted during the thesis are divided into two chapters. In the first one, we demonstrated the possibility of using the OpticSELINE to elicit electrically-evoked potentials (EEPs) of modulable magnitudes, and we used an independent component analysis (ICA) approach to show that it has some selectivity, which are two crucial steps in demonstrating the possibility to build a prosthetic device using this

approach. In the second chapter, we developed new methods to classify the EEPs origins and to quantify the EEPs similarity when classical methods failed, which in our opinion would be helpful in the future when the electrode density will be increased, thus leading to more similar EEPs signals that could not be distinguished by classical approaches.

Chapter 2 Spatially selective activation of the visual cortex via intraneural stimulation of the optic nerve

Postprint version of the article published in nature biomedical engineering volume 4 issue 2 (DOI: 10.1038/s41551-019-0446-8)

Authors: Vivien Gaillet ^{a, ‡}, Annarita Cutrone ^{b, ‡}, Fiorenzo Artoni ^{b, c, ‡}, Paola Vagni ^a, Ariastity Mega Pratiwi ^a, Sandra Alejandra Romero ^a, Dario Lipucci Di Paola ^b, Silvestro Micera ^{a, b} and Diego Ghezzi ^a

^a Medtronic Chair in Neuroengineering, Center for Neuroprosthetics and Institute of Bioengineering, School of Engineering, École polytechnique fédérale de Lausanne, Geneva, Switzerland.

^b The BioRobotics Institute, Scuola Superiore Sant'Anna, Pisa, Italy.

^c Bertarelli Foundation Chair in Translational Neuroengineering, Center for Neuroprosthetics and Institute of Bioengineering, School of Engineering, École polytechnique fédérale de Lausanne, Geneva, Switzerland.

[‡] These authors contributed equally to this work

Authors contributions : V.G. designed the stimulation protocol and performed the modelling and simulation, blind source separation and data analysis. A.C. designed and fabricated the OpticSELINE and performed mechanical and electrochemical characterizations. F.A. conceived and performed the blind source separation approach. P.V. performed in vivo and histological experiments. A.M.P. performed the modelling and simulation. S.A.R. participated in the design of the stimulation protocol and data analysis. D.L.D.P. participated in the design and microfabrication of the OpticSELINE and performed mechanical characterizations. S.M. supervised the activities related to electrode development and the blind source separation approach. D.G. designed the study, led the project and wrote the manuscript. All the authors read, edited, and accepted the manuscript.

2.1 Abstract

Retinal prostheses can restore a functional form of vision in patients affected by dystrophies of the outer retinal layer. Beyond clinical utility, prostheses for the stimulation of the optic nerve, the visual thalamus or the visual cortex could also serve as tools for studying the visual system. Optic-nerve stimulation is particularly promising because it directly activates nerve fibres, takes advantage of the high-level information processing occurring downstream in the visual pathway, does not require optical transparency and could be effective in cases of eye trauma. Here we show, in anaesthetized rabbits and with support from numerical modelling, that an intraneural electrode array with high mechanical stability placed in the intracranial segment of the optic nerve induces, on electrical stimulation, selective activation patterns in the visual cortex. These patterns are measured as electrically evoked cortical potentials via an ECoG array placed in the contralateral cortex. The intraneural electrode array should enable further investigations of the effects of electrical stimulation in the visual system and could be further developed as a visual prosthesis for blind patients.

2.2 Introduction

Visual prostheses have recently emerged as tools to fight blindness, a medical condition affecting more than 30 million people worldwide²⁷⁰. Starting from early pioneering works^{271,272}, over the past 50 years,

several types of visual prostheses have been proposed and classified by their location along the visual pathway^{32,273}, including subretinal²²⁴, epiretinal²⁷⁴, suprachoroidal²⁷⁵, optic-nerve²⁷⁶, thalamic²⁴³ and cortical prostheses²⁷⁷. Retinal implants quickly became the preferred strategies, since they can benefit from natural information processing along the visual pathway²⁷⁸. In various clinical trials, retinal prostheses have demonstrated the capability to restore a functional form of vision^{214,222}. Today, several research groups are developing retinal prostheses, with a special emphasis on light-driven photovoltaic implants^{220,221,279–281}. However, optic-nerve stimulation is also an attractive strategy, since it bypasses the entire retinal network and directly activates nerve fibres. Further, like epiretinal prostheses, it still takes advantage of the high-level information processing occurring downstream in the visual pathway. Moreover, optic-nerve stimulation could be effective in cases of severe trauma (such as retinal detachment or eyeball trauma) and does not require optical transparency (for example, in the case of corneal opacities). Indeed, history of retinal detachment, trauma and severe strabismus are among the contraindications for the Argus II epiretinal prosthesis.

Optic-nerve stimulation was pioneered with the implantation in the intracranial segment of a blind subject of a four-contact self-sizing spiral cuff epineural electrode array²²⁵, in which electrical stimuli elicited localized phosphenes. After a few months of training and psychophysical testing, the patient was able to distinguish line orientations as well as shapes and symbols despite using only four electrodes. Another patient was later implanted with an eight-contact electrode²²⁷, confirming the possibility of restoring functional vision via optic-nerve stimulation^{226,228,282}. However, in these trials, the induced phosphenes were reported as irregular; the use of spiral cuff epineural arrays could be the cause²⁸³ because of their limited mechanical stability. Following these results, the C-Sight project is currently investigating an optic-nerve prosthesis based on an array of three penetrating metal electrodes to stimulate the intraorbital segment of the optic nerve in rabbits^{284,285} and cats²³⁴. This project employs penetrating platinum–iridium electrodes, which are characterized by high stiffness (Young’s modulus of approximately 100 GPa) and rigidity, inducing a large mechanical mismatch with the nerve, which could have negative consequences for chronic implantation. Conversely, transverse intrafascicular multichannel electrode (TIME) arrays, microfabricated using thinfilm technology, have already demonstrated their superior capability in peripheral nerve stimulation^{286,287}. TIME arrays showed better mechanical compliance (Young’s modulus of approximately 1GPa and high flexibility) compared with penetrating metal electrodes, and higher selectivity in fibre stimulation compared with spiral cuff epineural arrays^{230,288}. More recently, a self-opening intraneural electrode (SELINe) array demonstrated improved mechanical stability compared with TIME arrays²³² as well as high biocompatibility over a period of six months²⁶⁹. In this work, we exploited OpticSELINe, a modified version of the previously described SELINe array^{232,269}, as a visual prosthesis based on optic-nerve stimulation.

2.3 Results

2.3.1 Electrode array design and characterization

The OpticSELINe is a polyimide-based looped electrode array designed in agreement with the anatomical structure of the rabbit’s optic nerve, which has a mean (\pm s.d.) diameter of 1.45 ± 0.10 mm (Supplementary Supplementary Figure 2-19). Each side has a total length of 33 mm, a maximum width of 3 mm and an overall thickness of $12\mu\text{m}$ (Figure 2-1a). A 35mm polyimide-based extension flat cable enables connection between the electrode array and the head-fixed plug connector. Each side of the OpticSELINe has six stimulating electrodes (each with an area of 0.008 mm^2) and a reference and a ground electrode outside the active area (Figure 2-1b). Two three-dimensional flaps extend from both sides of the main body and carry two

electrodes each; two more electrodes are located on each side of the main body. Each flap has a width of 0.15mm and a length of 0.48mm. The width of the active area is 0.43mm and the length is 1.25mm. Four alignment bars (width of 0.1mm) were included to ease the insertion procedure and verify that the active area is located inside the optic nerve (Figure 2-1c). The insertion procedure follows a standardized technique that was previously validated in the peripheral nerves of both animals²⁶⁹ and humans^{286,287}. A suture with a needle guides the OpticSELINE transversally into the nerve until the electrode enlargement is reached (used as a stopper); at this stage, the four alignment bars are visible outside of the nerve. The OpticSELINE is then slightly pulled back until only three alignment bars are visible to anchor the flaps into the nerve (Figure 2-1d, and e).

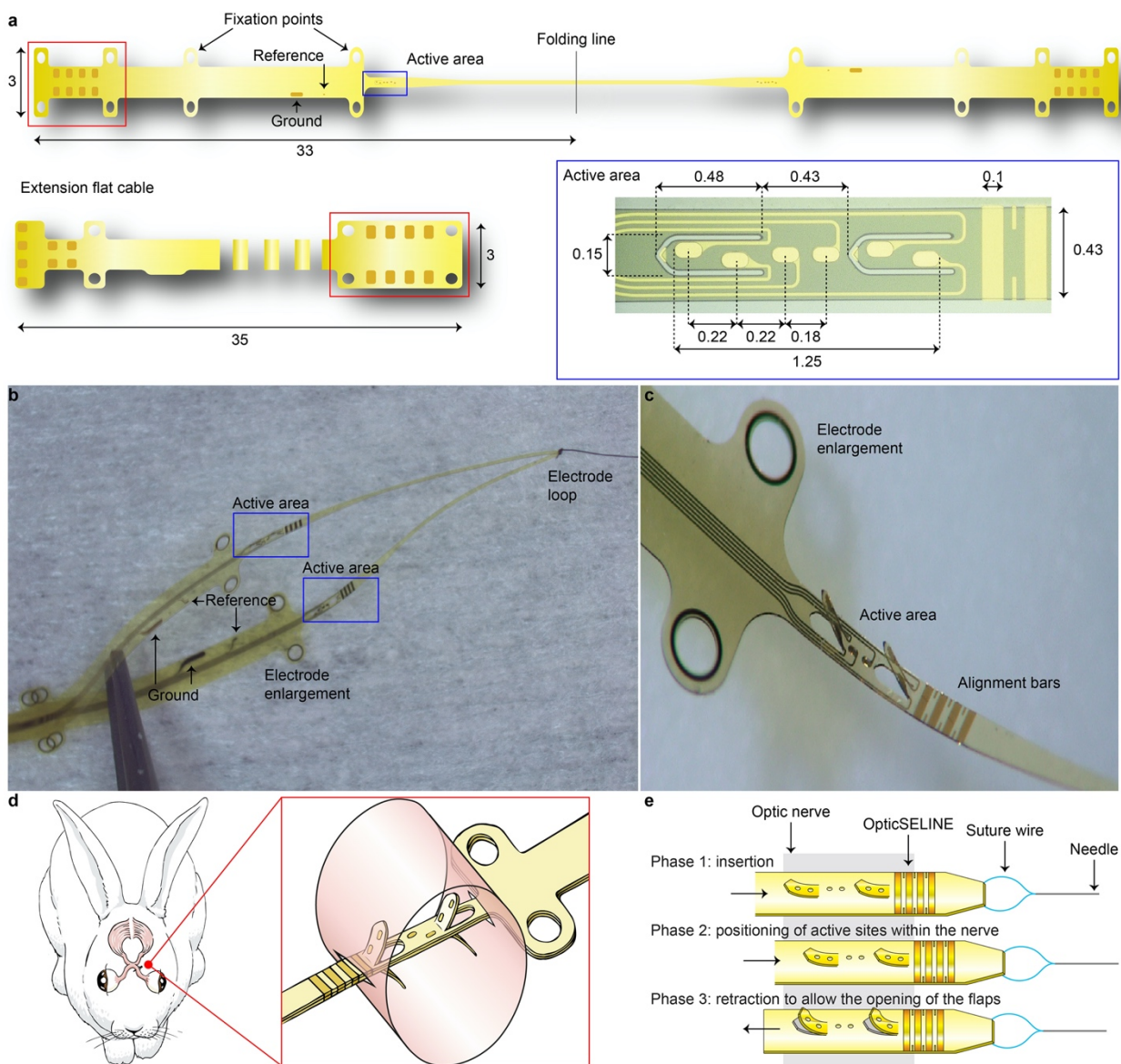


Figure 2-1 | The intraneural electrode array OpticSELINE. (a) Sketch of the OpticSELINE. The red box highlights the connection area between the electrode and the flat cable terminated with an Omnetics connector mounted on a printed circuit board (not shown). The blue box highlights one active area where two flaps and six electrodes are visible. Dimensions are in mm. (b) Photograph of the OpticSELINE, showing the looped structure with two active areas. (c) Magnified view of one side of the OpticSELINE, showing the active area with the flaps after three-dimensional shaping, the electrodes and the alignment bars. The electrode enlargement is used as a stopper to avoid excessive insertion of the array within the nerve. (d) Sketch of the OpticSELINE implanted in the rabbit optic nerve. The red box shows details of the implanted OpticSELINE in the optic nerve (cylindrical shape). (e) Schematic of the insertion procedure.

First, we characterized both the electrochemical and mechanical properties of the OpticSELINE. Cyclic voltammetry was performed to determine the charge storage capacity of the electrodes (Figure 2-2a) before and after a passive accelerated-ageing equivalent to an implantation time of 6.4 months (6 d at 87 °C)²⁸⁹. The mean (\pm s.d.) charge measured before (27.95 ± 14.28 nC) and after (29.55 ± 14.70 nC) ageing were not significantly different (Figure 2-2b); $n = 18$ electrodes from 4 OpticSELINEs; $P = 0.75$, two-tailed paired t-test). Given the small electrode area (0.008mm^2), these values of charge storage capacity (0.35 and 0.37 mC cm^{-2} , respectively, before and after ageing) are comparable to the values found in the literature for gold microelectrodes²⁹⁰. Similarly, we performed impedance spectroscopy (Figure 2-2c); the mean (\pm s.d.) magnitude at 1 kHz was not significantly different before (83.52 ± 44.27 k Ω) or after (77.79 ± 34.86 k Ω) ageing (Figure 2-2d; $n=30$ from 4 OpticSELINEs; $P=0.18$, two-tailed paired Wilcoxon test).

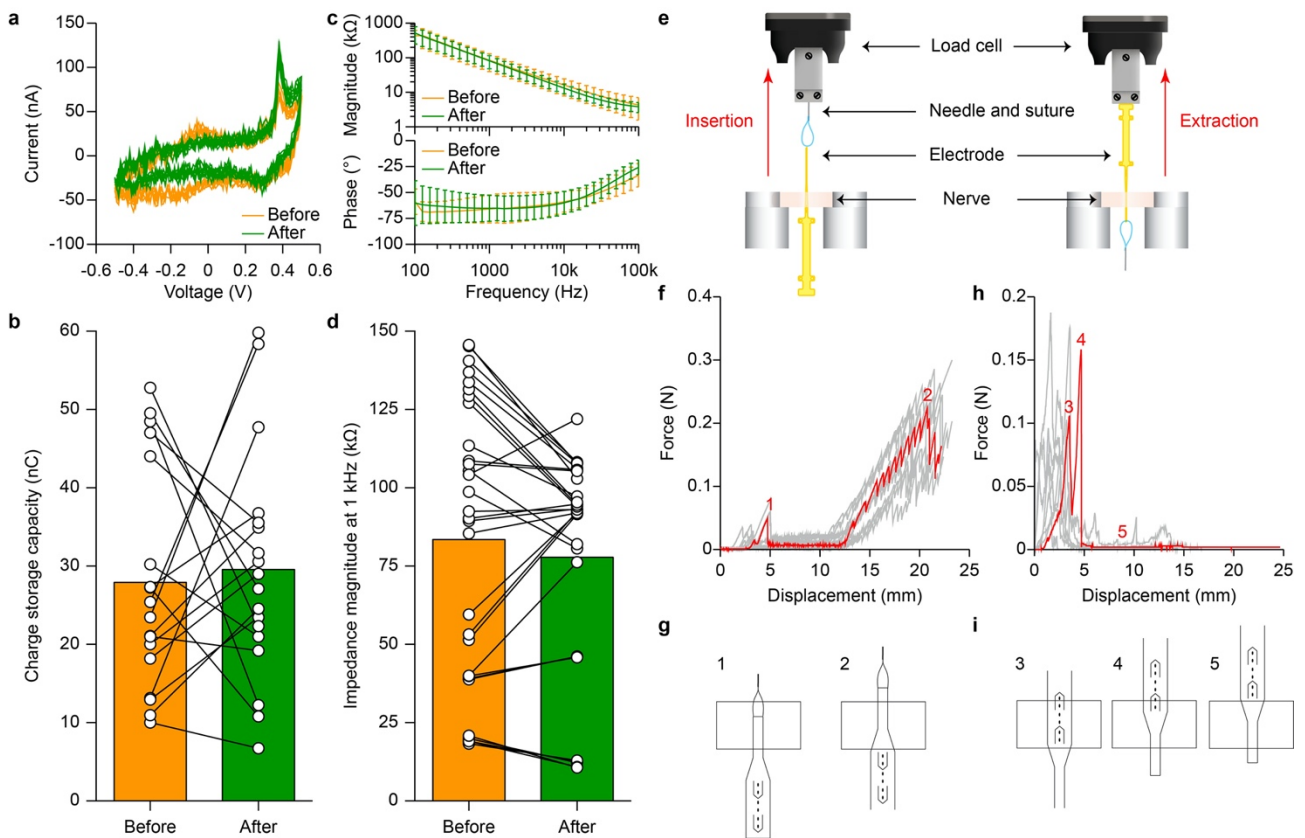


Figure 2-2 | Electrochemical and mechanical characterization. (a) Cyclic voltammetry performed on the electrodes before (orange) and after (green) passive accelerated ageing. Representative example of 1 electrode with an overlay of 10 repetitions. Experiment repeated on $n = 18$ electrodes from 4 OpticSELINEs. (b) Quantification of the mean (\pm s.d.) charge storage capacity ($n = 18$ electrodes from 4 OpticSELINEs). (c) Mean (\pm s.d.) magnitude (top) and phase (bottom) of the electrode impedances before (orange) and after (green) passive accelerated ageing ($n = 30$ electrodes from 4 OpticSELINEs). (d) Quantification of the mean (\pm s.d., $n = 30$ electrodes from 4 OpticSELINEs) impedance magnitude at 1 kHz. (e) Schematic of the ex vivo insertion (left) and extraction (right) experiments in explanted optic nerves from New Zealand white rabbits. (f) Forces during insertion in the optic nerve. Several insertion trials ($n = 10$ trials) are shown in grey. A selected example (red) is labelled with the different phases of insertion. (g) Sketch showing the different phases of insertion (phase 1 and phase 2). (h) Forces during extraction from the optic nerve. Several extraction trials ($n = 10$ trials) are shown in grey. A selected example (red) is labelled with the different phases of extraction. (i) Sketch showing the different phases of extraction (phases 3, 4 and 5).

A mechanical characterization was performed to verify the compatibility of the electrode array with the insertion forces and the stability within the optic nerve of New Zealand white rabbits. During insertion experiments (Figure 2-2e left), two major force peaks were observed (Figure 2-2f and g), corresponding to the insertion of the loop inside the nerve (peak 1) and to the entry of the enlarged area of the device (peak 2). The mean (\pm s.d., $n = 10$ trials) insertion forces are 32.5 ± 22.7 mN (peak 1) and 223.4 ± 92.2 mN (peak 2). The

stability of the electrode within the nerve was evaluated with an extraction experiment (Figure 2-2e right). During extraction, two major force peaks were observed (Figure 2-2h and i), corresponding to the force necessary to extract the three-dimensional flaps (peaks 3 and 4), followed by a flat phase relative to the slippage of the loop through the nerve (5). The mean (\pm s.d., $n = 10$ trials) extraction forces are 101.2 ± 36.2 mN (peak 3) and 100.3 ± 38.5 mN (peak 4), 30 times larger than the mean (\pm s.d.) force required to extract a similar electrode array without three-dimensional flaps (3.2 ± 0.5 mN; $n=4$ trials). This latter value is similar to what was previously measured in the rat sciatic nerve³³. This confirms that the three-dimensional flaps enhance the anchorage of the OpticSELINE within the nerve and provide better mechanical stability compared to TIME electrodes.

2.3.2 Visual stimulation

In the first set of rabbits, we characterized visually evoked cortical potentials (VEPs) on flash stimulation (4ms, Ganzfeld white LED; Figure 2-3a). The peak amplitudes (PAs) and latencies (PLs) of the two major peaks present in the VEP (N1 and P1) were measured using an electrocorticography (ECoG) electrode array (Figure 2-3b). The ECoG consists of a 4×8 array with $200 \mu\text{m}$ platinum electrodes with a 1mm pitch (E32-1000-30-200; NeuroNexus). The ECoG was placed over V1 visual cortex; given its small size, it is unlikely that it covers other areas than V1. However, we cannot formally exclude this possibility. We stimulated each rabbit on both eyes (ipsilateral and contralateral relative to the ECoG array) with flashes of increasing luminance levels (0.1, 0.5, 1, 5, 10 and 30 cd s m^{-2}). As expected, the strongest and fastest response occurred for contralateral stimulation (Figure 2-3c), since in albino rabbits, 90 to 95% of the optic-nerve fibres decussate at the level of the chiasm²⁹¹. The cortical activation for ipsilateral stimulation appeared only for luminance levels higher than 1 cd s m^{-2} , at which value the response to the contralateral stimulation was already saturated (Figure 2-3d). As previously reported²³³, the mean (\pm s.e.m., $N=9$ rabbits) P1 PL in contralateral stimulation started at 33.93 ± 2.59 ms for low luminance levels (0.1 cd s m^{-2}) and reached a plateau latency of 23.28 ± 1.86 ms for luminance levels higher than 5 cd s m^{-2} (Figure 2-3e). The mean (\pm s.e.m.) N1 PLs in contralateral stimulation were also comparable with previously reported data²³³ (Figure 2-3e).

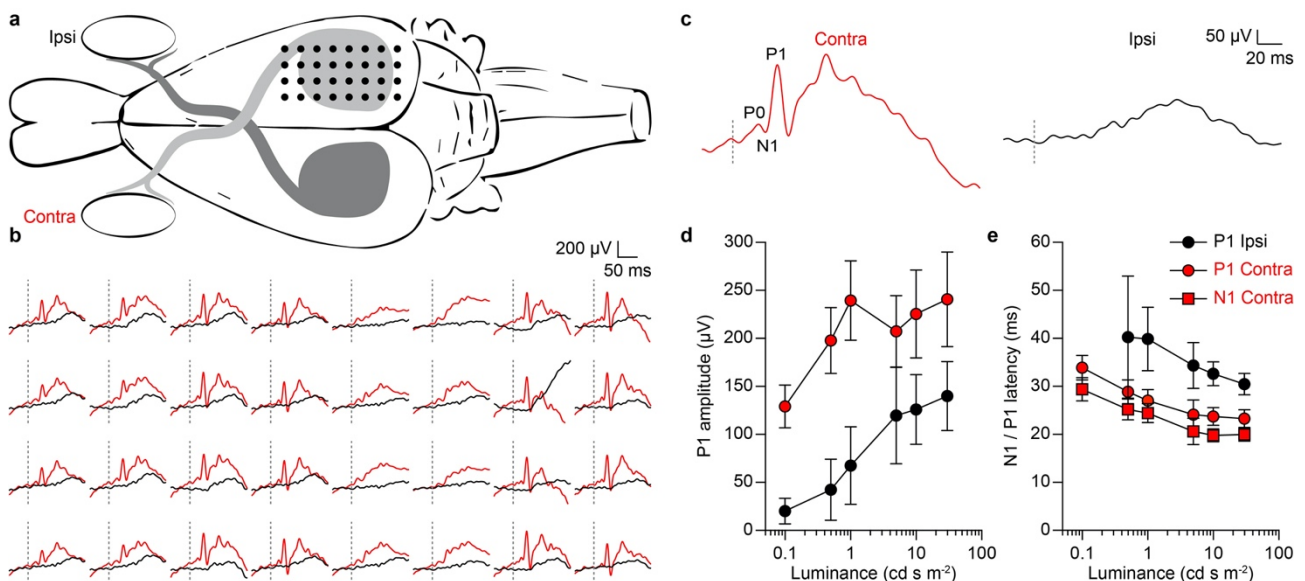


Figure 2-3 | Visually evoked cortical potentials. (a) Schematic diagram (top view) of the placement of the ECoG array (black dots) over the rabbit visual cortex. Recordings of VEPs were performed with the ECoG array upon flash stimulation (4 ms, Ganzfeld white LED) of both the ipsilateral (black) and contralateral (red) eye. (b) Example of traces (synchronous average of 10 responses) to a flash illumination of 0.5 cd s m^{-2} at the ipsilateral (black) or contralateral (red) eye. The dashed lines represent the occurrence of the flash.

Experiment repeated on N = 9 rabbits. **(c)** Example traces obtained from the average of the 32 recording channels (shown in b) for both ipsilateral (black) and contralateral (red) stimulation. P0, N1 and P1 peaks are visible (N for negative potential and P for positive potential). The dashed lines represent the occurrence of the flash. Experiment repeated on N = 9 rabbits. **(d and e)** Quantification of the P1 PA and PL as a function of the flash luminance. Each data point is the mean (\pm s.e.m.) of N = 9 rabbits. For each rabbit, ten consecutive recordings were averaged. For each recording, the 32 recording channels were averaged.

2.3.3 Electrical stimulation

In a second set of rabbits, we implanted the OpticSELINE transversally into the optic nerve from the lateral to the medial side. Because of the high percentage of fibre decussation at the level of the chiasm²⁹¹, electrically evoked cortical potentials (EEPs) were measured by an ECoG array in the contralateral visual cortex (Figure 2-4a and b). Cathodic first asymmetrically balanced (1:5) electrical stimuli were used. A previous report demonstrated that the ratio 1:5 is a good compromise between total pulse duration and stimulation efficiency²⁷. The same study also showed that placing the balancing anodic phase before the cathodic stimulation phase with a 1:5 ratio has no influence on the stimulation efficiency. Moreover, we did not introduce any interphase gap, since it has been demonstrated to have a significant effect only with symmetrically balanced stimuli²⁸⁵. Electrical stimulation consisted of a single biphasic pulse, unless stated otherwise. Upon electrical stimulation of the optic nerve, we found that both N1 and P1 PAs increased with the current amplitude of the stimulus (Figure 2-4c). To limit the overall experimental time for each rabbit and to avoid nerve fatigue due to repetitive stimulations (Supplementary Supplementary Figure 2-210a), we used only six electrodes of the OpticSELINE, located on the top side (from 1 to 6), unless stated otherwise.

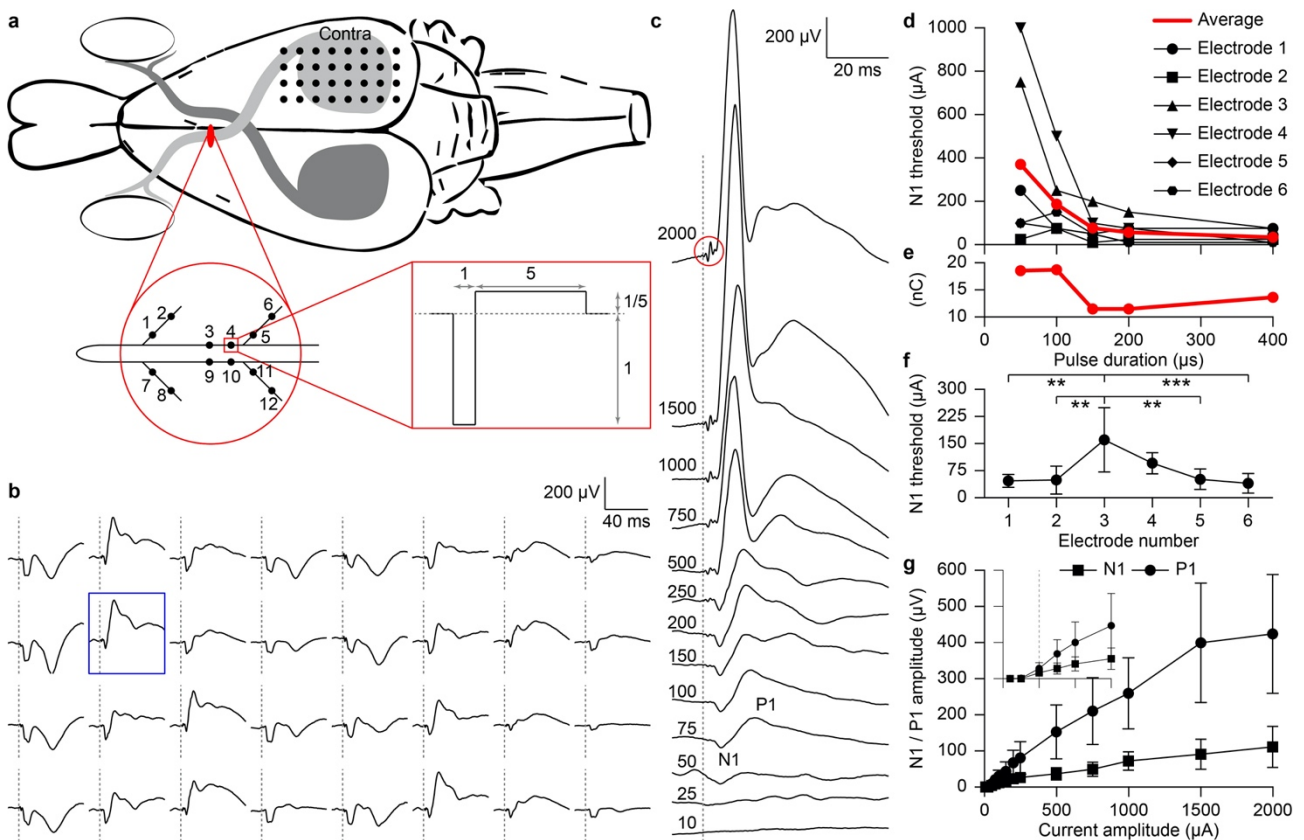


Figure 2-4 | Electrically evoked cortical potentials. (a) Schematic diagram (top view) of the placement of the OpticSELINE in the rabbit optic nerve and of the ECoG array (black dots) over the rabbit visual cortex. The enlarged red circle shows the nerve cross-section with the implanted OpticSELINE. The electrodes are each labelled with a number. EEPs were evoked via the implanted OpticSELINE with biphasic current pulses. The enlarged red box shows the biphasic current pulse delivered from electrode 4. **(b and c)** Example of traces (synchronous average of 10 responses) to a current pulse of 250 μ A and 150 μ s delivered from electrode 4. The dashed lines represent the occurrence of the current pulse. The blue box highlights 1 recording electrode, the responses of which

(synchronous average of ten responses) to increasing current pulses (left numbers in μA) of $150\ \mu\text{s}$ are visible in panel c. The appearance of N1 and P1 peaks is visible. The dashed line shows the occurrence of the current pulse. The red circle shows the stimulation artefact. Experiment repeated on $N = 4$ rabbits. **(d)** N1 activation thresholds in $N = 1$ rabbit as a function of the pulse duration. The red line and circles are the average of the $n = 6$ electrodes of the OpticSELINE (from 1 to 6, top side). **(e)** The average activation threshold is converted into the charge delivered. **(f)** Mean (\pm s.e.m., $N = 4$ rabbits) activation thresholds as a function of the OpticSELINE electrode (from 1 to 6, top side; $p < 0.001$, $F = 6.55$, one-way ANOVA, Tukey's multiple comparisons test). **(g)** Mean (\pm s.e.m., $N = 4$ rabbits) PAs of N1 (squares) and P1 (circles) for current pulses of $150\ \mu\text{s}$ as a function of the current amplitude. The inset shows a magnification from 0 to $150\ \mu\text{A}$ (x axis) and from 0 to $90\ \mu\text{V}$ (y axis); the dashed line is $50\ \mu\text{A}$. For each rabbit, ten consecutive recordings were averaged. PAs were quantified for each stimulating electrode of OpticSELINE from the averaged response of the 32 recording electrodes. The resulting values were averaged between stimulating electrodes.

First, we identified the N1 current threshold (that is, the minimum current required to induce the N1 peak in the EEP) using an automated peak detection algorithm followed by visual inspection and validation. To quantify the N1 current threshold, for each stimulating electrode of the OpticSELINE, we selected among the 32 recording electrodes the one with the highest N1 PA within the series (called the N1 leading channel). In the first rabbit (Figure 2-4d), we determined the N1 current threshold as a function of the pulse duration (50, 100, 150, 200 and $400\ \mu\text{s}$, cathodic phase). The N1 current threshold decreased with increasing pulse duration. However, for pulses shorter than $100\ \mu\text{s}$, there was a minimal effect on the charge (product of the current amplitude per the phase duration) required to induce N1 (Figure 2-4e). Then, the charge dropped by increasing the pulse duration from 100 to $150\ \mu\text{s}$ and remained stable for longer pulses (Figure 2-4e). For pulse durations of $150\ \mu\text{s}$, the mean (\pm s.d., $n = 6$ electrodes in $N=1$ rabbit) current threshold was $76.77 \pm 66.38\ \mu\text{A}$, and the charge threshold was $11.50 \pm 10.02\ \text{nC}$. The electrodes located on the main body (electrodes 3 and 4) showed a N1 current threshold higher than the other electrodes (1, 2, 5 and 6) located on the flaps, in particular for short pulses (Figure 2-4d).

On the basis of the previous results, in all subsequent experiments ($N=4$ rabbits), we fixed the first cathodic phase duration to $150\ \mu\text{s}$. Under this condition, we determined a mean (\pm s.e.m., $N = 4$ rabbits) N1 threshold of $74.03 \pm 13.33\ \mu\text{A}$, which corresponded to $11.10 \pm 2.00\ \text{nC}$. These values were very similar to those obtained in the first rabbit at $150\ \mu\text{s}$. We also found a similar and statistically significant trend ($P < 0.001$, $F = 6.55$, one-way ANOVA, Tukey's multiple comparisons test; $N = 4$ rabbits), with the electrodes on the main body showing a higher N1 current threshold (Figure 2-4f). This could be explained by the fact that in the pre-chiasmatic segment of the optic nerve, the large diameter fibres are localized more in the periphery of the nerve (Supplementary Supplementary Figure 2-311). Indeed, from the histological examination of an optic-nerve sample, we found that the fibre diameters within the whole nerve followed a unimodal distribution with a median of $0.79\ \mu\text{m}$ and a mode of $0.47\ \mu\text{m}$. In the central area (green square in Supplementary Figure 2-311a), the median of the distribution was lower than in the periphery (0.75 and $0.82\ \mu\text{m}$, respectively; $P < 0.0001$, unpaired t-test). The mean (\pm s.d.) fibre density was not different between the centre and periphery (0.19 ± 0.02 versus 0.19 ± 0.04 , fibres μm^{-2} ; $P = 0.40$, unpaired t-test). The overall mean (\pm s.d.) fibre density was 0.19 ± 0.03 fibres μm^{-2} . However, there may be alternative explanations related to the insertion procedure, which could affect more electrodes on the main shaft by increasing their N1 current threshold.

Next, we applied a detection algorithm to determine the N1 and P1 PAs and PLs. The mean (\pm s.e.m., $N = 4$ rabbits) N1 and P1 PAs showed monotonic growth as a function of the current amplitude, and the P1 PA saturated above $1,500\ \mu\text{A}$ (Figure 2-4g). From the average PAs, it was also apparent that both N1 and P1 became higher than zero, starting from a current pulse of $50\ \mu\text{A}$ (Figure 2-4g dashed line in the inset). Concerning the PLs, N1 PL was stable over the current range of stimulation used (approximately 3.5ms), whereas P1 PL slightly decreased from 7.45 to $5.68\ \text{ms}$ with the increase in the current amplitude (Supplementary

Figure 2-412). Qualitatively, PLs in EEPs were shorter than in VEPs by approximately 15ms, as previously reported²⁷. This was expected, since electrical stimulation bypasses the transduction step performed by photoreceptors. As a control, in one rabbit, we also verified that, similar to visual stimulation, electrical stimulation induced a small activation of the ipsilateral visual cortex only for high current amplitudes (Supplementary Figure 2-513)

2.3.4 Cortical activation maps

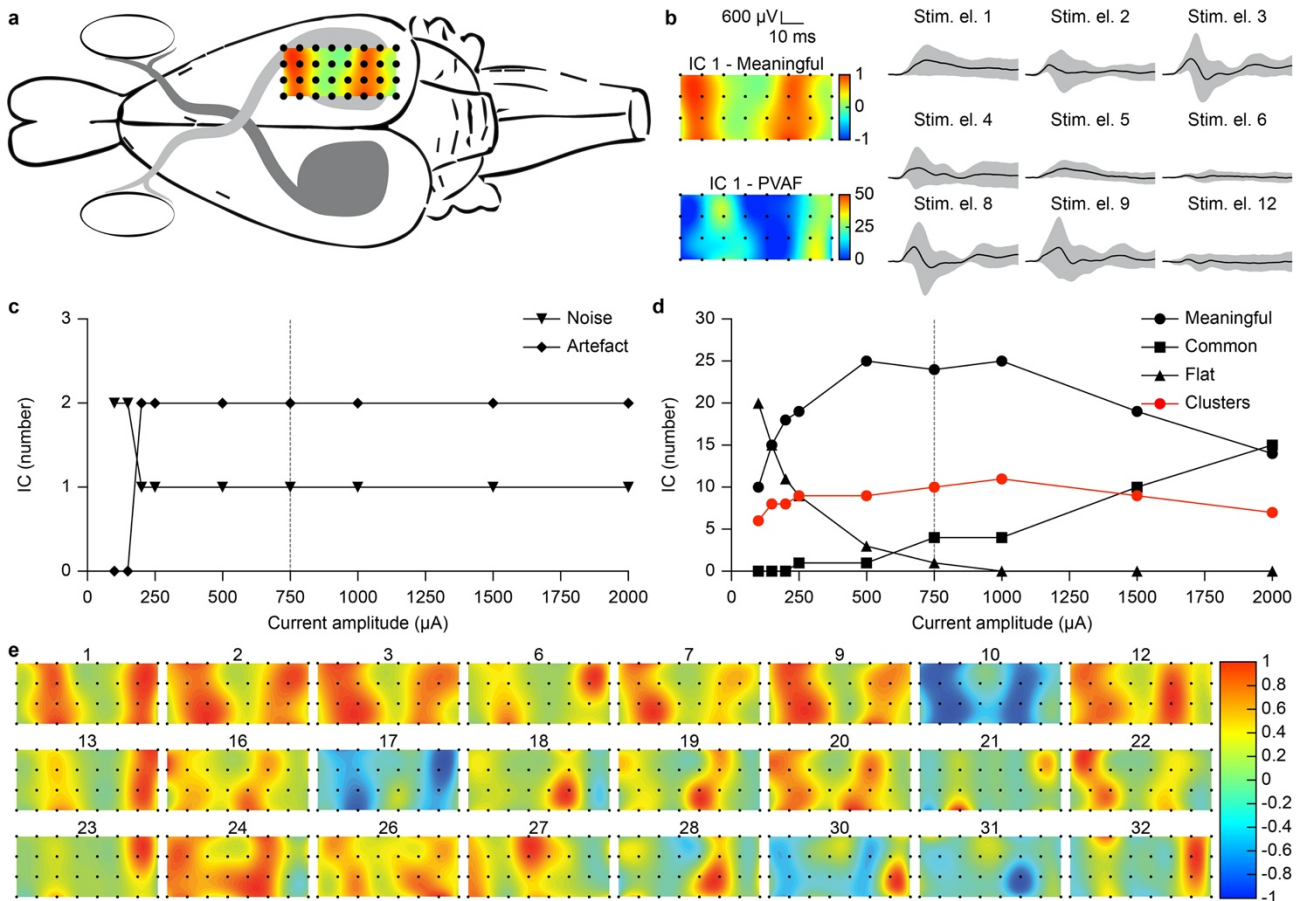


Figure 2-5 | Cortical activation maps. (a) Schematic diagram (top view) of the rabbit visual cortex with an example of an activation map corresponding to IC1 projected onto the ECoG array. (b) Example of the activation map (the colour code is the weight assigned to the IC), the percentage of variance accounted for (PVAf) and the time courses of a representative meaningful component (IC 1). A time course is shown for each stimulating electrode (stim. el.) of the OpticSELINE. The black lines are the mean of 10 repetitions and the grey shadings are the standard deviation. (c) Number of ICs classified as artefact or noise as a function of the current amplitude. At low currents (100 and 150 μA), the artefact cannot be detected. Noise ICs decrease from 2 to 1 because IC 4 is first detected as noise IC (100 and 150 μA) and later ($>200 \mu\text{A}$) detected as artefact IC. The dashed line shows the number of ICs obtained for a current amplitude of 750 μA , the reference value used in e. (d) Number of ICs classified as flat, common and meaningful as a function of the current amplitude. The number of meaningful clusters is plotted in red. The dashed line shows the number of ICs and clusters obtained for a current amplitude of 750 μA , the reference value used in e. (e) The 24 meaningful ICs are present in distinct regions of the visual cortex. The colour code is the weight assigned to the IC. Representative example from N = 1 rabbit with a current amplitude of 750 μA . Experiment repeated on N = 4 rabbits.

We then investigated the spatial characteristics of cortical activation upon intraneural stimulation of the optic nerve. A blind-source separation approach based on independent component analysis (ICA)²⁹²⁻²⁹⁵ was used to quantitatively extract differences between the EEPs resulting from the stimulation through different electrodes of the OpticSELINE. We hypothesized that each EEP is composed of ‘shared’ and ‘meaningful’ components: the shared components characterized by similar time courses regardless of the stimulating electrode activated in the OpticSELINE, and the meaningful components having time courses specific

to a single stimulating electrode (or to a small subset at most). For each rabbit, the ICA was performed on the 32 ECoG recordings to highlight the presence of meaningful components that may be hidden by the shared cortical signal. ICA linearly projects the 32 original time courses onto 32 new maximally independent time courses, called independent components (ICs), as weighted sums of the original time courses. We classified the ICs into different categories on the basis of their time course (Supplementary Figure 2-614): artefact (that is, containing the stimulation artefact), noise (that is, containing a high-frequency signal), flat (that is, not containing any peak), common (that is, having a similar time course regardless of the stimulating electrode) and meaningful (that is, having different time courses as a function of the stimulating electrode). Artefact, noise, flat and common ICs were considered shared components. The region of the visual cortex in which each IC is present was determined by plotting the activation map of each IC on the 32 electrodes of the recording array (Figure 2-5a).

In a representative example (N=1 rabbit, current amplitude of 750 μ A), all 12 stimulating electrodes of OpticSELINE were used, and among the 32 ICs, 24 were labelled as meaningful, 4 as common, 1 as flat, 1 as noise and 2 as artefact (Figure 2-5b and Supplementary Figure 2-715). However, 9 stimulating electrodes (electrodes: 1, 2, 3, 4, 5, 6, 8, 9 and 12) out of 12 resulted in meaningful cortical activation, whereas 3 (electrodes: 7, 10 and 11) induced only flat responses (Supplementary Figure 2-816 black traces). By back-projecting only the meaningful ICs onto the original channel space, the original data could also be filtered to highlight only the meaningful components (Supplementary Figure 2-816 red traces). By increasing the current amplitude of the pulse, the number of ICs classified as meaningful increased, reaching its maximum value between 500 μ A and 1,000 μ A and then decreasing (Figure 2-5d). This was probably due to the beginning of the saturation of the cortical response; therefore, more ICs are classified as common instead of meaningful. The activation maps of the 24 meaningful ICs show that they are present in distinct regions of the visual cortex (Figure 2-5e).

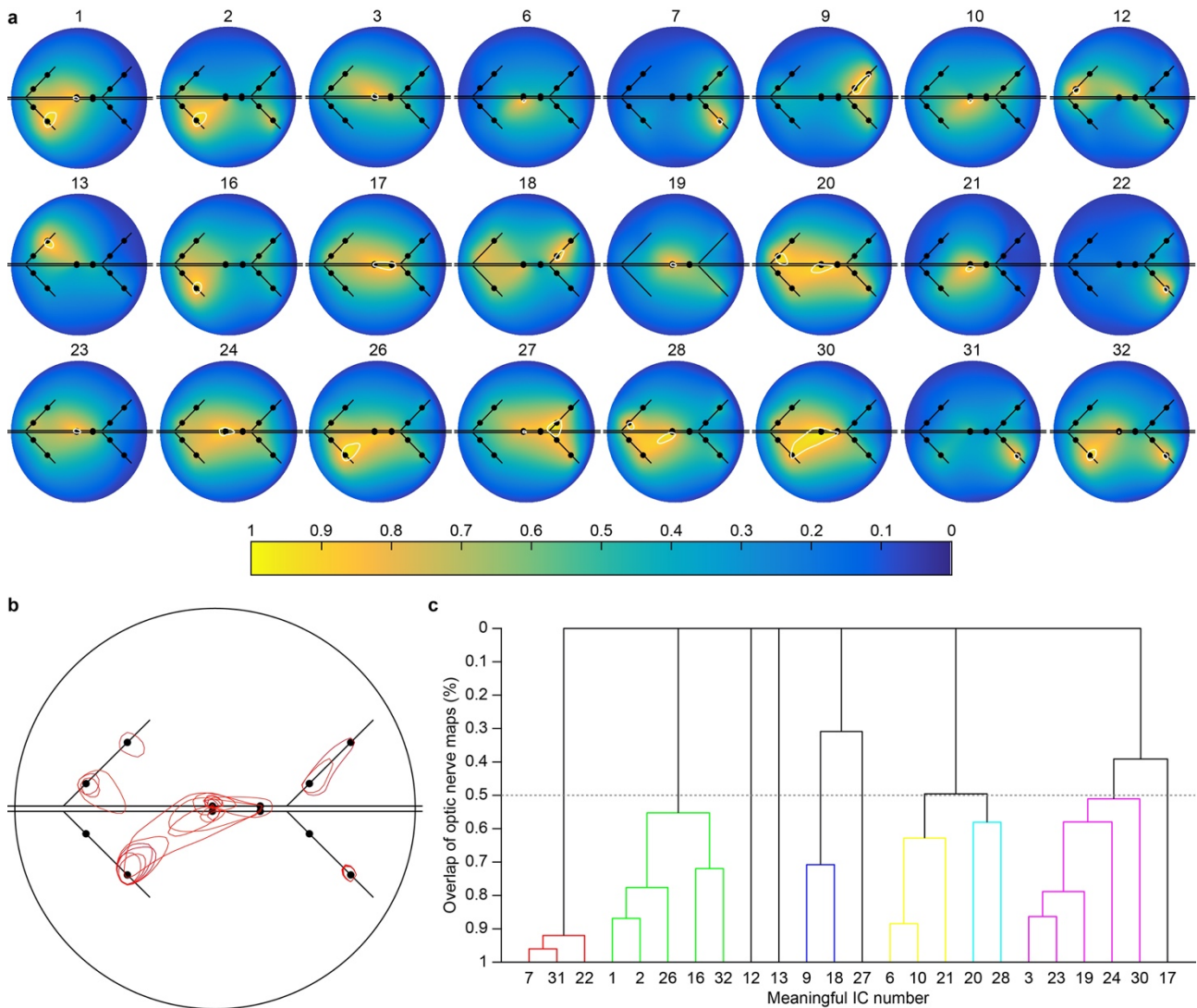


Figure 2-6 | Distribution map of the independent components within the optic nerve. (a) Individual distribution maps of each meaningful IC within the optic nerve. The colour code is the normalized IC peak-to-peak amplitude. The white contour corresponds to 90% of the maximal value of the distribution map. Most of the meaningful ICs are segregated in a small portion of the optic nerve, localized around one or in some cases a few neighbouring electrodes. **(b)** Overlay of the 90% activation contours (red) of all the meaningful ICs. The black circle represents the optic nerve. The sketch of the OpticSELINE is in black in both a and b. **(c)** Dendrogram of the hierarchical clustering of the meaningful ICs, based on the average overlap between the 90% area of each of their distribution maps at the level of the optic nerve. The threshold to determine the meaningful ICs that are part of the same cluster was set to a minimum overlap of 50% (dashed line). Representative example from N = 1 rabbit with a current amplitude of 750 μ A. Experiment repeated on N = 4 rabbits.

In addition, each meaningful IC exhibited a different degree of activation as a function of the stimulating electrode used. To quantify this, for each meaningful IC, the peak-to-peak amplitude of the early portion of the time courses (from 5 to 25ms after the pulse) induced by each stimulating electrode was computed and normalized among all the stimulating electrodes. All nine functional stimulating electrodes had at least one meaningful IC whose activation was maximized when stimulating through this electrode. Furthermore, by interpolating the contribution of every stimulating electrode to each IC, we found their distribution map within the optic nerve. The area corresponding to 90% of the activation level was confined to a small area around this electrode or, in some cases, it spread over one or two neighbouring electrodes (white lines in Figure 2-6a and red lines in Figure 2-6b). As expected, the three electrodes associated only with flat responses had no meaningful ICs associated with them. A further classification of meaningful ICs based on the distribution map within the optic nerve revealed that the 24 meaningful ICs could be grouped into 10 meaningful

clusters (Figure 2-6c). We verified that the number of meaningful clusters did not significantly change when considering less restrictive activation levels. With both 80% and 70% activation levels, the number of meaningful clusters was 9. In addition, in this representative example, the number of meaningful clusters remained qualitatively constant regardless of the current amplitude (Figure 2-5d, red trace and symbols).

We obtained a similar result in all the rabbits (N=4) recorded by stimulating with only six electrodes of the OpticSELINE (from 1 to 6, top side). On average, with the increase of the current amplitude, the number of flat ICs decreases, the number of common ICs increased, and the number of meaningful ICs first increased and then stabilized (Supplementary Figure 2-917). The mean (\pm s.d.) number of meaningful clusters remained qualitatively constant regardless of the current amplitude. The spatial organization of the ICs in the visual cortex and the back-projection of the ICs in correspondence with the OpticSELINE electrodes are considered as indirect signatures of the stimulation selectivity of the OpticSELINE.

2.3.5 Selectivity of optic-nerve stimulation

Measuring the recruitment and activity of optic-nerve fibres during *in vivo* stimulation is a challenging task. In addition, relying on cortical EEPs to determine the threshold and level of optic-nerve activation is critical, since cortical recordings might be affected by the variability in the impedance of the recording electrodes, both intra and inter-subject. Therefore, to better evaluate the current threshold and the number of fibres activated by each electric pulse at increasing current amplitudes, we implemented a hybrid numerical model and simulation based on two steps^{296,297}. First, the potential field generated by the electrical stimulation was computed using finite element analysis (FEA). Then, the activation probability of the fibres located around the stimulating electrode was obtained using the NEURON simulation environment. For the anatomical model, we considered the fibre distribution according to our findings (Supplementary Figure 2-311), and the nerve diameter was set to 1.5mm. The hybrid FEA model and NEURON simulation showed that on cathodic stimulation with pulses of 150 μ s, the activation of nerve fibres started from current amplitudes as low as 2 μ A and increased with increasing current amplitudes (Figure 2-7a and b). The number of nerve fibres activated was estimated considering a fibre density of 0.19 fibres μm^{-2} , as previously identified (Figure 2-7b). These results show that OpticSELINE can activate both internal and external fibres, in contrast to self-sizing spiral cuff epineural electrodes that preferentially activate the latter²⁹⁶. Finally, we investigated the electrode selectivity by computing the overlap of the activated fibres as a function of the stimulating current from two neighbouring electrodes (Figure 2-7c and d). The two activated areas remained separated up to a current amplitude of 10 μ A, whereas for higher currents, they started to fuse together, reaching a value of 31.2 % for 50 μ A.

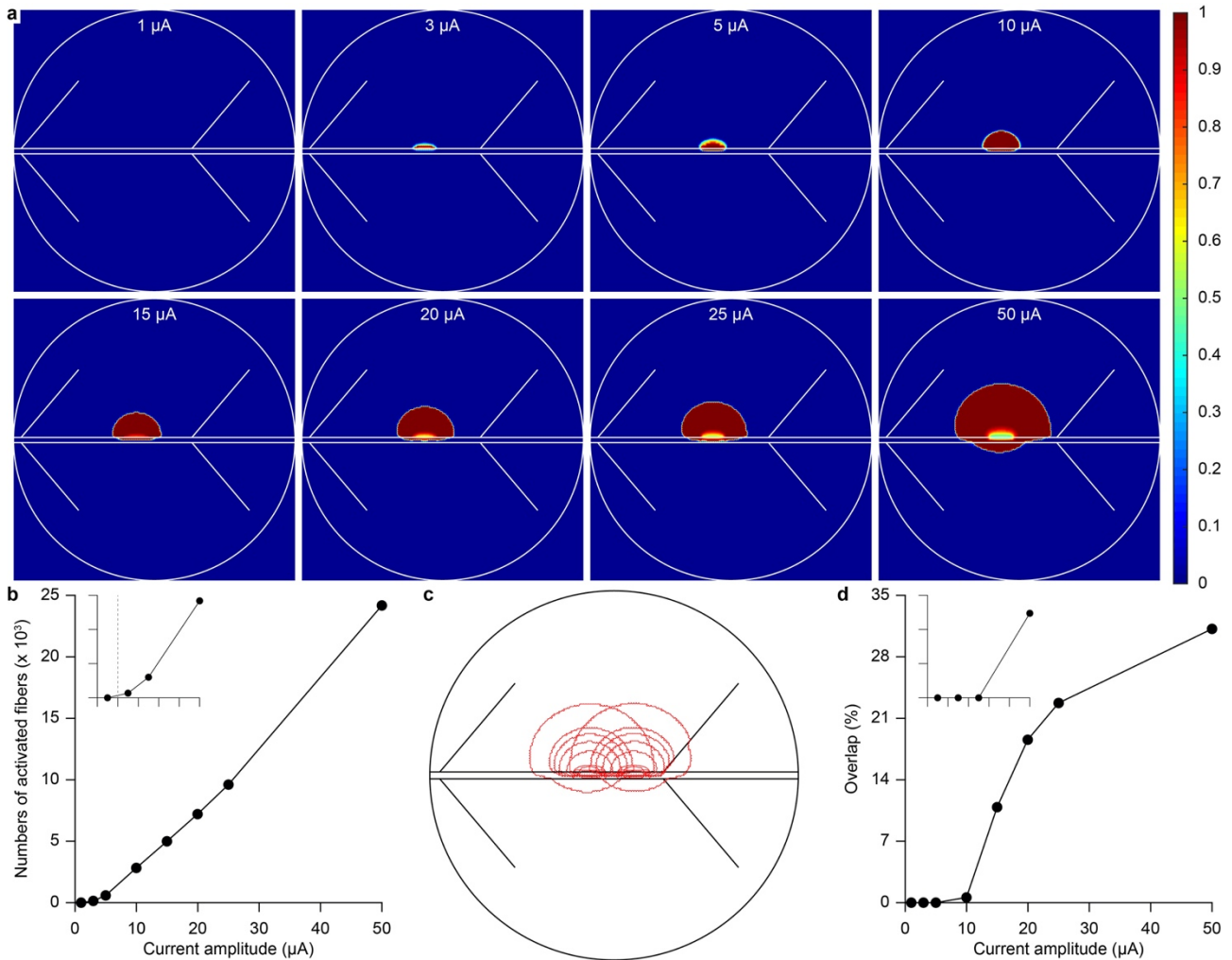


Figure 2-7 | Probability activation map of the optic nerve. (a) Probability activation map upon current pulses (150 μ s, cathodic phase first) at increasing current amplitudes from electrode 3 of the OpticSELINE. The colour code is the probability of activation in percentage. (b) Number of fibres activated by a single current pulse as a function of the current amplitude. The inset graph shows a magnification from 0 to 10 μ A (x axis) and from 0 to 3,000 fibres (y axis); the dashed line is 2 μ A. (c) Overlay of the activated area with a probability higher than 90% at increasing current amplitudes for electrodes 3 and 4. (d) Per cent overlap of the activated areas from electrodes 3 and 4 as a function of the current amplitude. The inset graph shows a magnification from 0 to 10 μ A (x axis) and from 0 to 0.75% (y axis).

There is a narrow range over which currents can be varied (up to approximately 10 μ A) without affecting the spatial selectivity in fibre recruitment; overall, this limits the dynamic range of intraneural stimulation. However, by using a self-sizing spiral cuff epineural electrode, it has been shown that high-frequency stimulation can be exploited to reduce the perception threshold instead of pulse modulation (amplitude or duration)²⁹⁶. First, we verified that this mechanism can also be recruited with intraneural stimulation via OpticSELINE. We delivered pulse trains (consisting of one, two, three or four pulses) at the highest repetition rate (1 kHz) allowed by our stimulation protocol (Figure 2-8a). In this manner, our results can be generalized to every lower repetition rate; for example, as previously shown up to 300Hz²⁹⁶. We also verified that nerve fatigue due to repetitive stimulation with a pulse train is not present (Supplementary Figure 2-210b–d). By increasing the number of pulses within the train (from 1 to 4) with equal current amplitude, the mean (\pm s.e.m., N=4 rabbits) N1 threshold was reduced to 35.83 \pm 6.59% (for four pulses) of the threshold obtained with a single pulse (Figure 2-8b). Similarly, cortical activation (for example, P1 PA) can be modulated in amplitude by increasing the number of pulses instead of changing the current intensity (Figure 2-8c). Notably, by using the hybrid FEA model and NEURON simulation, we estimated that the activated area from each electrode was

not affected (maximal variation of 4.3% for a current pulse of 15 μ A) by increasing the number of pulses in the train while keeping the amplitude constant (Figure 2-8e); this is particularly evident for current amplitudes below 10 μ A. In a previous study, this phenomenon was reported as a mechanism of temporal summation (Figure 2-8d) resulting from the repeated activation of the same few axons and not leading to the recruitment of more fibres. This strategy based on frequency modulation can be applied to widen the input dynamic range of the OpticSELINE. In addition, techniques such as current steering and focusing might be used to further enhance the stimulation selectivity²⁹⁷.

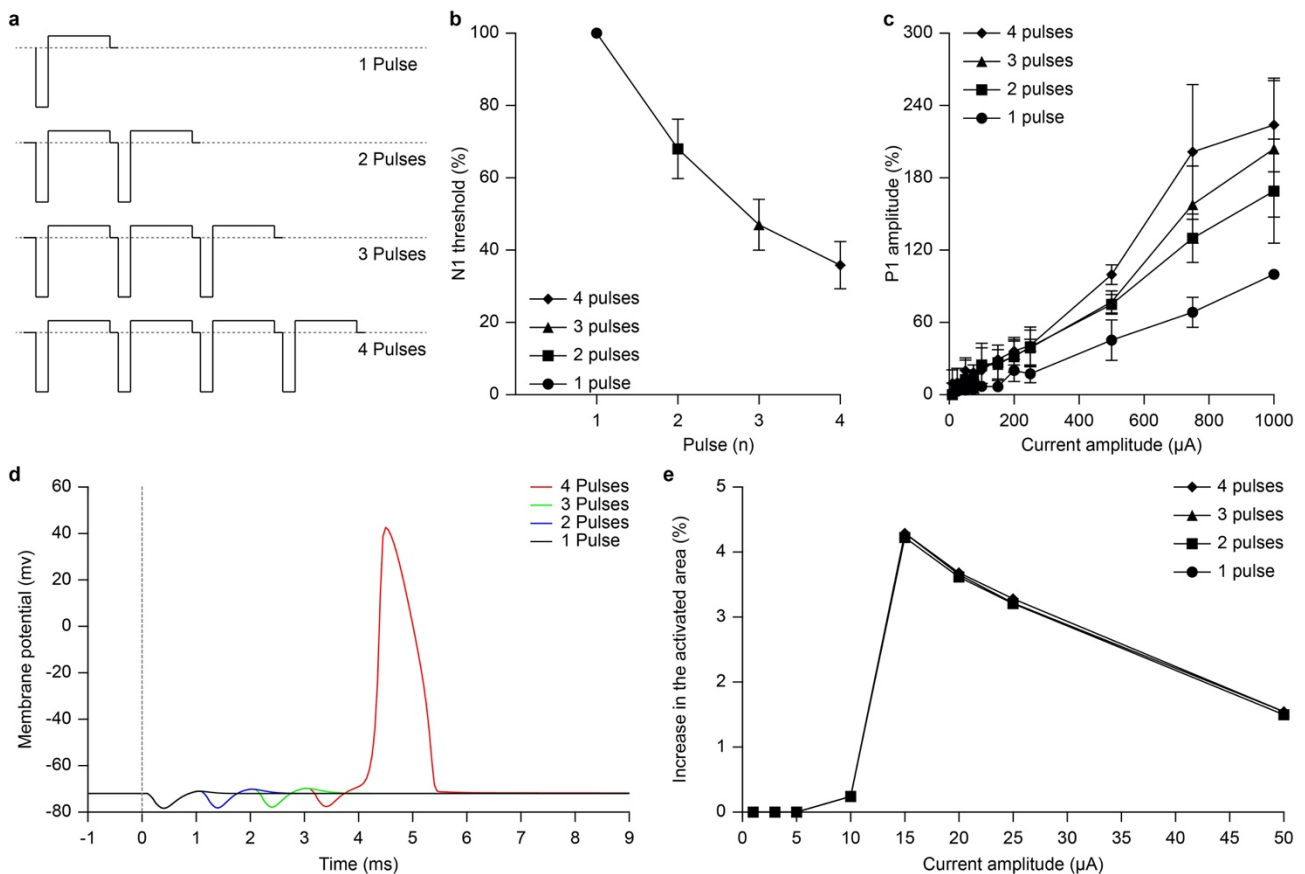


Figure 2-8 | High-frequency stimulation of the optic nerve. (a) EEPs have been evoked via the implanted OpticSELINE (6 electrodes, top side) with biphasic current pulses arranged in packages containing 1, 2, 3 or 4 pulses at 1 kHz of repetition rate. (b) Normalized mean (\pm s.e.m., $N = 4$ rabbits) of the N1 current threshold with stimuli composed of 1 to 4 pulses (circles, squares, triangles and diamonds, respectively). The N1 current threshold was quantified based on the N1 leading channel. For each rabbit, 10 consecutive recordings were averaged. The normalization was performed compared to the threshold on one pulse. (c) Normalized means (\pm s.e.m., $N = 4$) of P1 PAs for trains with 1, 2, 3 or 4 pulses (circles, squares, triangles and diamonds, respectively). The normalization was performed compared to the amplitude on one pulse at 1,000 μ A. For each rabbit, 10 consecutive recordings were averaged. PAs were quantified for each stimulating electrode of the OpticSELINE from the averaged response of the 32 recording electrodes and the resulting values were averaged among stimulating electrodes. (d) Membrane potential of a simulated optic-nerve fibre upon stimulation with a train composed of 1, 2, 3 or 4 pulses. The current pulse is set to 25 μ A. (e) Change in the activated area as a function of the current amplitudes for trains with 1, 2, 3 or 4 pulses.

2.4 Discussion

Currently, research on visual prostheses is mostly focused on the development of retinal prostheses, either subretinal, epiretinal or suprachoroidal^{20,21,23,24,50–53}. Nevertheless, in addition to the early pioneering works, some research groups are attempting the stimulation of other regions of the visual pathway¹². Optic-nerve prostheses aim to stimulate the axonal fibres from retinal ganglion cells along their path towards

the optic chiasm. Optic-nerve stimulation was first reported in a set of studies on two blind patients affected by retinitis pigmentosa^{225,227} and then in another study targeting the optic disc⁵⁰.

In the first set of studies, the two patients were implanted with self-sizing spiral cuff epineural electrodes, which have the advantage of being less invasive than intraneural arrays. However, one of the main limitations of the self-sizing spiral cuff epineural electrode is the induction of phosphenes that are widely distributed in the visual field of the patient, probably because they mostly activate external fibres with limited selectivity²⁹⁶. Nevertheless, intraneural arrays can also stimulate the central area of the nerve and provide higher stimulation selectivity²³⁰. In addition, intraneural arrays such as the OpticSELINE are mechanically very stable²³²; therefore, they could enable more reproducible and stable stimulation. For these reasons, we selected an intraneural approach, confirming the high mechanical stability provided by the lateral flaps and the high selectivity in fibre recruitment, as demonstrated by the hybrid FEA model and NEURON simulation.

In our experimental design, we chose to target the intracranial segment of the optic nerve. Spiral cuff epineural electrodes were previously implanted in both the intraorbital²²⁷ and intracranial²²⁵ segment of the nerve. The comparison of the two clinical studies showed that intraorbital stimulation induces smaller EEPs compared with intracranial stimulation, whereas latencies are not significantly different; in other words, the perceptual threshold is higher for intraorbital stimulation²⁷⁶. In addition, the intraorbital segment of the optic nerve must accommodate eye movements; therefore, an intraneural electrode may be subjected to high cyclic strain, which could lead to subsequent failure. This issue is minimized in the intracranial segment. A third drawback of the intraorbital placement of an intraneural electrode is due to the presence of the central retinal vein and artery entering the nerve at approximately 1 cm from the eyeball; an intraneural placement may risk damaging them. Therefore, for intraneural electrodes, the intracranial placement seems more appropriate than intraorbital placement.

In a previous study with the self-sizing spiral cuff epineural electrode²⁹⁶, the perception threshold of the patient was investigated as a function of the stimulation intensity (pulse duration or amplitude) and the stimulation frequency (number of pulses and repetition rate). A reduction of the perception threshold was observed by increasing both parameters: a mechanism of spatial summation (each single pulse recruits more fibres) was associated with the intensity modulation, while a mechanism of temporal summation (repeated activation of the same axons not resulting in the recruitment of more fibres) was associated with the frequency modulation. Although the first mechanism was expected, the second one was more difficult to assess. We showed that intraneural optic-nerve stimulation can be implemented even at a very high frequency (that is, 1 kHz), three times higher than has been previously reported²⁹⁶. As expected, a reduction of the N1 activation threshold was observed with multiple pulses, without inducing nerve fatigue upon repetitive stimulation. In addition, using a hybrid FEA model and NEURON simulation approach, we verified that the temporal summation does not induce the recruitment of more nerve fibres.

Optic-nerve stimulation differs from retinal prostheses since it selectively activates only axonal fibres instead of cell bodies and other synaptically connected cells in the retinal network; thus, the generated signal is not dependent on the complex and uncontrolled synaptic processing within the retina²²⁶. Subretinal prostheses activate retinal ganglion cells preferentially through the inner nuclear layer. Epiretinal prostheses activate retinal ganglion cells both directly and indirectly via the inner nuclear layer. Short electric pulses preferentially activate retinal ganglion cells directly, even if the thresholds for direct and indirect activation are barely discriminable for clinically used pulses (for example, 450 μ s in Argus II)^{302,303}. For this reason, optic-nerve stimulation appears to be a good strategy for neuromorphic prostheses or for the testing of neuromorphic

algorithms in animal models, in which the reproduction of the natural code of retinal ganglion cells is needed with high temporal fidelity^{304,305}. Conversely, the downside of optic-nerve stimulation is the inability to activate the inner retinal circuit, which might provide a more natural form of vision.

An important feature of OpticSELINE is the capability to induce selective optic-nerve stimulation and generate spatially organized cortical patterns. The first clinical trial with epineural electrodes already demonstrated that optic-nerve stimulation induces spatially organized phosphenes²²⁶. The C-Sight project demonstrated that in rabbits the position of the cortical channel with the highest amplitude can be spatially modulated by applying current-steering methods to the intraneural stimulation of the intraorbital segment of the optic nerve²⁸⁴. We have found that with an intraneural array, it is possible to associate ‘meaningful’ cortical activation patterns obtained by ICA with specific stimulating electrodes, suggesting that the OpticSELINE induces activation of the visual cortex in a reproducible and spatially organized manner. This is possible because of the selective activation of nerve fibres, which could open the possibility to elicit behaviourally relevant visual activation patterns by optimizing the stimulation protocol.

2.4.1 Outlook

This work contributes to progress towards the implementation of optic-nerve stimulation to restore functional vision. However, our results, obtained in an animal model, cannot be easily translated to restore vision in a blind patient. ECoG recordings measure an integrated activation of the cortical surface, therefore intrinsically lack the required spatial selectivity to prove that different electrodes of the OpticSELINE activate different regions of the visual cortex. To overcome this problem, we implemented a blind source separation approach, which has already been exploited to overcome the intrinsic limitation of the recording method²⁹²; for example, to determine different sources of activity in the electroencephalographic signal. Further work is still required to find a direct link between ICs and physiological steady measures such as dipolarity. In addition, further evidence might be obtained with techniques that enable higher specificity in cortical recordings in large animals, such as fast three-dimensional functional imaging tools^{306–308}.

2.5 Methods

2.5.1 Electrode microfabrication

OpticSELINE was developed using microphotolithography and thin-film techniques. A silicon wafer was used as a sacrificial layer. After the cleaning of a silicon wafer (10 min acetone; deionized water rinse; 10 min isopropanol), two layers of polyimide PI2610 (HD Microsystems) were spun on the substrate (2,000 r.p.m. for 30 s). Samples were hard baked in an oven with nitrogen flux at 350 °C for 1 h. Lift-off layer and S1813 (Microposit) were spincoated on the wafer at 1,000 r.p.m. for 20 s and 4,500 r.p.m. for 30 s. The substrate was exposed using a glass photomask at a dose of 180 mJ cm⁻². The sample was developed in MF319 for 30 s and rinsed in deionized water. A layer of titanium (20 nm) and gold (250 nm) was sputtered on the substrate and a lift-off technique was used to release the pattern of traces, active sites and pads (overnight immersion in remover 1165). Two layers of PI2610 were spun on the substrate (2,000 r.p.m. for 30 s) and hard baked in the oven with nitrogen flux at 350 °C for 1 h. An aluminium mask (200 nm) was deposited on the substrate by thermal evaporation. S1813 was spun on the sample and exposed (glass photomask, 180 mJ cm⁻²) and the wafer was developed in MF319 for 30 s. S1813 was removed (2 min in remover 1165) and dry etching was used to etch the excess of polyimide (40 sccm of O₂ (sccm, standard cm³ per min);

150 W, 1 h). The aluminium mask was etched away and electrodes were peeled off from the wafer. The three-dimensional geometry was conferred to the OpticSELINE by securing the device on a stainless-steel mould. The mould has four holes in correspondence with the four flaps; a needle was used to secure each flap inside the hole. Alignment holes were included on the mould to ease the placement of the device. A thermal treatment (1 h, 200 °C) was used to memorize the curved shape of the flaps. The devices were connected to the polyimide-based extension cable: a silver conductive glue was used to connect the corresponding pads of the two elements (Ablestik-Henkel; 1 h at 130 °C). Then, the flexible extension cable was connected to a printed circuit board by silver conductive glue. A surgical needle with a looped wire (Ethicon) was inserted through the device. Flexible wires were soldered to the printed circuit board and a linear Omnetics connector was attached. Two-component biocompatible silicone (Silbione-Bluestar Silicones) was applied to all the soldering.

2.5.2 Electrochemical characterization

Cyclic voltammetry was performed using a three-electrode setup immersed in phosphate-buffered saline (PBS) solution and applying a ten-cycle potential ramp at a scan rate of 1.5 V s⁻¹ between -0.5 V and +0.5 V. Impedance measurements were performed using a three-electrode setup immersed in PBS solution and applying a sinusoid of 10 mV between 100 Hz and 100 kHz. The accelerated ageing test was performed for 6 d at a temperature of 87 °C with an accelerating factor of 32. OpticSELINE arrays were in glass beakers filled with PBS and the beakers were sealed and stored in an oven.

2.5.3 Mechanical tests

Both experiments were performed using the same setup, comprising a press to secure the nerve, a 10 N load cell and an explanted rabbit optic nerve. During insertion experiments, the nerve was first pierced by the needle and then the electrode was pulled at a constant speed of 15 mm min⁻¹ to insert the device inside the nerve. During extraction experiments, the device was first implanted inside the nerve, and then the electrode was pulled at a constant speed of 15 mm min⁻¹ to completely extract the device from the nerve. In both cases, insertion and extraction forces were measured by a load cell.

2.5.4 Animal handling and surgery

Animal experiments were performed under the authorization GE1416 approved by the Département de l'Emploi, des Affaires Sociales et de la Santé, Direction Générale de la Santé of the République et Canton de Genève (Switzerland). Female New Zealand white rabbits (>16 weeks, >2.5 kg) were sedated with an intramuscular injection of xylazine (5 mg kg⁻¹). Anaesthesia and analgesia were provided with an intramuscular injection of an anaesthetic mix composed of medetomidine (0.5 mg kg⁻¹), ketamine (25 mg kg⁻¹) and buprenorphine (0.03 mg kg⁻¹). If required, anaesthesia was prolonged with further injections (half dose) of the anaesthetic mix. Eye drops were placed on the eye to prevent eye drying. The rabbit was placed on a heating pad at 35 °C for the entire procedure. Oxygen was provided with a mask to prevent hypoxia during the anaesthesia. The head was shaved and cleaned with 70% ethanol and betadine. The rabbit's head was then secured gently within a stereotactic frame (David Kopf Instruments). Before cortical skin incision, a mix of lidocaine (6 mg kg⁻¹), bupivacaine (2.5 mg kg⁻¹) and adrenaline (0.1 mg kg⁻¹) was injected subcutaneously at the surgical sites. After 5 min, the skin was opened and pulled aside to expose the skull and the skull was cleaned with cotton swabs. A temporal craniotomy was made to access the left optic nerve. The OpticSELINE was inserted in the left optic nerve from lateral to medial in the pre-chiasmatic area. The surgical

implantation was performed by piercing the nerve with a needle (prolene 10-0 EH7900G, Ethicon) and by guiding the OpticSELINE transversally into the nerve with the suture until the electrode enlargement (used as a stopper). At this stage, the four alignment bars were visible on the other side of the nerve; the OpticSELINE was then slightly pulled back until only three alignment bars were visible to anchor it into the nerve. Then, a second craniotomy was made to expose the right visual cortex. A 32-channel epidural ECoG array (E32-1000-30-200; NeuroNexus) was placed on the visual cortex. All rabbits were euthanized at the end of the acute recording procedures while still under anaesthesia, with an intravenous injection of pentobarbital (120 mg kg⁻¹).

2.5.5 Optic-nerve anatomy

To determine the average nerve diameter, optic nerves ($n = 10$) were explanted from five female New Zealand white rabbits (>16 weeks, >2.5 kg), immediately embedded in the optimum cutting temperature compound (Tissue-Tek, Qiagen) and frozen at -20°C . $10\ \mu\text{m}$ sections were obtained with a cryostat (Leica Microsystems) and mounted on glass slides. Images were taken with a slide scanner (VS120-L100, Olympus). For each nerve, three sections were collected and an average diameter was computed.

To determine the distribution of the fibre diameters, one female New Zealand white rabbit was perfused under anaesthesia with a mix of 2.5% glutaraldehyde and 2.0% paraformaldehyde in 0.1 M phosphate buffer (pH 7.4). The descending aorta was clamped to deliver the solution exclusively to the brain. After perfusion, the brain was left to rest for 2 h and then dissected. Both optic nerves, including the chiasma, were dissected from the skull and placed in the same fixation solution overnight at 4°C . The tissue was then sliced transversally using a vibratome (VT1200, Leica) at a thickness of $100\ \mu\text{m}$. Slices at different positions were then washed with cacodylate buffer (0.1 M, pH 7.4), post-fixed for 40 min in 1.0% osmium tetroxide with 1.5% potassium ferrocyanide, and then for 40 min in 1.0% osmium tetroxide alone. They were finally stained for 30 min in 1% uranyl acetate in water before being dehydrated through increasing concentrations of ethanol and finally embedded in resin (Durcupan ACM, Fluka). The resin was hardened for 24 h in an oven at 65°C . The different regions were sectioned with a diamond knife at a thickness of $0.5\ \mu\text{m}$, collected onto a glass microscope slide and stained with toluidine blue. The entire tissue section was imaged at a resolution of 92.3 nm per pixel with a transmitted-light microscope (Olympus Slide Scanner VS120-L100). The axon segmentation was performed using a customized MATLAB (MathWorks, v.R2018a) script. An image of a central section of the optic nerve was divided into 64 (8×8) squares, for each of which the areas of all the objects identified as axons were collected. The internal diameter of each axon was calculated assuming circularity. A histogram of the axon diameter distribution for each quadrant was created by dividing the whole range of diameters (0–3,000 nm) into bins of 50 nm width and by computing the total axon count for each bin. To normalize the height of the bars, the relative probability for each bin was computed by dividing the count of the bin by the total number of axons in the square. The median diameter of each square was used for the statistical analysis. The squares that did not contain any axons were excluded from the analysis. The axon density for each square was obtained by dividing the total number of axons by the area occupied by the axons in that square.

2.5.6 Electrophysiology

For optic-nerve stimulation, the OpticSELINE was attached to a current stimulator (IZ2MH; Tucker-Davis Technologies), whereas for cortical recordings, the ECoG array (E32-1000-30-200; NeuroNexus) was connected to an amplifier (PZ5; Tucker-Davis Technologies) via a 32-channel analogue head stage (ZIF-Clip Analog Headstage; Tucker-Davis Technologies). Optic-nerve stimulation was performed with 13 pulse

amplitudes (10, 25, 50, 75, 100, 150, 200, 250, 500, 750, 1,000, 1,500 and 2,000 μ A) and 5 pulse durations (50, 100, 150, 200 and 400 μ s) delivered in a scrambled manner. Data were filtered between 0.5 Hz and 2 kHz and digitized at 12 kHz. Epochs (from -100 to 750 ms) synchronous to the onset of the stimulation were then extracted from the data stream and data analysis was performed with MATLAB.

2.5.7 Blind source separation

For each recording electrode and each stimulation intensity, epochs were concatenated and processed with an AMICA57 core and GPU-processed infomax reliable ICA (RELICA)³⁰⁹. Dimensionality reduction on the data as a pre-processing step to ICA was not performed¹. RELICA allowed us to test the repeatability of ICs appearing in decompositions of bootstrapped versions of the input data and to retain only stable ICs for further analysis. Given the multivariate dataset from the 32 recording electrodes X (electrode, time), ICA extracts an unmixing matrix W (32×32) such that the IC time courses $S = WX$ are maximally independent. Rows of W represent the weights applied to each electrode to obtain the corresponding ICs S . The i th column of the mixing matrix A (pseudoinverse of W) represents the weight of the i th IC on each recording electrode and can be represented as an activation map. Each activation map was obtained by projecting the weights of the unmixing matrix A onto the layout of the ECoG array, then by spatially interpolating them with a spline function, and finally by normalizing the maps to the maximal absolute value present in the interpolated map. IC grand-average time courses, obtained by performing the average over trials for each stimulation intensity, formed the IC-EEPs. The PVAF by each IC on each electrode was computed and represented as a PVAF activation map. ICs were categorized into several classes: flat, common, artefact, noise and meaningful (Supplementary Figure 2-614a). First, low-frequency components of the signal were removed using a zero-phase high-pass filter with a 5 Hz cut-off frequency. Then, artefact ICs, exhibiting a large activation within the first 5 ms from the stimulus onset, were identified by visual inspection and removed. To verify that the artefact ICs were correctly identified, all the other ICs were back-projected. The initial portion of the back-projected signal (0 to 5 ms) was indeed exclusively affected by the manual removal of the artefact ICs when compared to the original signal (Supplementary Figure 2-1018). Following the identification of the artefact, the noise ICs were identified by computing the frequency plot of the signal; the ICs exhibiting unusual peaks in the 250 to 500 Hz frequency range were labelled noise (Supplementary Figure 2-614b). Among the remaining ICs (Supplementary Figure 2-614c), the ones with a peak-to-peak variation (Δ) in the time course (time frame from 5 to 25 ms after the stimulus) smaller than three times the standard deviation of the time course (σ) were labelled as flat ($\Delta/\sigma < 3$). To separate meaningful ICs from common ICs, a similarity index was used: that is, the correlation between the time courses of the different stimulating electrodes. ICs were classified as common (that is, with visible meaningful activation but with similar time courses for all the stimulating electrodes) when exhibiting a mean similarity index larger than 0.5. The distribution maps in the optic nerve were obtained by interpolating the contribution of every stimulating electrode to each IC with a spline function. The contour of the optic nerve was set to zero. Meaningful ICs were further classified into meaningful clusters by grouping together the ICs that were associated with similar portions of the optic nerve. We defined a similarity index consisting of the average area overlap between the 90% area of the distribution maps at the level of the optic nerve of each pair of meaningful ICs. A perfect overlap between the 90% area is a score of one and no overlap is a score of zero. On the basis of this similarity, we used the complete-linkage clustering method to build a clustering tree of the meaningful ICs. ICs that had at least 50% overlap were clustered.

2.5.8 Hybrid FEA model and NEURON simulation

A realistic electrical and structural model was built by combining a three-dimensional FEA model in COMSOL Multiphysics (v.5.2.262) to determine the electrical potential distribution inside the optic nerve with a biophysical-cable model of the optic-nerve axons simulated in the NEURON environment (v.7.4). The FEA model was built using COMSOL's stationary-current study with the AC/DC module. The optic-nerve model consists of a central cylinder surrounded by the meningeal layers, modelled as concentric cylinders. In particular, the pia mater was approximated by a contact impedance due to its very small thickness, and the cerebrospinal fluid was placed between the pia mater and the dura mater. The optic nerve is surrounded by a volume of saline solution. The OpticSELINE is inserted transversely through the centre of the optic nerve domain so that each of the four central electrodes, modelled as boundary current sources of 0.008 mm², is equidistant from the centre of the optic-nerve domain. Finally, a large return electrode is modelled in saline medium. Except for the optic-nerve domain, which has a larger electrical conductivity along its axis, all the other domains have isotropic conductivity. The size (in μm) and conductivity (in S m^{-1}) of the different domains are as follows. For the optic nerve, the radius is 750, the longitudinal electrical conductivity is 0.5 and the transversal electrical conductivity is 0.08³¹⁰. For the pia mater, the thickness is 10 and the electrical conductivity is 0.016³¹⁰. For the dura mater, the thickness is 300 and the electrical conductivity is 0.06³¹¹. For the cerebrospinal fluid, the thickness is 100 and the electrical conductivity is 1.7³¹². For the saline, the electrical conductivity is 1.7³¹².

A monophasic unitary current pulse was injected through one of the electrodes while the current in the others was set to zero. Quasi-static approximation of Maxwell equations is valid at the frequency range of the experiment³¹³. Therefore, the extracellular electrical potential V_e resulting from the injection of the current can be computed with the Laplace formulation: equation (1)³¹⁴:

$$\nabla \cdot \sigma \nabla V_e = 0 \quad (1)$$

Resulting in equation (2), with the Dirichlet boundary conditions set to zero at the external part of the box:

$$V_e(\Omega\delta) = 0 \quad (2)$$

where $\delta\Omega$ represents the basis of the cylinders and the outer surface of the saline box. The size of the saline box and the mesh size were optimized to respect the hypothesis of ground condition at infinity. We tested models with different combinations of length and radius of the saline box, all of which had a mesh composed of tetradic second-order elements. To achieve better accuracy, the mesh close to the electrode, where the steeper change in the electrical potential occurs, was made finer by making two concentric spheres of smaller mesh size around the electrode. According to frequently used indexes in FEA³¹⁵, we optimized the size of the saline box as 4.5 mm in diameter and a total length of 5 mm.

The axon-fibre models were implemented in NEURON as McNeal's cable model; only the nodes of Ranvier are active segments, while the myelinated segments are approximated by a perfect insulator. The geometric parameters used to build each axon model were obtained from a previous work²⁹⁸. Each axon model is a modified Hodgkin–Huxley model¹⁹², with each of its nodes of Ranvier containing five types of currents: fast sodium current, fast potassium current, persistent sodium current, slow potassium current and leak current. The electrical properties of the axon were obtained from a previous work³¹⁶. The axon models allow determination of whether a set of extracellular-potential values (obtained from the interpolation of the potential distribution from the FEA model at the locations of their nodes of Ranvier) can generate an action potential.

An axon is defined as activated if an action potential travels to both of its ends. For an axon of a given diameter and shift (the relative distance separating its central node of Ranvier from the centre of the stimulating electrode), its probability of being activated by the stimulation is binary: either 0 or 1. To determine the probability of a certain pair of coordinates in the optic-nerve cross-section containing an axon activated by a given electrical stimulation, the probabilities of all possible axons passing were computed. We tested a total of 60 combinations of diameters and shifts: 12 diameters ranging from 0.25 to 3 μm and 6 shifts (ranging from 0 if the electrode is aligned with the central node of Ranvier to 0.5 if the electrode aligned with the centre of the myelinated segment, with an interval of 0.1). Each of these 60 probabilities was weighted by a factor that consists of the frequency of occurrence of the diameter it corresponds to, multiplied by the squared diameter of the axons. Once weighted, these probabilities were summed to give the final combined probability of activation. We sampled the probability of activation at every $40\ \mu\text{m} \times 40\ \mu\text{m}$ pair of coordinates over the entire cross-section of the optic nerve and re-sampled it more finely at the locations where an important change in the probability of activation was present. These probabilities of activation were linearly interpolated to give the final probability maps with a resolution of $1\ \mu\text{m}$.

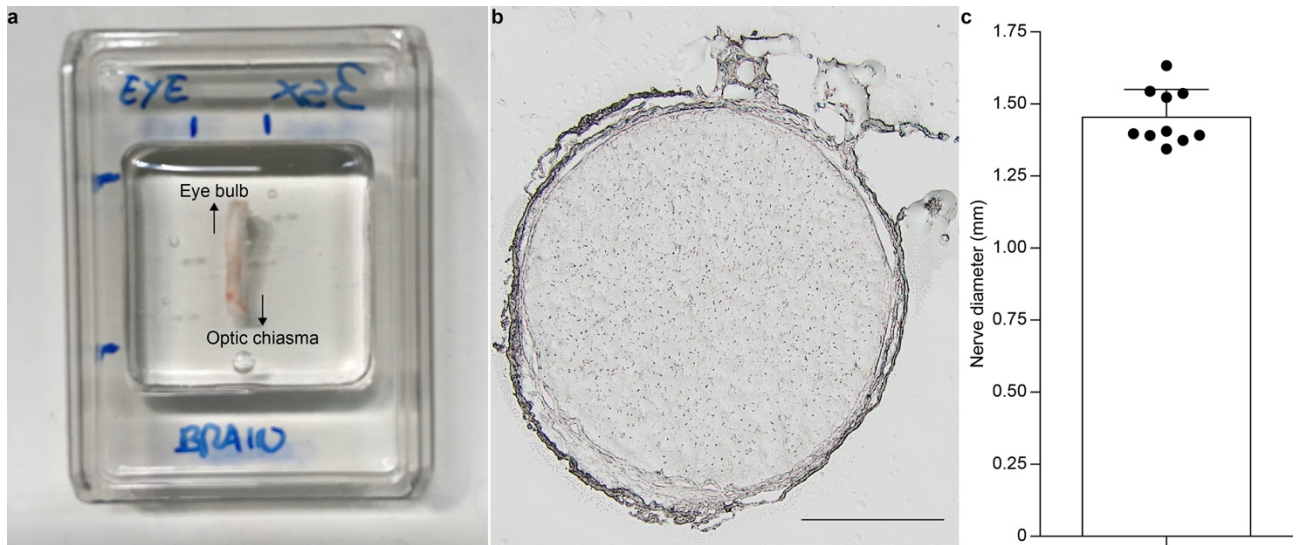
2.5.9 Statistical analysis and graphical representation

Statistical analysis and graphical representation were performed with Prism (GraphPad Software, v.8.1.2). The normality test (D'Agostino and Pearson omnibus-normality test) was performed in each dataset to justify the use of a parametric or non-parametric test. In each figure, P-values are represented as *P < 0.05, **P < 0.01, ***P < 0.001 and ****P < 0.0001. Data are reported as the mean \pm s.e.m. or mean \pm s.d.; n is used to identify the number of electrodes, trials or nerves; N is used to identify the number of rabbits.

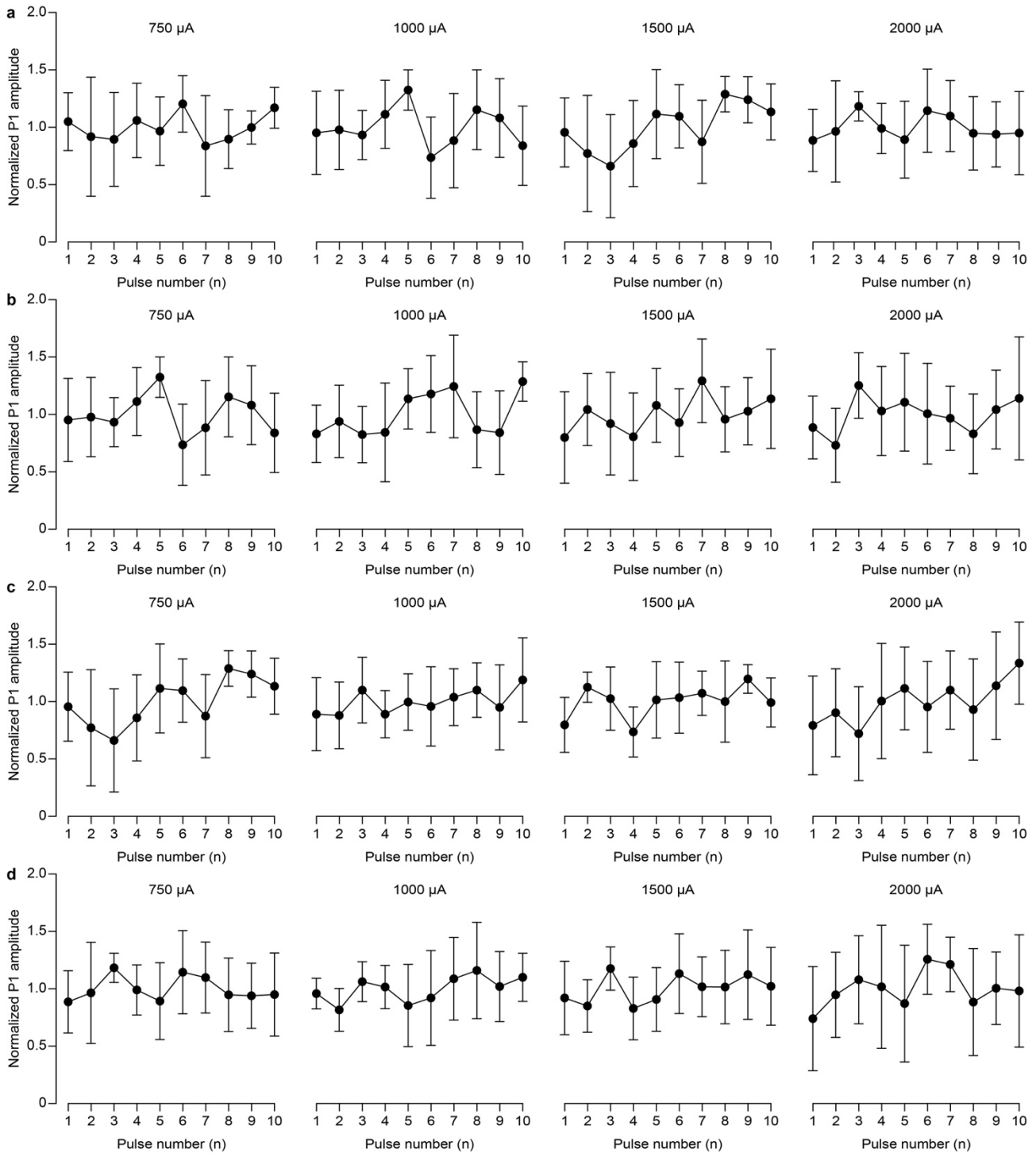
2.6 Acknowledgment

We acknowledge the support from the Bioelectron Microscopy Core Facility (BIOEM) of École polytechnique fédérale de Lausanne. This work has been supported by École polytechnique fédérale de Lausanne, Medtronic, Bertarelli Foundation and Wyss Center for Bio and Neuroengineering. F.A. is supported by the European Union's Horizon 2020 research and innovation programme under Marie Skłodowska-Curie Action agreement no. 750947 (BIREHAB).

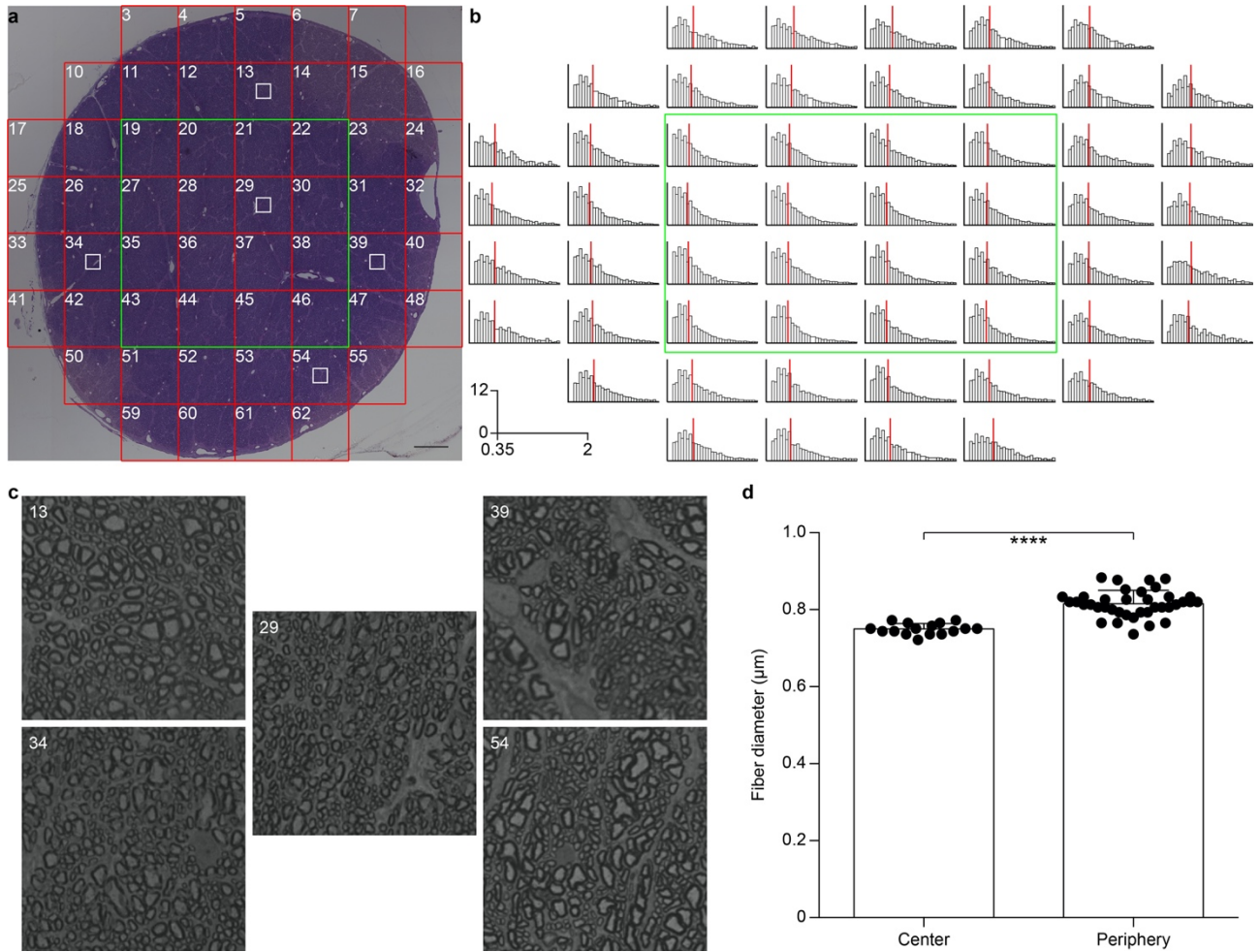
2.7 Supplementary Material



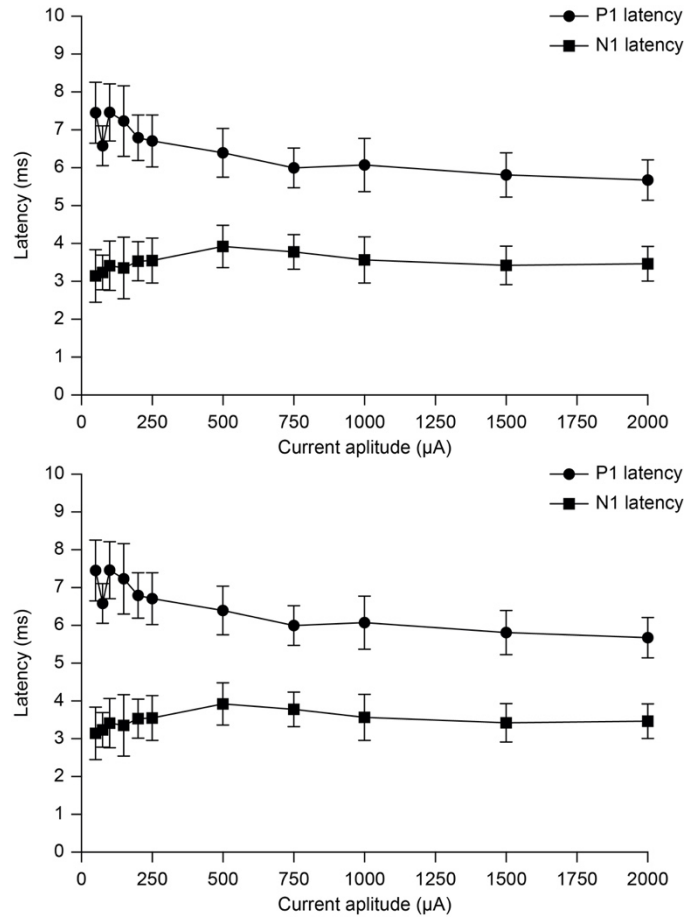
Supplementary Figure 2-1 | Optic nerve dimension. (a) Representative nerve explanted from a New Zealand White rabbit and embedded in optimal cutting temperature compound before freezing. (b) Representative transverse section extracted 1 mm close to the optic chiasma from the optic nerve in a. The scale bar is 0.5 mm. Experiment repeated on $n = 10$ nerves. (c) Quantification of the mean nerve diameter (\pm s.d., $n = 10$ nerves). For each nerve, we collected three sections and computed the average diameter.



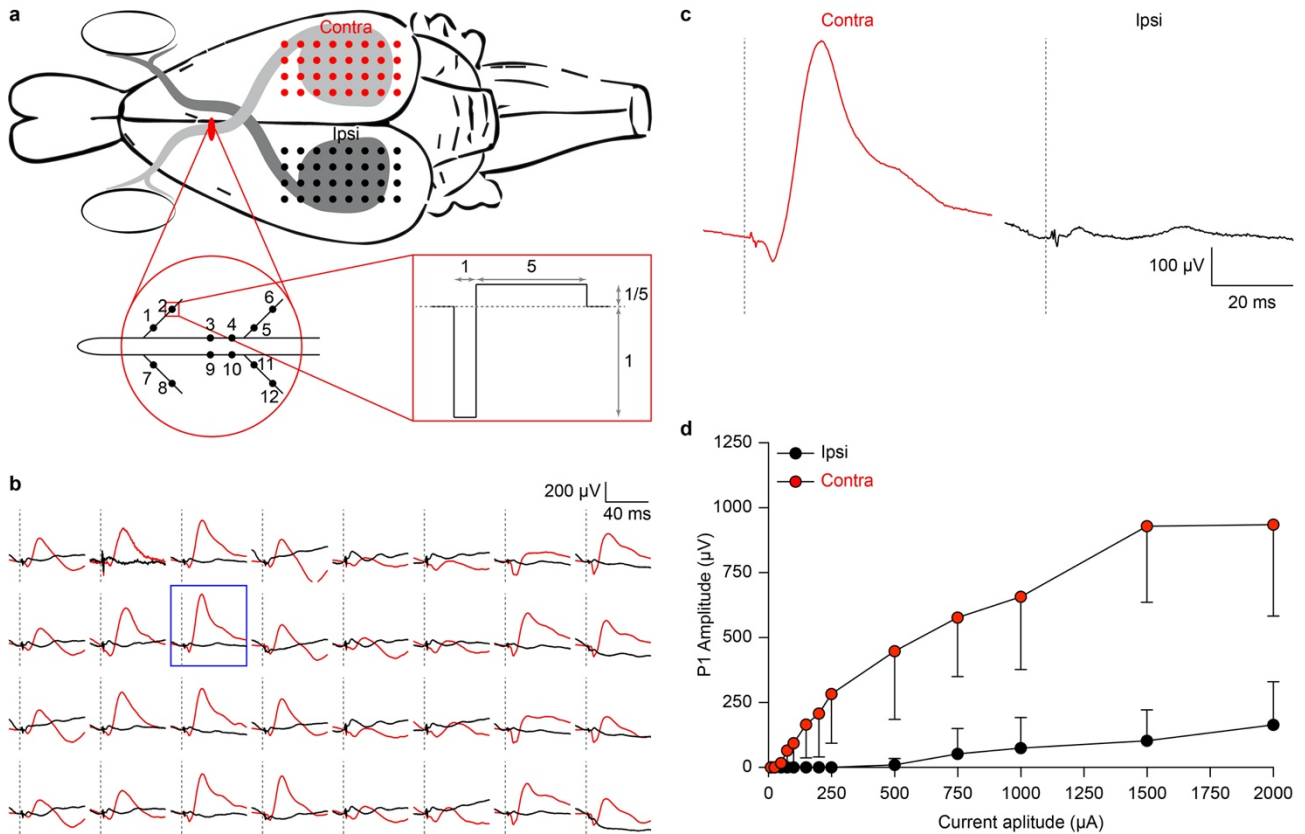
Supplementary Figure 2-2 | Evaluation of optic nerve fatigue. Normalized P1 PAs upon 10 stimulations consisting of 1 (a), 2 (b), 3 (c), or 4 (d) pulse trains at 1 kHz of repetition rate; representative example from N = 1 rabbit, repeated on N = 4 rabbits. Each PA is normalized with respect to the average PA out of the 10 repetitions. Each plot shows the mean (\pm s.d.) P1 PAs at increasing current amplitudes (reported only from 750 to 2000 μA since were most subjected to fatigue). For each data point, the responses from n = 6 stimulation electrodes of the OpticSELINE (from 1 to 6, top side) were averaged.



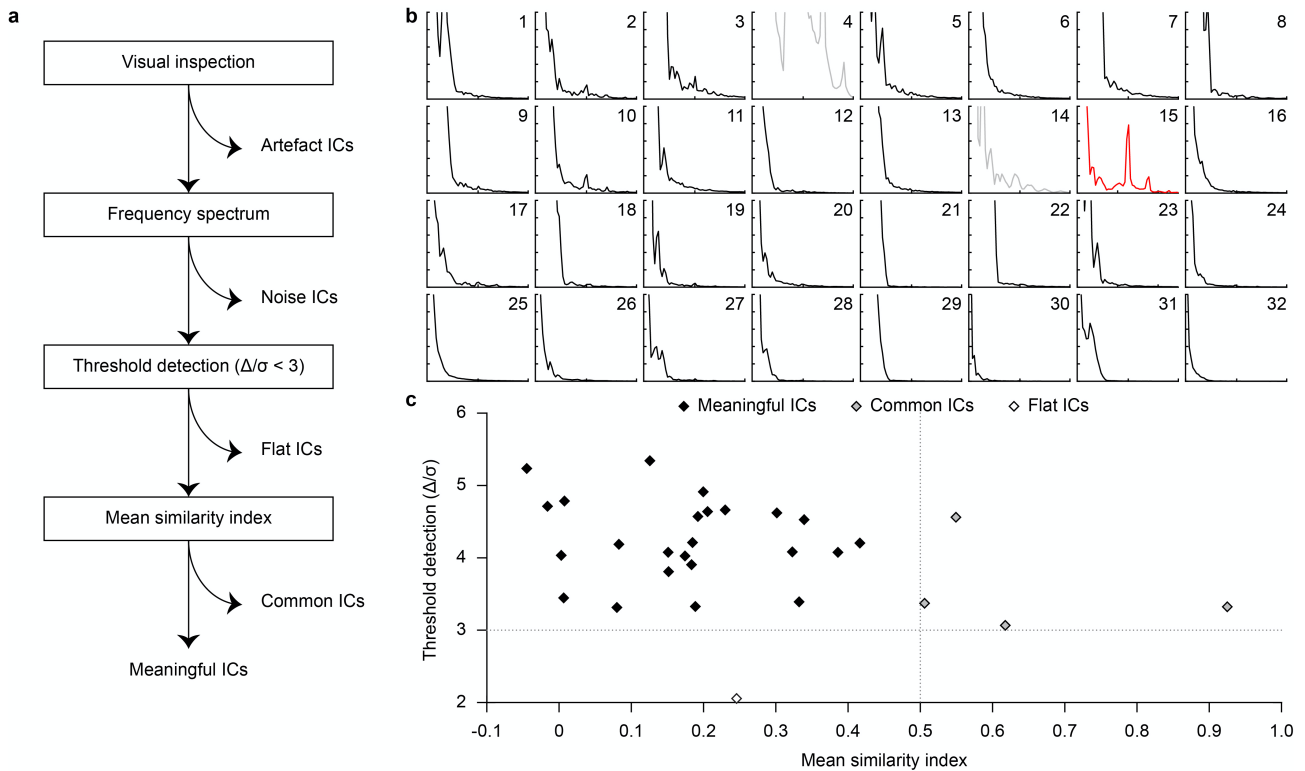
Supplementary Figure 2-3 | Distribution of the optic nerve fibres. **(a)** Histological section of the rabbit optic nerve. The red boxes represent the segmentation used for quantification. The green box is the area considered as the centre of the nerve. The scale bar is 100 μm . Experiment repeated on $n = 1$ nerve. **(b)** Distribution of the optic nerve fibres for each red box in a. The x-axis is the fibre diameter (plotted from 0.35 to 2 μm , bins of 0.05 μm). The y-axis is the percentage probability (plotted from 0 to 12 %). The red lines are the medians of each distribution. **(c)** Magnification of 5 regions (out of 54) of the optic nerve, corresponding to the white boxes in a. The scale bar is 10 μm . **(d)** Quantification of the mean (\pm s.d. center: $n = 16$; periphery: $n = 38$) median of the fibre distribution in the centre of the nerve (green box in panel a) and in the periphery (**** $p < 0.0001$, two-tailed unpaired t-test).



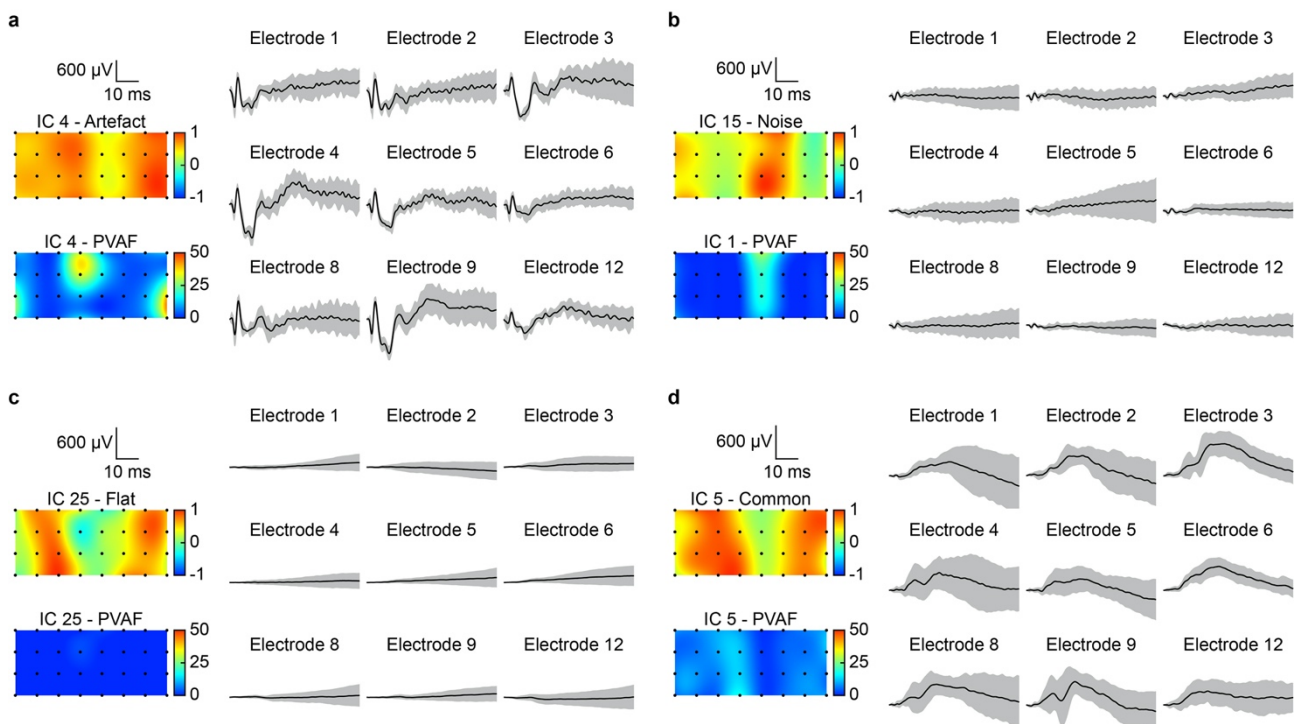
Supplementary Figure 2-4 | Latency of the electrically-evoked cortical potentials. Mean (\pm s.e.m., $N = 4$ rabbits) PLs of N1 (squares) and P1 (circles) peaks for current pulses of $150 \mu\text{s}$ as a function of the current amplitude. For each rabbit, 10 consecutive recordings were averaged. PAs were quantified for each stimulating electrode of the OpticSELINE ($n = 6$) from the averaged response of the 32 recording electrodes. The resulting values were averaged between the $n = 6$ stimulating electrodes.



Supplementary Figure 2-5 | Ipsilateral and contralateral electrically-evoked cortical potentials. (a) EEPs were evoked via the implanted OpticSELINE with biphasic current pulses. Recordings of EEPs were performed with ECoG arrays covering both the ipsilateral (black) and contralateral (red) visual cortices. (b) Representative example of responses (synchronous average of 10 responses) to a current pulse of 250 μA and 150 μs delivered from the electrode 2. The dashed lines represent the occurrence of the current pulse. Experiment repeated on $N = 1$ rabbit. (c) Magnification of the traces obtained from one recording electrode (blue box in b) for both ipsi- (black) and contra- (red) lateral recordings. The dashed lines represent the occurrence of the current pulse. (d) Mean (\pm s.d., $n = 12$ stimulating electrodes from $N = 1$ rabbit) P1 PAs as a function of the current amplitude in contralateral (red) and ipsilateral (black) recordings. 10 consecutive recordings were averaged. PAs were quantified for each stimulating electrode of the OpticSELINE ($n = 12$) from the averaged response of the 32 recording electrodes.

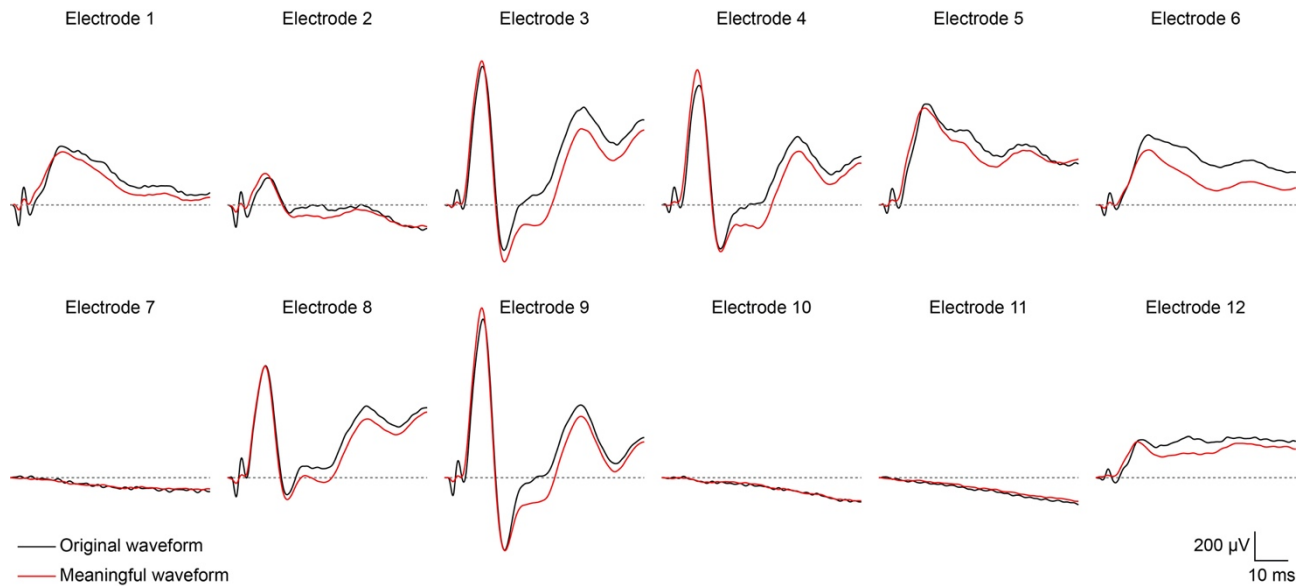


Supplementary Figure 2-6 | Method for the classification of independent components. (a) Step by step process for the classification of ICs. **(b)** Frequency plot of the time course of the ICs. The y-axis is the power (from 0 to 25,000) while the x-axis is the frequency (from 0 to 500 Hz). The noisy IC (number 15, red) has been identified by the 2 peaks occurring at frequencies higher than 250 Hz. IC 4 and IC 14 (grey) have been already visually classified as artefact ICs. **(c)** Identification of the flat IC (number 25) based on the threshold detection and the common ICs (numbers 5, 8, 11, and 29) based on the mean similarity index. The horizontal grey dotted line is the threshold for discrimination for flat ICs ($\Delta\sigma < 3$), while the vertical grey dotted line is the threshold for discrimination for common ICs (0.5). Panels b and c shows a representative example from $N = 1$ rabbit with a current amplitude of $750 \mu\text{A}$. Experiment repeated on $N = 4$ rabbits.

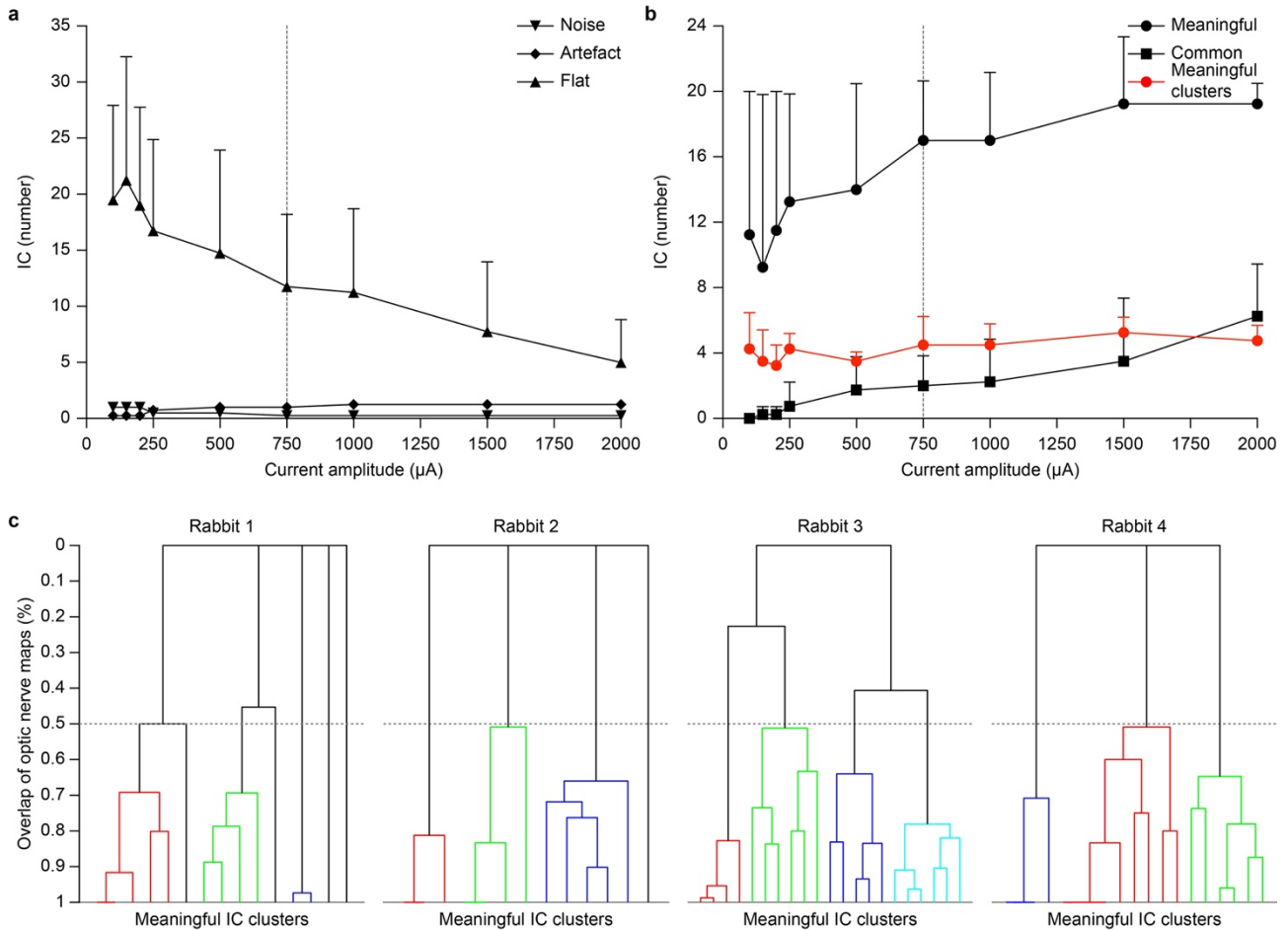


Supplementary Figure 2-7 | Representative example of non-meaningful independent components. (a) Example of an artefact component (IC 4). It contains the stimulation artefact. **(b)** Example of a noise component (IC 15). It contains high-frequency oscillations.

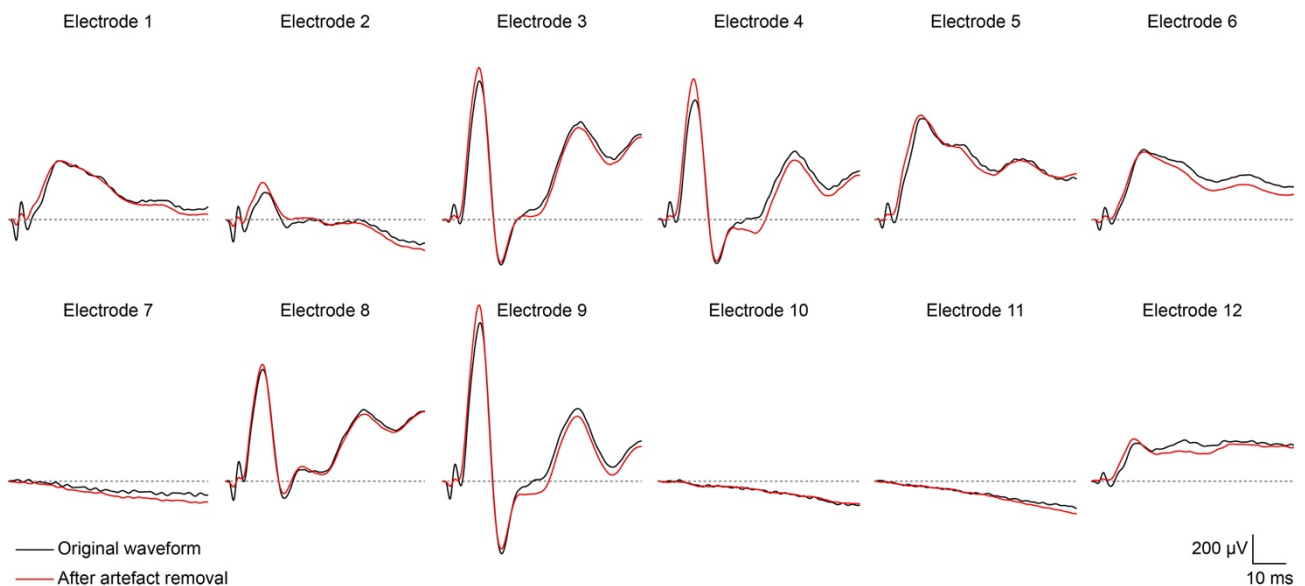
IC 4 can be considered also as an example of a noisy component since it contains also high-frequency oscillations. **(c)** Example of a flat component (IC 25). It does not contain any peaks in the waveform. **(d)** Example of a common component (IC 5). It has a similar waveform for each of the stimulating channels. For each panel, on the left side, there are the activation maps obtained with the weight of the ICs and the percentage of variance accounted for (PVAF). On the right side, there are the mean (\pm s.d., 10 repetitions) IC for each of the working stimulating channels (3 out of the 12 did not induce a meaningful cortical response).



Supplementary Figure 2-8 | Back-projections of the meaningful independent components. Plot of the original recorded EEPs (black) and the back-projections of the meaningful ICs (red), obtained by multiplying the IC time courses by the mixing matrix while setting the weights of the 'shared' ICs to zero. In this representative example ($N = 1$ rabbit, current amplitude of $750 \mu\text{A}$), the stimulating channels 7, 10, and 11 did not result in a meaningful cortical activation. Experiment repeated on $N = 4$ rabbits.



Supplementary Figure 2-9 | Classification of the independent components. (a) Mean (\pm s.d.) number of ICs classified as artefact, noise, or flat depending on the current amplitude in $N = 4$ rabbits. (b) Mean (\pm s.d.) number of ICs classified as common or meaningful depending on the current amplitude in $N = 4$ rabbits. The mean (\pm s.d.) number of meaningful clusters is plotted in red. (c) Dendrograms of the hierarchical clustering of the meaningful ICs for each rabbit. The threshold to determine the meaningful ICs that are part of the same cluster has been set to a minimum overlap of 50% (grey dashed lines).



Supplementary Figure 2-10 | Back-projections after artefact removal. Plot of the original recorded EEPs (black) and the back-projections after artefact removal (red), obtained by multiplying the IC time courses by the mixing matrix while setting the weights of

the artefact ICs to zero. Representative example from N = 1 rabbit with a current amplitude of 750 μ A. Experiment repeated on N = 4 rabbits.

Chapter 3 A machine-learning algorithm correctly classifies cortical evoked potentials from both natural retinal stimulation and electrical stimulation of the optic nerve

Manuscript of the article submitted to Journal of Neural Engineering, January 2021.

Authors: Vivien Gaillet ^a, Eleonora Borda ^a, Elodie Geneviève Zollinger ^a, and Diego Ghezzi ^a

^a Medtronic Chair in Neuroengineering, Center for Neuroprosthetics and Institute of Bioengineering, School of Engineering, École polytechnique fédérale de Lausanne, Geneva, Switzerland.

Authors contributions : V.G. designed the stimulation protocol and the classification and regression algorithm, and performed the data analysis, and wrote the manuscript. E.B. performed in vivo experiments. E.G.Z. performed in vivo experiments. D.G. designed the study, led the project and wrote the manuscript. All the authors read, edited, and accepted the manuscript.

3.1 Abstract

Objective. Optic nerve's intraneural stimulation is an emerging neuroprosthetic approach to provide artificial vision to totally blind patients. An open question is the possibility to evoke individual non-overlapping phosphenes via selective intraneural optic nerve stimulation. To begin answering this question, first, we aim at showing in preclinical experiments with animals that each intraneural electrode could evoke a distinguishable activity pattern in the primary visual cortex.

Approach. We performed both patterned visual stimulation and patterned electrical stimulation in healthy rabbits while recording evoked cortical activity with an electrocorticogram array in the primary visual cortex. Electrical stimulation was delivered to the optic nerve with the intraneural array OpticSELINE. We used a support vector machine algorithm paired to a linear regression model to classify cortical responses originating from visual stimuli located in different portions of the visual field and electrical stimuli from the different electrodes of the OpticSELINE.

Main results. Cortical activity induced by visual and electrical stimulation could be classified with nearly 100% accuracy relative to the specific location in the visual field or electrode in the array from which it originated. For visual stimulation, the accuracy increased with the separation of the stimuli and reached 100% for separation higher than 7 degrees. For electrical stimulation, at low current amplitudes, the accuracy increased with the distance between electrodes, while at higher current amplitudes, the accuracy was nearly 100% already for the shortest separation.

Significance. Optic nerve's intraneural stimulation with the OpticSELINE induced discernible cortical activity patterns. These results represent a leap forward for intraneural optic nerve stimulation towards artificial vision.

3.2 Introduction

Blindness is a medical condition impairing the quality of life of the affected people and their relatives; hence it represents a high medical, economic and social cost for society. While therapies are available for several pathologies causing vision loss and blindness, some others currently have no treatment¹⁵⁵. Among these diseases, retinitis pigmentosa is a set of inherited retinal rod-cone dystrophies with a prevalence of about 1:4,000 individuals causing the progressive loss of rod photoreceptors, loss of night vision and the constriction of the visual field (tunnel vision), later followed by cone dysfunctions and eventually profound blindness¹⁷⁷. The degeneration of retinal photoreceptors characterises retinitis pigmentosa. Consequently, the other retinal neurons (i.e. bipolar cells, amacrine cells and retinal ganglion cells) are generally considered to be preserved and to form a functional network that can be activated via electrical stimulation evoking the sensation of discrete points of light called phosphenes. Artificial vision is the perception of the world using an ensemble of these phosphenes. Retinal prostheses have been extensively investigated in animal experiments^{220,221,273,280,301,317,318} and in retinitis pigmentosa patients to fight blindness^{319–321}. However, none of these devices is available in clinics today, and the few that were available have been discontinued.

Large clinical studies with retinal implants in retinitis pigmentosa patients showed a large performance variability^{222,223,322}. The number of functional electrodes able to elicit phosphenes with the Argus® II retinal implant was variable, as low as 5 out of 60³²². Postoperative outcomes were also variable, from just phosphenes perception to object recognition and reading capability³²². Similar variable outcomes were observed in retinitis pigmentosa patients implanted with the Alpha-IMS/AMS subretinal prostheses, ranging from just light perception to restoration of partial visual acuity²²³. Variable perceptual outcomes could be attributed to the advance stage of retinal degeneration. In late-stage retinitis pigmentosa patients, post-mortem retina analysis revealed that 78% of bipolar cells and 30% of retinal ganglion cells are spared, while it was the case for only 5% of photoreceptors^{178,186,187,323}. However, there are divergent opinions about the functional integrity of retinal circuits. While some studies reported the anatomical and functional preservation of retinal ganglion cells in both humans and animal models^{186,324,325}, some others documented the remodelling and reorganisation of the synapses in the inner nuclear layer^{235,236}, which might compromise the efficacy of electrical stimulation^{237–239,326}. The deafferentation of bipolar cells caused by photoreceptors' death is followed by a negative plasticity period, which is not fully understood. Changes in synaptic connectivity might form aggregates of synaptic connexions between survival cells, known as microneuromas, which are presumably the source of the spontaneous retinal hyperactivity^{237,238,327}. These plastic events might create connectivity loops, reducing the retinal excitability and impairing the ability to encode visual information with retinal implants³²⁸. Retinal network-mediated stimulation in retinitis pigmentosa patients is also subjected to rapid phosphene's fading due to static adaptation and bipolar cells' desensitisation³²⁹: a phenomenon requiring cognitively exhausting large head and body movements to counteract it. Therefore, bypassing the retinal network might be an attractive strategy to reduce the variability in retinal stimulation. One approach was developed by the AV-DONE project based on an intrapapillary electrode array^{330,331}. A retinitis pigmentosa patient implanted with three wires reported the perception of distinguishable phosphenes upon stimulation of the optic disc²²⁹.

Long-term mechanical stability of epiretinal prostheses is another critical element leading to an increase in the stimulation threshold associated with the increase of the electrode-to-retina distance^{212,213}. Also, several exclusion criteria limit the eligibility for retinal prostheses, as appeared from enrolment criteria in several clinical trials, and here summarised: retinal detachment or trauma, sub-macular choroidal neovascularization, extremely thin conjunctiva, too small or too long axial length, corneal ulcers, abnormalities in the typical

curvature of the retina, eyeball trauma, and corneal opacity or lack of optical transparency preventing adequate visualisation of the inner structures of the eye or impeding the correct placement of the device. Retinal prostheses might not be limited by all those criteria simultaneously since some of them might apply only to specific implants. However, optic nerve's direct electrical stimulation appears an attractive strategy to circumvent all the above-mentioned limitations in a single step. Another consideration is the restored visual angle. Previous studies pointed out that retinitis pigmentosa patients would benefit from the restoration of a wide visual angle^{332,333}. Although some wide-field retinal prostheses are under development^{334,335}, optic nerve's stimulation is attractive because its relatively small diameter facilitates the electrical stimulation of a wide visual field.

Early studies on optic nerve's stimulation were performed in retinitis pigmentosa patients^{226,276}. The first subject received a 4-contacts self-sizing cuff electrode around the intracranial segment of the optic nerve. Following psychophysical testing, the subject correctly identified basic shapes and character-like symbols, even if the phosphenes were reported as unstable, possibly due to the device's movement caused by the poor anchorage of the cuff electrode. Following these results, the C-sight project proposed an optic nerve prosthesis based on a few (3 to 5) penetrating rigid and stiff microelectrodes and tested the concept in pre-clinical experiments^{234,284}. An optic nerve prosthesis (OpticSELINE) was also proposed by our group³³⁶. Compared to other approaches, the OpticSELINE provides higher mechanical stability due to its three-dimensional anchoring wings, better mechanical compliance because of thin-film microfabrication on polymeric materials and higher electrodes' number because of the high integration capacity of cleanroom processes. Despite early clinical studies in humans^{226,229,276} and preclinical experiments in animals^{234,284,336}, optic nerve stimulation is not mature yet for clinical use. Several technical improvements and validations are still required, such as electrode miniaturisation, increase of the electrodes' number and density, long-term biocompatibility assessment in the optic nerve and demonstration of localised and non-overlapping phosphenes when multiple electrodes are activated simultaneously or in rapid succession. A step towards this latter goal is to show that the stimulation through different electrodes induces distinguishable cortical activity patterns, suggesting that different fibres of the optic nerve are recruited, and non-overlapping phosphenes might be evoked.

Preclinical studies in animals often rely on the peak-to-peak analysis of electrocorticogram (ECoG) recordings to determine the portion of the visual cortex activated by the stimulation. However, ECoG recordings with microelectrodes are often limited by low spatial resolution. A recent report found that the cortical tissue around an ECoG electrode that contributes to its activity is approximately 3-mm in diameter³³⁷, most likely because of the volume conduction of the potentials. The mapping of spatially organised cortical activity patterns in relatively small animals could be hindered, if not prohibited, by this physical limitation. On the other hand, a previous study presenting letters to a rhesus monkey demonstrated that machine-learning algorithms might overcome this problem since they benefit from the information of the whole spectrogram of ECoG recordings³³⁸. Therefore, we propose a machine-learning approach not relying exclusively on the peak-to-peak amplitude but encompassing the whole signal spectrogram to correctly classify and predict the ECoG signal originating from patterned visual stimulation and optic nerve's intraneural electrical stimulation. First, we validated the algorithms using patterned visual stimuli. Then, we demonstrated that the cortical signals evoked by electrical stimulation from different electrodes of the OpticSELINE were correctly classified and predicted.

These results represent a leap forward for intraneural optic nerve stimulation towards an artificial vision. Also, this approach might have wide use in neuroprosthetics for the preclinical validation of visual prostheses and other sensory prostheses.

3.3 Material and Methods

3.3.1 Animal handling and surgery

Animal experiments were performed according to the authorisation GE519 approved by the Département de l'Emploi, des Affaires Sociales et de la Santé, Direction Générale de la Santé of the République et Canton de Genève (Switzerland). Female rabbits (>16 weeks, >2.5 kg) were premedicated 30 min before the transfer to the surgical room with an intramuscular injection of xylazine (3 mg kg⁻¹; Rompun® 2%, 20 mg ml⁻¹, 0.15 ml kg⁻¹), ketamine (25 mg kg⁻¹; Ketanarkon® 100 mg ml⁻¹, 0.25 ml kg⁻¹) and buprenorphine (0.03 mg kg⁻¹; Temgesic® 0.3 mg ml⁻¹, 0.1 ml kg⁻¹). Rabbits were left under 100% O₂. 10 to 15 min after premedication, a 22G catheter was placed in the ear's marginal vein. Local anaesthesia was provided to the throat (Xylocaine 10%, spray push). The rabbit was intubated with a 3.5-mm tracheal tube with a balloon and ventilated (7 ml kg⁻¹, rate: 40/min, positive end-expiratory pressure: 3 cm of H₂O). Eye gel (Lacrigel) was placed on the eye to protect it from drying. Anaesthesia and analgesia were provided intravenously with propofol (10 mg kg⁻¹ h⁻¹; 20 mg ml⁻¹, 0.5 ml kg⁻¹ h⁻¹) and fentanyl (0.005 mg kg⁻¹ h⁻¹; 0.05 mg ml⁻¹, 0.1 ml kg⁻¹ h⁻¹). Rabbits were placed on a heating pad at 35 °C for the entire surgery. The depth of anaesthesia was monitored continuously throughout the procedure, including heart rate, temperature and pulse oximetry. Fluid supplementation was administered intravenously to prevent dehydration (physiological solution 20-35 ml kg⁻¹, IV). The rabbit's head was shaved and secured gently within a stereotactic frame (David Kopf Instruments). Before cortical skin incision, lidocaine (6 mg kg⁻¹; Lidocaine 2%, 20 mg ml⁻¹, 0.3 ml kg⁻¹) was injected subcutaneously at the surgical sites. After 5 min, the skin was opened and pulled aside to clean the skull with cotton swabs. A craniotomy was made to expose the visual cortex. A 32-channel epidural ECoG array (E32-1000-30-200; NeuroNexus) was placed over V1. For electrical stimulation, a frontotemporal craniotomy was made to access the optic nerve. The intraneural electrode array was inserted in the optic nerve in the pre-chiasmatic area. The surgical implantation was performed by piercing the nerve with a needle (nylon black DLZ 4,8-150 10/0, FSSB) and by guiding the intraneural electrode array transversally into the nerve. All rabbits were euthanised at the end of the acute recording procedures while still under anaesthesia, with an intravenous injection of pentobarbital (120 mg kg⁻¹).

3.3.2 Electrophysiological recording and stimulation

For patterned visual stimulation, white rectangles were projected (ML750ST; Optoma) on a reflective screen placed approximately 90 cm away from the rabbit. The projected area covered 28 x 44 degrees of the visual field, and the full luminance of the projector was 530 cd m⁻². Rectangles of 1/4th of the screen's size (14 x 22 degrees) were projected in 10 different locations along the horizontal meridian separated by 2.2 degrees. Each stimulus lasted for 16 ms (based on the projector frame rate). Sixty flashes were presented for each stimulus location. For patterned electrical stimulation, two microelectrode arrays were used: Flat-OpticSELINE and OpticSELINE. The OpticSELINE was previously described by our group [44]. Briefly, it is a polyimide-based looped microelectrode array. Six microelectrodes (0.0078-mm² area) are located on each side of the OpticSELINE, with a reference electrode and a ground electrode placed outside the active area. Two three-

dimensional flaps extend from both sides of the main body and carry two electrodes each; two more electrodes are located on each side of the main body. The dataset with the OpticSELINE was obtained from the previous experiment [44], during which only the six electrodes on the top side were used for stimulation. The Flat-OpticSELINE is a modified version of the OpticSELINE. The array is a single polyimide strip with a linear and planar distribution of eight electrodes (40- μm diameter, 160- μm pitch, 0.0013- mm^2 area) with a reference electrode and a ground electrode placed outside the active area. The microelectrode array was attached to a current stimulator (IZ2MH; Tucker-Davis Technologies). Optic-nerve stimulation was performed with 150- μs biphasic cathodic-first current pulses (asymmetric: 750- μs anodic phase at one-fifth of the cathodic amplitude) at various cathodic current amplitudes (10, 25, 50, 75, 100, 150, 200, 250, 500, 750, 1,000, 1,500 and 2,000 μA) delivered in a scrambled manner. For each electrode and current amplitude, 30 stimuli were delivered with the Flat-OpticSELINE and 10 with the OpticSELINE. For cortical recordings, an ECoG array composed of 32 (4 \times 8) platinum electrodes with a diameter of 200 μm and a pitch of 1 mm (E32-1000-30-200; NeuroNexus) was placed over V1 contralateral to the stimulated eye and connected to an amplifier (PZ5; Tucker-Davis Technologies) via a 32-channel analogue head stage (ZIF-Clip Analog Headstage; Tucker-Davis Technologies). Data were filtered between 0.1 and 500 Hz and digitised at 12 kHz. Epochs synchronous to the stimulation's onset (from -100 ms to +750 ms) were then extracted from the data stream and analysed with MATLAB (MathWorks).

3.3.3 Signal processing and feature extraction

The ECoG signal was band-pass filtered between 3 and 500 Hz, then offset by a value equal to the average voltage of the 100-ms preceding the stimulus's onset. The signal spectrogram was computed with a built-in MATLAB function (continuous 1-D wavelet transform) using the Morlet wavelet to extract the frequency bands from 10 to 300 Hz. The wavelet power was obtained by squaring two times the magnitude of the wavelet transform. The wavelet power was then normalised by subtracting the average power of the 100 ms before the stimulus's onset and then dividing the result by the same value for each frequency bands (baseline-correction). Nine classes of features were extracted from the time course portion from 5 ms after the stimulus's onset (to remove the stimulus artefact that occurs between 0 to 4 ms) to 100 ms after the stimulus. The continuous features named 'Time' and 'Slope' consist of the time course itself ('Time') and its derivative ('Slope'). The punctual features named 'PA' and 'PL' consisted of the VEP signal's peak amplitude ('PA') and the positive peak's latency ('PL'). The broad-band gamma power ('BGP') was obtained by averaging the frequency bands from the wavelet power ranging from 40 to 150 Hz. The punctual features in the frequency domain named 'Power Amplitude', 'Power Frequency' and 'Power Timing' correspond respectively to the maximum value of the power wavelet spectrogram, its frequency and its timing. Finally, the wavelet power spectrogram was down-sampled in the time axis from 12 kHz down to 1200 Hz and used as the continuous feature named 'Power'.

3.3.4 Classification and regression

For patterned visual stimulation and patterned electrical stimulation with the Flat-OpticSELINE, both a classification and a linear regression were performed. For patterned electrical stimulation with the OpticSELINE, only the classification was performed. The classification was performed in MATLAB using a support vector machine algorithm (SVM), determining the hyperplane in the feature space that maximises the margins (the projection of the data points on the hyperplane). The SVM algorithm was used with the MATLAB error-correction output codes allowing the SVM classifier to be used on a multi-class data set. No kernel function was

used. We ran 6-fold cross-validation, where 5/6 of the observations were used for training (training set) and 1/6 for testing (testing set). The classification was repeated on 6 different pairs of training and testing sets. The final classification accuracy score was the average of the 6 trials. Features' selection was performed on the training set only. We first conducted the classification on all the stimuli at once for patterned visual stimulation and patterned electrical stimulation with the Flat-OpticSELINE. Then, we computed the classification accuracy between pairs to evaluate the impact of the distance between stimuli or electrodes on the classification accuracy. For patterned electrical stimulation with the OpticSELINE, the classification was conducted on all the stimuli at once only. Then, the correlation coefficient between the features and the stimuli' location was computed, and a regression model was built with the features with the highest absolute correlation coefficient value. The model takes the form of $y = \beta_0 + \beta_1 X_1 + \beta_2 X_2 + \beta_3 X_3 + \dots + \beta_n X_n + \epsilon$, where X_1 to X_n are the features used as input, β_0 to β_n are the weights of the features, ϵ is the error term, and y is the predicted location of the rectangle's centre or the electrode's position. The observations were split into training and testing sets of a size equal to 5/6 and 1/6 of the total number of observations, which was repeated 60 times for patterned visual stimulation and 30 times for patterned electrical stimulation with the Flat-OpticSELINE to gradually shift the testing sets by an increment equal to the number of stimulations. The average model predictions and the root-mean-square error (RMSE) were reported as the average values of the different splits.

3.4 Results

3.4.1 Patterned visual stimulation

We took advantage of patterned visual stimulation to validate the SVM classification algorithm on ECoG recordings (Figure 3-1). An anaesthetised rabbit was placed in front of a screen (Figure 3-1a), and white flash stimuli (14 x 22 degrees rectangles) were projected on dark background in 10 different locations along the horizontal meridian (red dots in Figure 3-1b). Visually evoked potentials (VEPs) elicited by patterned visual stimulation (Figure 3-1c) were detected using the ECoG electrode array placed over V1 contralateral to the stimulated eye. Strong patterned flash stimulation was selected among the various stimuli used in vision research to mimic the strong and fast activation induced by electrical stimulation as closely as possible. Flashes and electric pulses are both fast transients, not physiological in normal vision. Also, electrical stimulation elicits phosphenes, and a focalised flash is the closest stimulus to a phosphenes. Despite these similarities, electrically evoked responses do not necessarily match visually evoked responses since electrical stimulation bypasses both phototransduction and the retinal network. Also, flashes are two orders of magnitude longer than electric pulses (16 ms and 150 μ s, respectively).

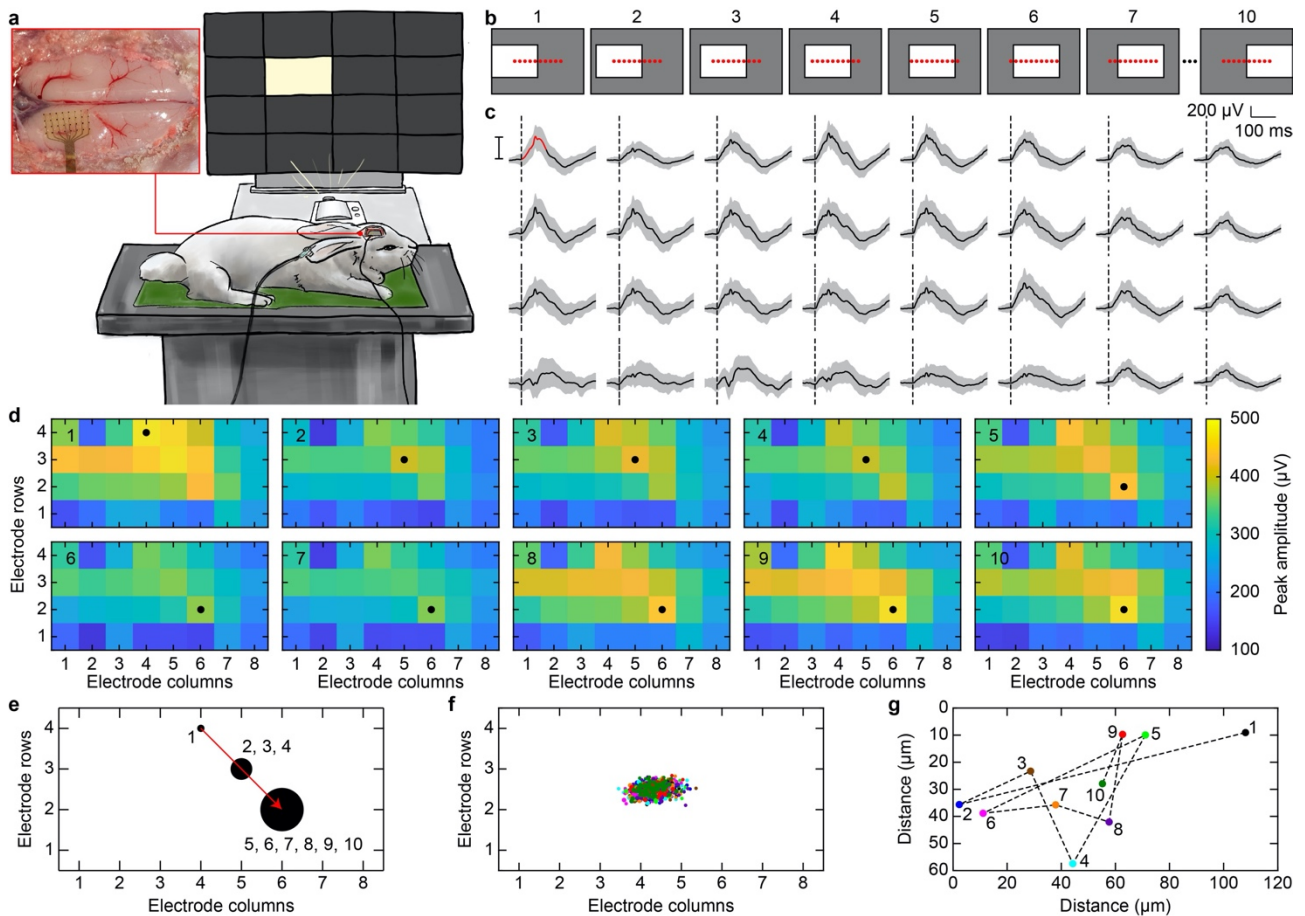


Figure 3-1. (a) Sketch of the experimental setup for visual stimulation. An anaesthetized rabbit is placed in front of the screen on which the light stimuli are projected. The red square shows an enlarged picture of the ECoG recording electrode array placed over V1 (post-mortem image). (b) Schematic representations of the patterned visual stimulation. The red dots are the centre of the white rectangles. (c) Representative example of the 32 VEPs recorded with the ECoG electrode array upon presentation of one visual stimulus. The black trace is the average of 60 repetitions, while the s.d. is the grey area. The trace in the top left corner shows the quantification of the peak-to-peak amplitude in the early portion of the signal (100 ms). The black dashed lines are the light stimulus onset. (d) Averaged activity maps among the 60 repetitions obtained for each visual stimulus location. In each map, the number in the upper left corner indicates the stimulus location, while the black circle indicates the leading channel. (e) Map of the channels identified as leading channels. The black circles' size is proportional to the number of times the electrode is identified as the leading channel. The numbers next to the circles correspond to the stimulus locations leading to the electrode being identified as the leading channel. The red arrow identifies the leading channel's shift. (f) Distributions of the centres of the activity map. Each circle corresponds to a single activity map upon one visual stimulus (60 circles for each stimulus location). Each colour corresponds to one stimulus location as in (g). (g) Shifts of the average centre of the activity maps. Each circle is the average of the centres originating from a stimulus location. The numbers correspond to the stimulus location associated to a colour code.

One of the most commonly used approaches to determine what part of the visual cortex is activated by a stimulus is measuring the leading channel's shift²⁸⁴, which is the electrode with the highest peak-to-peak amplitude. This approach has been successfully used to determine retinotopic organisation in the visual cortex when paired with intracortical recordings. However, the low spatial resolution of ECoG microelectrodes might be inadequate for this task. In our dataset, we computed the activity map for each visual stimulus in each location as the peak-to-peak amplitude for each recording electrode. The 60 activity maps corresponding to a stimulus location have been averaged (Figure 3-1d), revealing that 3 leading channels appeared out of the 10 stimulus locations upon patterned visual stimulation (Figure 3-1e). The shift in the leading channel is coherent with the stimulus's shift (from temporal to nasal) according to previously reported visual maps^{233,339,340}. However, the limited spatial resolution of the recording system and analysis method provides only three hot-spots, which are not enough to identify distinguishable pattern of activation for each stimulus

location. Therefore, we evaluated the whole activity maps. First, we computed the distribution of the centre of mass for each activity map (Figure 3-1f), and they resulted in overlapping distributions lacking significant clustering. Then, we computed the average centre of the distributions and evaluated the shift, which is in the order of one hundred microns and occurring in directions not coherent with the visual stimulus's horizontal motion. These results indicate that the cortical activity map measured by the ECoG electrode array was not affected by the visual stimulus's location (Figure 3-1g).

The shifts of both the leading channel and the centre of mass alone are not a good estimator of the cortical activity pattern's modulation upon variation of the stimulus location when recordings are made with ECoG microelectrodes, since they are both based only on the signal peak-to-peak amplitude. Therefore, we sought an alternative method encompassing more exhaustive information about the elicited cortical signal to identify the stimulation corresponding to a particular activation pattern in the visual cortex. We investigated a machine-learning approach to isolate the most informative features leading to a finer analysis of the cortical signals, highlighting differences among signals generated by different stimuli. The hypothesis is that the similarity between signals will decrease when the areas of stimulation within the visual field are further apart, which will be reflected by higher classification accuracy.

The machine-learning workflow classified the signal originating from patterned visual stimulation based on two types of features extracted from the 32 VEP time courses: continuous or punctual. The continuous features are the signal time course ('Time', Figure 3-2a in red), its derivative ('Slope', Figure 3-2b in red) and its broad-band gamma power ('BGP', Figure 3-2c). The punctual features, which have a single value per time course, are the peak-to-peak amplitude of the VEP signal ('PA') and the latency of the positive peak ('PL') (Figure 3-2a). In addition to the features derived from the time course, we included features containing information about the frequency domain to broaden the possible features. Therefore, we added continuous features consisting of each pair of time points and the power spectrogram frequency (which was down-sampled by a factor 10 in time). From the power spectrogram, we extracted three punctual features: amplitude ('Power Amplitude'), frequency ('Power Frequency') and timing ('Power Timing') of the maximum of the power spectrogram (red cross in Figure 3-2c). Last, the wavelet power spectrogram was down-sampled in the time axis from 12 kHz down to 1200 Hz and used as the continuous feature ('Power'). All the features were concatenated in a single matrix for feature selection.

Since specific portions of the signal or some signal features are more informative than others, we applied a feature selection approach on the training set only. The very large number of features made some feature selection approaches computationally expensive, so we opted first to do a pre-selection test by computing the chi-score of all the individual features. We then proceeded to test different features selection algorithms (minimum redundancy maximum relevance, chi-squared test, reliefF and randomly selected features) on the 5% of the features with the highest chi-score (Figure 3-2d). We selected the minimum redundancy maximum relevance (MRMR) algorithm for our future analysis, as this algorithm resulted in the highest classification accuracy. When the number of selected features is disproportionally large compared to the number of observations, overfitting may occur: the RMSE of the training set converges to zero, while the RMSE of the testing set increases drastically. To avoid overfitting, we selected the best 200 features returned by the MRMR algorithm (one-third of the total number of observations) for which the RMSE of the testing set was minimized, and we used them as an input of a support machine vector classifier. The MRMR algorithm returned a classification accuracy 70.67% with 200 features (Figure 3-2d).

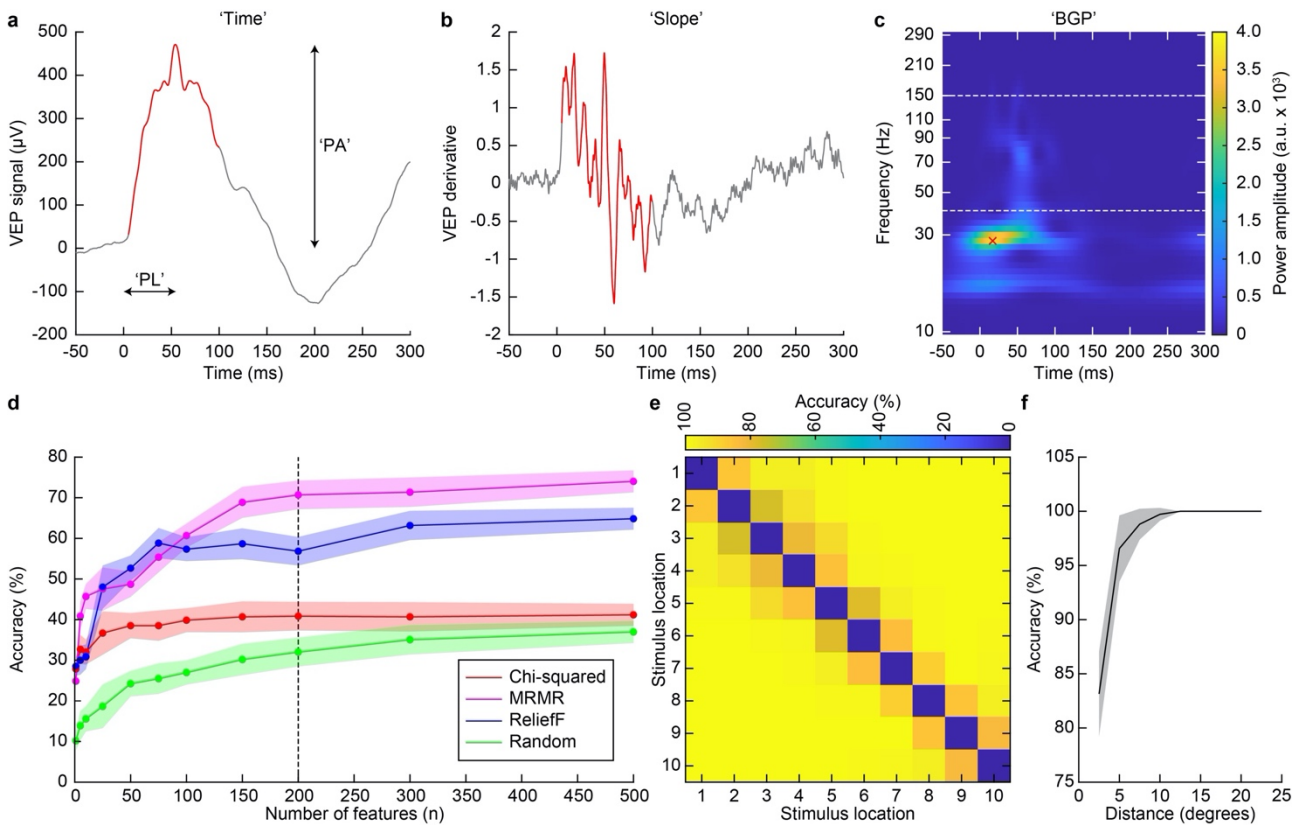


Figure 3-2. (a) Representative VEP signal highlighting the peak-to-peak amplitude and the positive peak latency. The red portion of the signal corresponds to the time course used as a feature from 5 ms to 100 ms. (b) Derivative of the VEP signal in a. The red portion of the signal is the one used as a feature from 5 ms to 100 ms. (c) Representative spectrogram from the VEP signal in a. The white dashed lines indicate the frequency band corresponding to the 'BGP'. The red cross highlights the 'Power Amplitude', the 'Power Frequency' and the 'Power Timing'. (d) Average (\pm s.d., 6 repetitions) classification accuracy of the feature selection algorithms. The black dashed line highlights the classification accuracy after 200 features. (e) Accuracy matrix for patterned visual stimulation. (f) Average (\pm s.d.) classification accuracy of the combination of pairs of stimuli as a function of the centre-to-centre distance between visual stimuli.

In a first step, we conducted the classification on all the stimuli at once (10 locations and 60 repetitions for a total of 600 observations), resulting in an average (\pm s.d.) classification accuracy of $71.17\% \pm 1.83\%$ (10-classes classification). Then, to evaluate the impact of the distance (in degrees) between stimuli on the classification accuracy, we computed the classification accuracy between pairs of patterned visual stimuli (2-classes classification), resulting in 90 accuracy values, organised into an accuracy matrix (Figure 3-2e). All the values separated by the same distance were averaged and plotted as a function of the distance (Figure 3-2f). We observed an increase in the classification accuracy when the distance between stimulus locations increased. The classification accuracy started from 83.15%, which is higher than the chance level (50%), monotonously increased for the lowest separations, reached 96% for a separation of 5 degrees, and 100% for separation higher than 7 degrees. Visual stimuli are 14 degrees wide, so 100% classification accuracy was reached when the stimuli's overlap was reduced to 50%. This result suggested that the more the visual stimuli were separated, the less similar the VEPs are. In our hypothesis, as the patterned stimulations get further apart and gradually stop overlapping, they will recruit different populations of retinal ganglion cells, leading to the activation of increasingly different groups of neurons in V1. This activation ultimately results in a larger difference between the VEP signals, as they are an integrated summation of those neurons' activity.

While the algorithm could classify cortical patterns originating from visual stimuli in different locations with high accuracy, the classifier had one limitation. If giving as input to the classifier a novel signal from an

unknowing origin, it would only associate it with one of the classes of signals already encountered in its training phase, but it would not extrapolate the actual location of the stimulus eliciting that signal. This limitation motivated us to build a linear regression model to improve the predictive capacity when presented with a new signal of unknown origin, using the 200 features with the highest individual R2 scores. The average prediction of the model was close to the actual centre of the rectangles (Figure 3-3a), with an average (\pm s.d.) RMSE of 2.72 ± 0.60 degrees (Figure 3-3d), equivalent to 12.45% of the full range of possible positions. The adjusted R2 score of 0.86 suggested that the linear model is a good fit for patterned visual stimulation. The model performs better for the central locations, while the performance slightly decreases at the two extremities. To validate the model further, we performed two control experiments. First, we randomly scrambled the labels of the stimulus's centres (scrambled condition), and the linear regression model failed to predict the positions of the stimuli (Figure 3-3b), with an average (\pm s.d.) RMSE of 7.36 ± 2.85 degrees (Figure 3-3e). Second, we removed one location from the training set, and we trained on the 9 remaining locations. The testing set was composed only by the location that was left out from the training set (left-out condition). The linear regression model correctly predicted the missing stimulus position (Figure 3-3c), with an average (\pm s.d.) RMSE of 2.90 ± 0.96 degrees (Figure 3-3f).

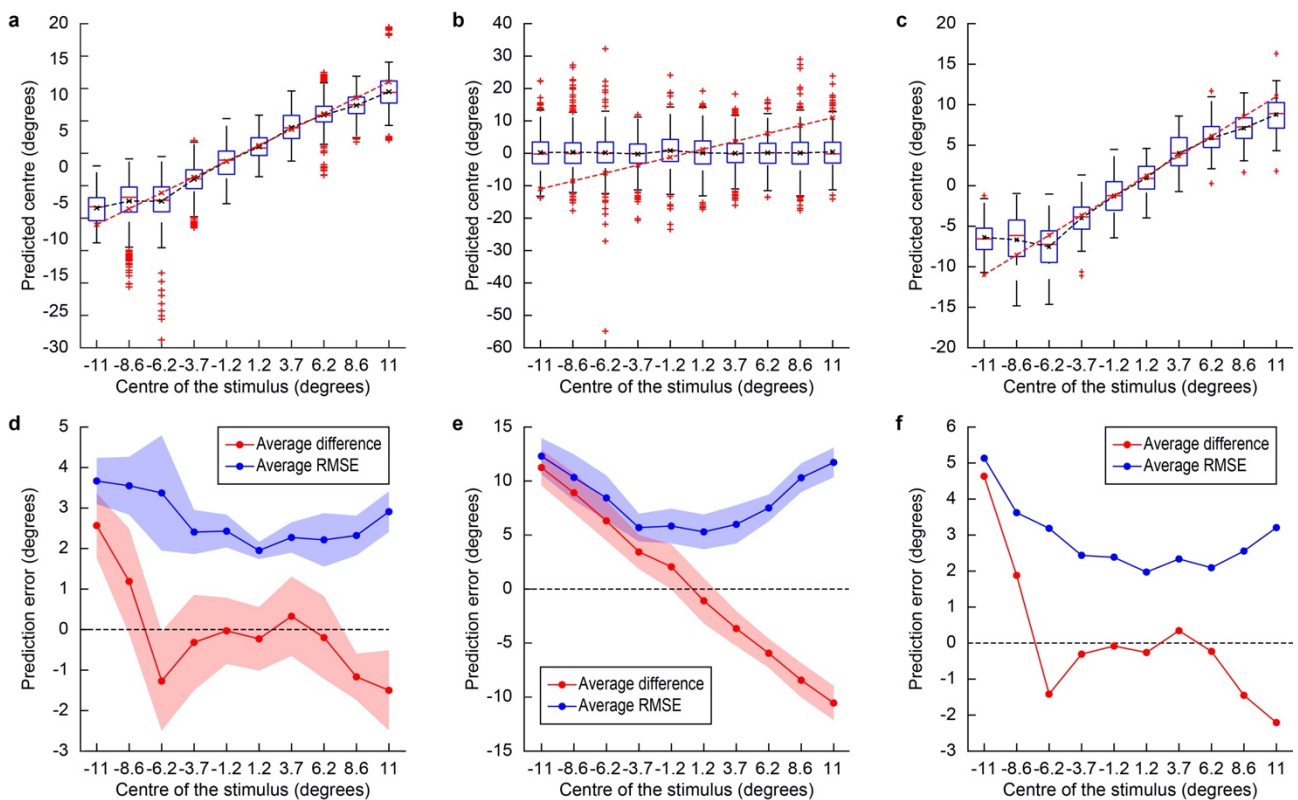


Figure 3-3. (a,b,c) Quantification of the averaged predicted centre locations (black dashed line) and their actual locations (red dashed line) for the three conditions: normal (a), scrambled (b) and left-out (c). In each box: the red line is the median, the box extremities are the 1st (q1) and 3rd (q3) quartiles, the whiskers are $q1 + 1.5 \times (q3 - q1)$ and $q3 + 1.5 \times (q3 - q1)$ and the red crosses outside of the whiskers are the outliers. (d,e,f) Average difference between the predicted and the actual locations (red) and RMSE of the predicted locations (blue) for the three conditions: normal (d), scrambled (e) and left-out (f). In panels (d,e) the shaded area is the s.d. In the left-out condition (f), the RMSE is computed only once for each excluded stimulus, so the s.d. cannot be computed.

3.4.2 Patterned electrical stimulation

We successfully designed a classification algorithm and a regression model for patterned visual stimulation. Next, we tested them on the optic nerve's intraneural electrical stimulation. First, we took advantage of a tailored OpticSELINE (Flat-OpticSELINE) with a linear and planar distribution of 8 electrodes transversally inserted from medial to lateral in the centre of the left optic nerve (Figure 3-4a). The advantage of this linear and flat electrode array is the similarity with the previously tested visual pattern: stimuli varying along a single dimension. Visual stimulation consisted of flashes aligned along the horizontal meridian from temporal to the nasal direction. With the Flat-OpticSELINE also electrical pulses are organised along the central line of the nerve's cross-section. A linear electrodes' distribution does not necessarily mean that phosphenes will occur along the horizontal meridian, since the fibres' retinotopic distribution within the nerve is unknown. However, the linear electrodes' distribution allowed us to compute the classification accuracy as a function of the distance and apply the linear regression model. Electrically evoked potentials (EEPs) were recorded upon biphasic charge-balanced asymmetric current pulses of different current amplitudes ranging from 10 to 2000 μA (Figure 3-4b).

First, we computed the activity maps for each stimulation electrode and each current amplitude (Figure 3-4c). From the maps, we computed the shift in both the leading channel (Figure 3-4d) and the average centre of mass (Figure 3-4e). At low current amplitudes ($\leq 250 \mu\text{A}$), both shifts appear random, but they became structured and reproducible from higher current amplitudes ($\geq 750 \mu\text{A}$). The quantification of the peak-to-peak amplitude from 750 μA revealed 2 to 5 leading channels out of the 8 stimulating electrodes depending on the current amplitude with a clear shift direction. Compared to the shift in VEPs, the direction is opposite, from posterior-lateral (electrode 1) to anterior-medial (electrode 8), which might be coherent with the insertion of the array from the medial to the lateral side of the nerve: electrode 1 is lateral, and electrode 8 is medial. Again, the limited spatial resolution of the recording system and analysis method provides only 2 to 5 hot-spots, which are not enough to identify distinguishable cortical activity patterns for each electrode. The distributions of the centre of mass for each activity map appeared more clustered and separated than the ones from VEPs (Figure 3-4e). Consequently, the shift of the average centre of the distributions from posterior-lateral (electrode 1) to anterior-medial (electrode 8) is larger than the one from VEPs. This larger shift and higher clustering could be justified since visual stimuli cover a small portion of the visual field, while electrodes spanned the entire optic nerve cross-section. We could hypothesise that electrodes induced phosphenes in region of the visual field which are more distant than the visual stimuli.

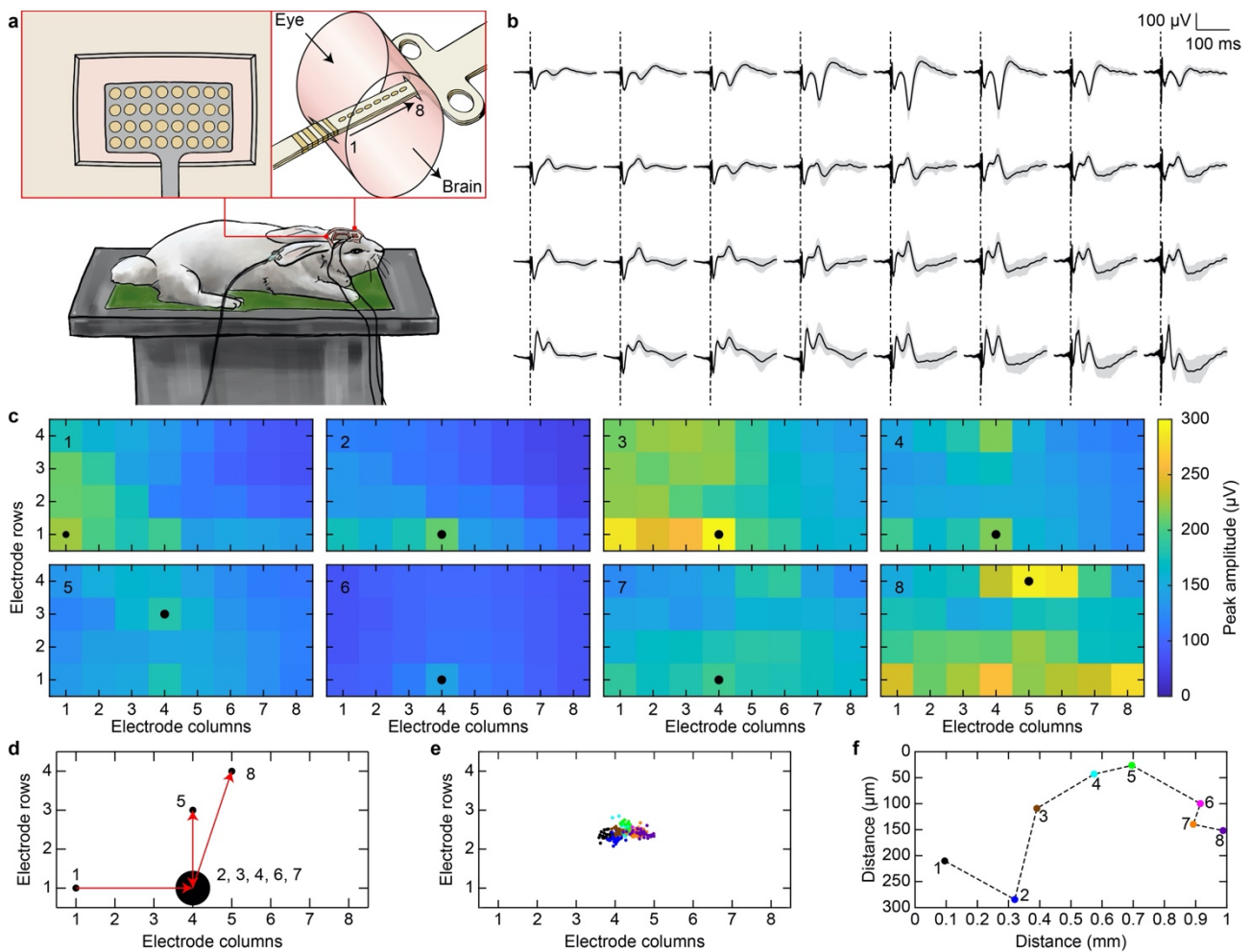


Figure 3-4. (a) Sketch of the experimental setup for electrical stimulation with the Flat-OpticSELINE. The red squares show an enlarged sketch of the ECoG recording electrode array placed over V1 and the Flat-OpticSELINE inserted into the left optic nerve from medial to lateral. The electrode's arrangement is indicated by the black arrow from 1 to 8. (b) Representative example of the 32 EEPs recorded with the ECoG electrode array upon one electric pulse (2000 μ A). The black trace is the average of 30 repetitions, while the s.d. is the grey area. The black dashed lines are the stimulus onset. (c) Averaged activity maps among the 30 repetitions obtained for each electrode upon electrical stimulation at 2000 μ A. In each map, the number in the upper left corner indicates the electrode, while the black circle indicates the leading channel. (d) Map of the channels identified as leading channels upon electrical stimulation at 2000 μ A. The black circles' size is proportional to the number of times the electrode is identified as the leading channel. The numbers next to the circles correspond to the stimulation electrodes leading to the recording electrode being identified as the leading channel. The red arrows identify the shift of the leading channel. (e) Distributions of the centres of the activity map upon electrical stimulation at 2000 μ A. Each circle corresponds to a single activity map upon one electric stimulus (30 circles for each electrode). Each colour corresponds to one stimulus location as in (f). (f) Shifts of the average centre of the activity map upon electrical stimulation at 2000 μ A. Each circle is the average of the centres originating from one electrode. The numbers correspond to the electrode associated to a colour code.

For EEPs, we implemented the same classification workflow used for VEPs with the machine-learning algorithm. The features used and the feature selection method remained unchanged (Figure 3-5a-c), but due to the lower number of repetitions (30 instead of 60), we selected only the 100 best scoring features to avoid overfitting using the MRMR algorithm (Figure 3-5d,e). In a first step, we conducted the classification on all the stimuli at once (8-classes classification) for each current amplitude: 8 electrodes and 30 repetitions for a total of 240 observations (Figure 3-5f, black). The classification accuracy started around 20% for low current amplitudes (from 10 to 75 μ A), slightly above the chance level (12.5% for 8 electrodes). This low correlation accuracy is justified since those current amplitudes correspond to the threshold to elicit a detectable EEP. The correlation accuracy linearly increased by increasing the current amplitude and reached nearly 100%

from 500 μA . As a control experiment, the observations' labels were scrambled before the classification, and the classification accuracy remained rightfully close to chance level regardless of the current amplitude (Figure 3-5f, blue). Overall, the machine-learning algorithm correctly classified cortical activity patterns based on the electrode in the array from which they were evoked in the entire range of current amplitudes above the activation threshold for EEP. Then, to evaluate the impact of the separation between electrodes on the classification accuracy of the elicited cortical activations, we computed the classification accuracy between pairs of electrodes (2-classes classification), resulting in 56 accuracy values organised into an accuracy matrix for each current amplitude (Figure 3-5g). All the values separated by the same distance were averaged and plotted as a function of the distance (Figure 3-5h). The classification accuracy with the machine-learning algorithm returned an increasing classification accuracy as a function of the electrode distance. The increase was marked for intermediate current amplitudes (200 and 250 μA), while at higher current amplitudes, the accuracy was quickly reaching 100%. For lower current amplitudes (below 150 μA), we could not find a clear relation between classification accuracy and electrode separation, probably because of the very low cortical activity elicited by such low currents.

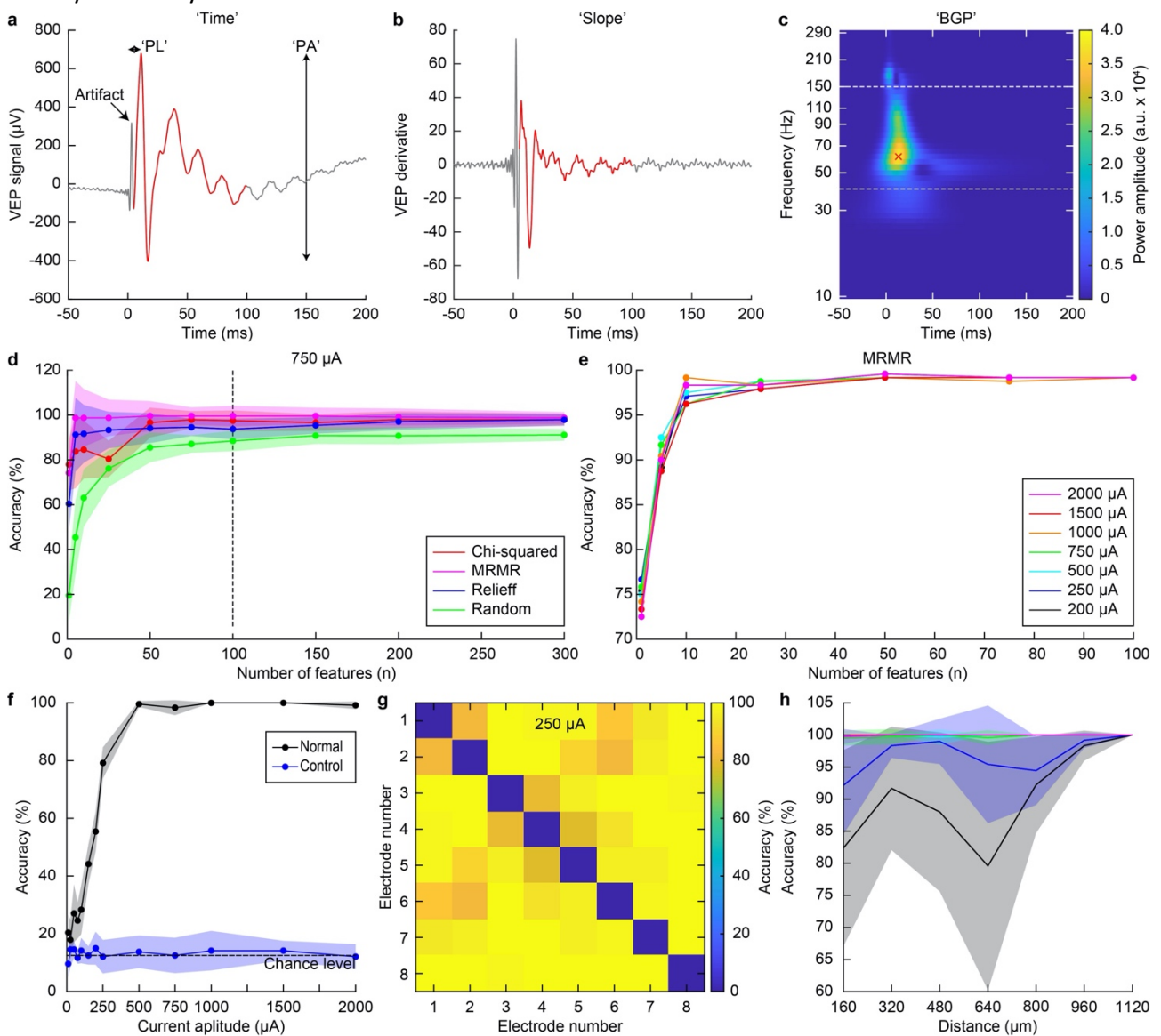


Figure 3-5. (a) Representative EEP signal highlighting the peak-to-peak amplitude and the latency of the positive peak. The red portion of the signal corresponds to the time course used as features from 5 ms to 100 ms. (b) Derivative of the EEP signal in a. The red

portion of the signal is the one used as features from 5 ms to 100 ms. **(c)** Representative spectrogram from the EEP signal in a. The white dashed lines indicate the frequency band corresponding to the 'BGP'. The red cross highlights the 'Power Amplitude', the 'Power Frequency' and the 'Power Timing'. **(d)** Average (\pm s.d., 6 repetitions) classification accuracy of the feature selection algorithms for a stimulation current amplitude of 750 μ A. The dotted line highlights the classification accuracy after 100 features. **(e)** Average (6 repetitions) classification accuracy of the MRMR feature selection algorithm for the stimulation current amplitudes from 200 μ A to 2,000 μ A. **(f)** Average (\pm s.d.) classification accuracy as a function of the stimulation current amplitude of all the electrodes (black). The blue circles and line show the classification accuracy when labels of the observations were scrambled. **(g)** Accuracy matrix for the optic nerve's intraneural electrical stimulation at 250 μ A. **(h)** Average (\pm s.d.) classification accuracy of the combination of electrodes' pairs as a function of the centre-to-centre distance at increasing current amplitudes (from 200 to 2,000 μ A) for the optic nerve's intraneural electrical stimulation. Colour code is as in panel e.

Next, we fitted the linear regression model on the features extracted from the EEPs (Figure 3-6), following the same method used for patterned visual stimulation but using only the 100 features with the highest individual R2 scores. The model had the best fit for 1,000 μ A (Figure 3-6a and b) according to the adjusted R2 (0.91) and the average RMSE (0.68). Overall, among the various current amplitudes, the model had an adjusted R2 between 0.01 and 0.91, increasing with the current amplitude and an average RMSE between 3.24 and 0.65, decreasing with the current amplitude (Figure 3-6c). To validate the model further, we performed control experiments as done for VEPs. First, we randomly scrambled the labels of the stimulating electrodes (scrambled condition), and the linear regression model failed to predict the electrode's position (Figure 3-6d), with an average (\pm s.d.) RMSE of 2.66 ± 0.69 (Figure 3-6e). A similar behaviour was observed for all the current amplitudes (Figure 3-6f). Second, we removed one stimulating electrode from the training set, and we trained on the 7 remaining electrodes. The testing set was composed only of the electrode left out from the training set (left-out condition). The linear regression model correctly predicted the missing electrode position (Figure 3-6g), with an average (\pm s.d.) RMSE of 1.06 ± 0.74 (Figure 3-6h). Overall, among the various current amplitudes, the model had an average RMSE between 4.06 and 1.06, decreasing with the current amplitude (Figure 3-6i).

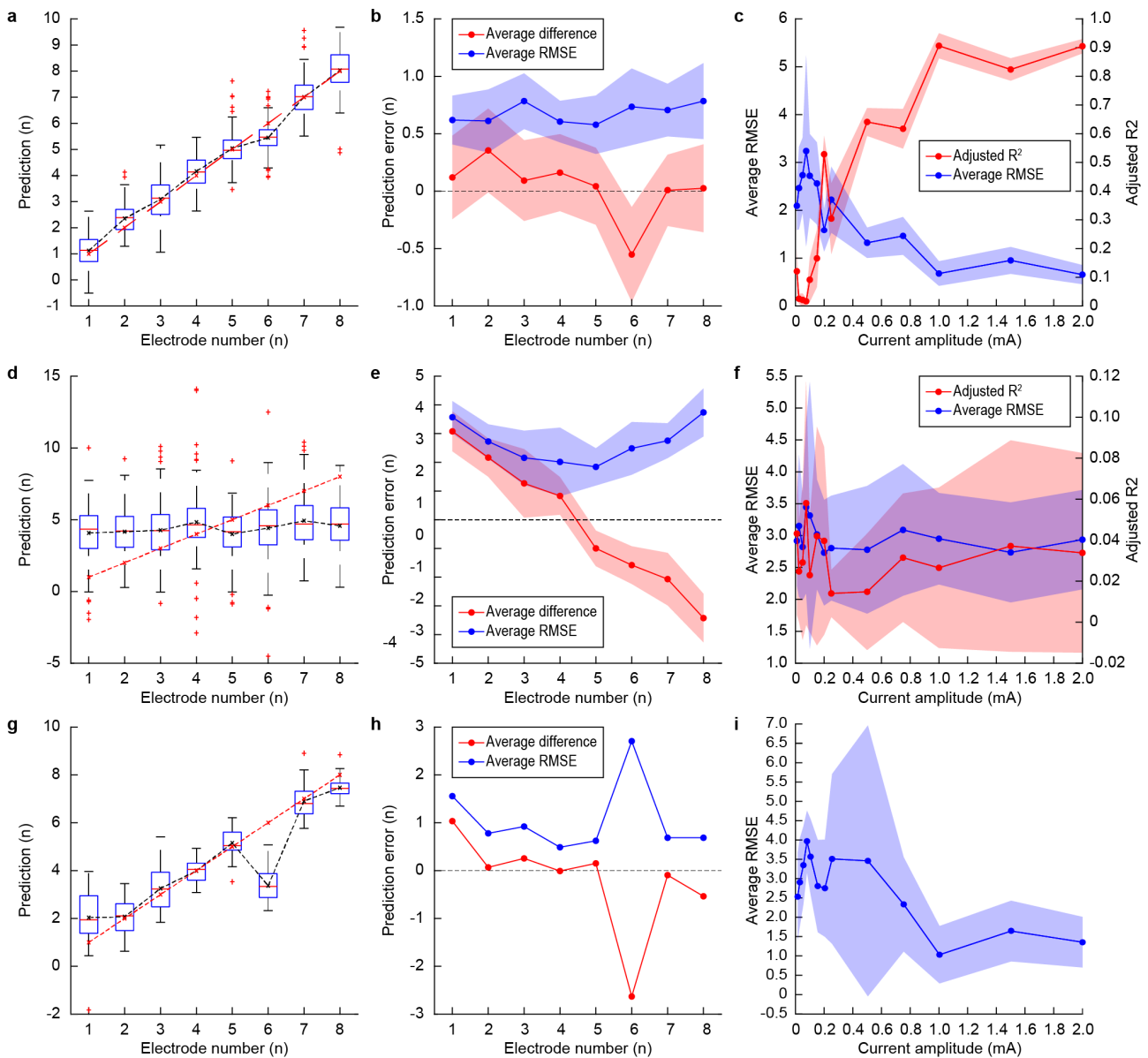


Figure 3-6. (a,d,g) Quantification of the averaged predicted centre locations (black dashed line) and their actual locations (red dashed line) upon electrical stimulation at 1,000 μ A for the three conditions: normal (a), scrambled (d) and left-out (g). In each box: the red line is the median, the box extremities are the 1st (q1) and 3rd (q3) quartiles, the whiskers are $q1 + 1.5 \times (q3 - q1)$ and $q3 + 1.5 \times (q3 - q1)$ and the red crosses outside of the whiskers are the outliers. (b,e,h) Average difference between the predicted and the actual locations (red) and RMSE of the predicted locations (blue) upon electrical stimulation at 1,000 μ A for the three conditions: normal (b), scrambled (e) and left-out (h). In panels (b,e) the shaded area is the s.d. In the left-out condition (h), the RMSE is computed only once for each excluded stimulus, so the standard deviation cannot be computed. (c,f,i) Average (\pm s.d.) RMSE (blue) and adjusted R2 coefficient (red) of the model as a function of the stimulating current amplitudes for the three conditions: normal (c), scrambled (f) and left-out (i). In the left-out condition (i), the adjusted R2 coefficient cannot be computed since it requires the variance of the testing set labels, which is null since the testing set is only composed of observations with the same label.

Our approach used nine classes of features from both the time domain and the frequency domain classified in two major categories: punctual and continuous. Therefore, we investigated which feature's types was most informative. We repeated the linear regression model for both patterned visual stimulation and patterned electrical stimulation. We computed the correlation coefficient between the features and the stimuli' locations based on the whole datasets to be more descriptive (i.e. on the total number of observations instead of the 5/6th of the training sets' observations). Then, we selected the 200 (for patterned visual stimulation) and 100 (for patterned electrical stimulation) features with the highest correlation coefficient value (Figure

3-7). For patterned visual stimulation, the 200 selected features were from only two types: ‘Slope’ (51.5%) and ‘Power’ (48.5%), both continuous features. This result indicates that continuous features might be more informative than punctual features, like the peak-to-peak amplitude. Patterned electrical stimulation revealed a remarkably similar behaviour. Among all the current amplitudes, 6 types of features were cumulatively selected: ‘Time’ (8.5%), ‘Slope’ (12.5%), ‘Power Timing’ (0.2%), ‘Power Amplitude’ (0.2%), ‘BGP’ (19.2%) and ‘Power’ (59.4%). Continuous features (99.6%) were largely predominant compared to punctual features (0.4%). Features in the frequency domain were mostly selected (79%) compared to features in the time domain (21%). The most informative feature was the ‘Power’ feature (59.4%).

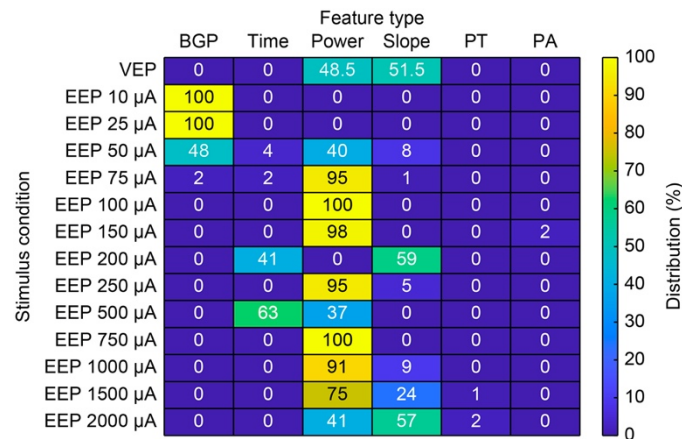


Figure 3-7. Distribution of the selected feature’s types. Numbers in each box correspond to the exact percentage value. PT corresponds to ‘Power Timing’ and PA to ‘Power Amplitude’.

The machine-learning algorithm returned an excellent classification accuracy for intraneural electrical stimulation with the Flat-OpticSELINE. Therefore, we generalised the approach and used the method to classify EEPs originating from the standard OpticSELINE having flaps distributing electrodes over the nerve’s cross-section. For this classification, we used a dataset obtained from previous experiments³³⁶. Briefly, the optic nerves of four rabbits were implanted with the OpticSELINE, and the six electrodes of the top shank were used for electrical stimulation. EEPs were collected with the same ECoG arrays (Figure 3-8a). For each of the four rabbits, we classified the time courses of the EEPs originating from the optic nerve’s stimulation using the six electrodes of the upper part of the OpticSELINE as a function of the current amplitude (Figure 3-8b). We conducted the classification on all the stimuli at once for each current amplitude: 6 electrodes and 10 repetitions for a total of 60 observations. The machine-learning algorithm showed a very high classification accuracy for three rabbits, close to 100% from 200 µA. In one rabbit (bottom left panel in Figure 3-8b), the classification accuracy was increasing with a slower slope, probably because higher currents were required to elicit detectable EEPs and the signal-to-noise ratio of the cortical responses was low. The average accuracy among the four rabbits started around 20% for low current amplitudes (10 and 25 µA), which is slightly above the chance level (16.6% for 6 electrodes). Then, the classification accuracy rapidly increased until reaching a plateau at 100% for the higher current amplitudes (Figure 3-8c).

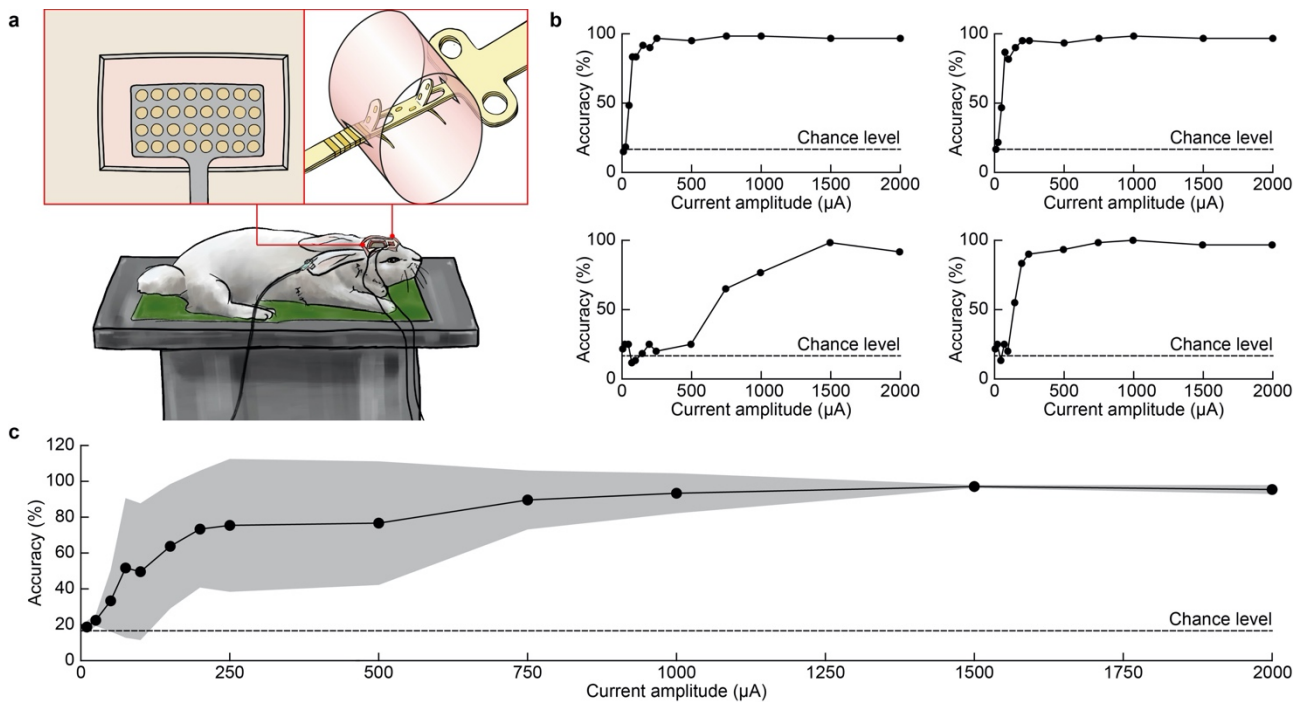


Figure 3-8. (a) Sketch of the experimental setup for electrical stimulation with the OpticSELINE. The red squares show an enlarged sketch of the ECoG recording electrode array placed over V1 and the OpticSELINE. (b) Individual classification accuracy as a function of the stimulating current for each rabbit. (c) Mean (\pm s.d.; $n = 4$) classification accuracy as a function of the current amplitude.

3.5 Discussion

Optic nerve stimulation has advantages compared to epiretinal stimulation. However, one of the key open questions in preclinical studies is to detect distinguishable cortical patterns upon selective activation of the nerve fibres. Computational and experimental methods showed that intraneural electrodes could selectively activate different sets of fibres within the optic nerve³³⁶. Also, high-frequency pulse trains with a variable number of pulses could modulate the cortical responsivity without affecting the optic nerve's activated area. Building on this evidence, our results showed that a machine-learning algorithm could correctly classify electrically evoked cortical potentials originating from the microelectrodes of the OpticSELINE array.

First, we showed that approaches relying only on the peak-to-peak amplitude alone are not powerful enough to distinguish the stimulus's location inducing the cortical activation due to the low spatial resolution of ECoG microelectrodes. This result motivated the development of a new signal analysis approach based on a SVM classification algorithm, and we took advantage of patterned visual stimulation for its validation. We designed the stimulation pattern to test conditions in which the visual field's stimulated portions are close and overlapping, thus more difficult to distinguish from one another. We hypothesised that the further apart the visual field's stimulated portion would be, the less similar the signal originating from their activation would be. Therefore, the visual stimuli were aligned over the horizontal meridian to precisely quantify their centre-to-centre separation. The SVM classification method confirmed the hypothesis, showing an increase in classification accuracy with increased centre-to-centre separation, reaching 100% for stimuli with less than 50% overlap.

After demonstrating the efficiency of the SVM classification approach on patterned visual stimulation, we tested it on the optic nerve's intraneural electrical stimulation. First, we used a simplified intraneural electrode array (Flat-OpticSELINE). As for visual stimulation, we found an increase in classification accuracy with

increased centre-to-centre separation between the stimulating electrodes. However, the performance of the SVM classification method was much better for electrical stimulation than visual stimulation, with nearly 100% classification accuracy from the smallest separation distance above 500 μA . This result also highlighted the dependence of the classification accuracy from the current amplitude, with higher accuracy at higher amplitudes. This result could be explained since the highest is the current amplitude, the highest is the signal-to-noise ratio of the recorded signal and the lowest is the variability among trial, leading to better classification. Also, the better performance on electrical stimulation can be explained since the visual stimuli cover a small portion of the visual field, while electrodes spanned the entire optic nerve. We could hypothesise that electrodes induced phosphenes in region of the visual field which are more distant than the visual stimuli. Because of this difference, a quantitative comparison between visual and electrical stimulation could not be performed. However, both modalities showed the same qualitative behaviour.

The algorithm provided only a qualitative estimation of the distance separating two stimuli: a low accuracy score was associated with a small distance between the stimuli, while a high accuracy score indicated that the stimuli were further apart. However, it cannot predict how far apart the stimuli were since after a small distance between the electrodes, the classification accuracy reached a plateau at 100% of accuracy, and increasing the distance between stimuli further could not improve it. Also, for electrical stimulation above 500 μA , the classification accuracy reached 100% from the smallest separation distance. Therefore, we applied a regression model to add a predictive capacity. We selected a linear model as it is a simple approach matching the type of stimuli used, which vary along a single dimension. This choice relies on the assumption that some features are linearly related to the stimuli's coordinates. We obtained several features with a large correlation coefficient, which allowed us to build a successful regression model for both visual and electrical patterned stimulation. The linear regression model performed better for patterned visual stimulation than patterned electrical stimulation, as visible from the RMSE in the left-out condition. The linear regression is a better approximation in patterned visual stimulation because stimuli remained located in a small and central portion of the visual field. This approximation of linearity is less accurate for patterned electrical stimulation since electrodes are located through the whole size of the optic nerve, and the evoked phosphenes might not be all linearly organised. In this condition, a more complex machine-learning algorithm such as convolutional neural networks could provide better results since it would not impose any assumption on linearity or any other type of regression.

The linear regression models for both patterned visual and electrical stimulation revealed that continuous features are the most informative. Punctual features appeared only sporadically in patterned electrical stimulation and resulted in not being very informative. Punctual features compress the cortical signal into a single value, which does not appear to be informative enough for prediction models. Features from both time and frequency domains were selected. However, spectral features appeared to be the most robust, especially the 'Power' feature. Among features in the time domain, 'Slope' was the most selected. It is noteworthy that the signal's derivative ('Slope') was mostly selected and not the signal itself ('Time'). This result might be explained by the trial-to-trial variation of the signal (e.g. voltage offset), which is removed in the derivative, making the 'Slope' more consistent between repetitions. Among features in the frequency domain, it appears that the 'Power' feature is the most informative. BGP or similar frequency ranges have been used to successfully classify cortical signals in V1 upon visual stimulation³³⁸ and electrical stimulation of the retina³⁴¹. From this dataset and results, the whole spectrum ('Power' feature) is more informative than its partition ('BGP'). The BGP might result in a loss of information compared to the whole spectrum.

The successful design of these two algorithms shows that the cortical activities elicited by the electrical stimulation are indeed distinctively different. The linear regression model then shows that they are meaningfully different, as it highlights features that vary in a linear manner, which can be expected from cortical activity patterns resulting from the stimulation of a gradually shifted portion of the visual field.

To generalise the approach, we implemented the SVM classification algorithm to EEPs induced by the OpticSELINE intraneural array, where the electrodes are not distributed in line but cover the cross-section of the nerve. The algorithm returned similar results, with a nearly 100% classification accuracy above 200 μA of current stimulation in three out of the four rabbits tested. In one animal, the classification accuracy increased with a slower slope as a function of the current. This result was explained since, in that experiment, higher currents were required to elicit detectable EEPs, and the signal-to-noise ratio of the cortical responses was low. The classification accuracy's dependency with the signal-to-noise ratio makes the classification algorithm relative to the stimulation strength. Thus, an increase in classification accuracy could be linked to a larger separation between the stimuli only when the stimuli are comparable in strength: that is to say, the same illuminated surface for visual stimuli or the same current amplitude for electrical stimulation.

3.6 Conclusion

The machine-learning approach based on an SVM classification algorithm showed that the cortical activity patterns induced by the optic nerve's intraneural stimulation with the OpticSELINE could be successfully classified. Like patterned visual stimulation, intraneural electrodes might selectively recruit different optic nerve portions leading to different visual phosphenes. This result is a critical step to move forward visual prosthesis based on the optic nerve's intraneural stimulation. However, it must be noted that this analysis and results cannot provide information about perceptual phenomena. Also, in late-stage retinitis pigmentosa patients, only 30% of retinal ganglion cells might be spared, and the retina's hyperexcitability might affect the reliability of artificial vision via optic nerve's stimulation. These assessments will require further clinical investigation.

3.7 Acknowledgment

This work was supported by École polytechnique fédérale de Lausanne, Medtronic and Swiss National Science Foundation (200021_182670).

Chapter 4 Conclusion

4.1 Achieved results

The present thesis focuses on investigating electrical stimulation of the optic nerve stimulation for artificial vision. In the second chapter, we introduced a new intraneural multi-electrode array design, called the OpticSELINE. To our knowledge, it is the first flexible intraneural array to ever be proposed for the electrical stimulation of the optic nerve. We conducted the electrical and mechanical characterization of the implant, demonstrating its solid anchorage stability, an important property lacking in the previously used implant in optic nerve stimulation and necessary to be able to elicit phosphenes with a consistent location in the visual field in chronic implantation conditions. We then optimized the electrical stimulation pulse width and found an optimal pulse duration of 150 μs for the leading cathodic phase, with an amplitude/duration ratio of 5 for the counterbalancing pulse. This brings the total duration of the pulse just under 1 ms, which permits using high stimulation frequencies that permit large flexibility in the stimulation. Indeed, this enables to stimulate both asynchronously or synchronously through several electrodes, depending on the types of activation desired. The former ensures to avoid cross-talk between too close neighboring electrodes and that each of them activates only nervous fibers in their close vicinity, while the latter condition could result in a summation of the two produced negative potential field, leading to an additional activation of the area in between the two electrodes that may be undesired.

This was followed by the demonstration of the possibility to modulate the magnitude of the cortical activation by changing the stimulating current amplitude. According to the simulation study we conducted, this is caused by a proportional change in the number of fibers activated by the stimulation. The ability to control the size of the activated portion of the nerve will likely prove to be very useful in adding flexibility to the image reconstruction algorithm. Indeed, due to anatomical constraints, optic nerve prostheses will likely lack the high-density distribution of electrodes present in retinal implants. Therefore, unlike their image reconstruction algorithms which can mostly be limited to the pixelization of the image, optic nerve prostheses will likely need to use a combination of phosphenes of various sizes and shapes to achieve higher fidelity artificial image reconstruction in blind patients.

Since the rabbit primary visual cortex is organized in a retinotopic manner, we initially expected to be able to see visible spatial shifts in the maximally activated portion of the visual cortex when a different portion of the optic nerve or the visual field are stimulated. This hypothesis was discarded in the second chapter, as at the time, it seemed there was no coherent and spatially segregated focalized cortical activation pattern resulting from the electrical stimulation. However, it was recently discovered that due to a different numbering between the channels of the ECoG array and its connector linking it to the stimulator, the spatial arrangement of the channel was incorrect, which resulted in scrambled cortical maps. This presumed absence of a shift in the cortical activity led us to seek out alternative approaches to evaluate the selectivity of the OpticSELINE. We used ICA in order to obtain independent components that are a linear combination of the 32 originally recorded ECoG signals. We used a classification algorithm that allowed us to discard the ICs corresponding to noise or artifact. We then demonstrated that some of the remaining ICs were exclusively related to a single stimulating electrode. This shows that some components of the signal originating from the stimulation through different electrodes are meaningfully distinctive, suggesting that our electrical stimulation indeed stimulates different portions of the nerve.

In the third chapter, we developed two machine learning algorithms, a classifier based on an SMV algorithm and a linear regression model based on a wide variety of features, instead of the commonly used P1 peak extracted from the ECoG signal traces. The successful design of these two algorithms further demonstrates that the cortical activities elicited by the electrical stimulation are indeed distinctively different. The linear regression model then shows that they are meaningfully different, as it highlights features that vary in a linear manner, which can be expected from cortical activity patterns that result from the stimulation of a gradually shifted portion of the visual field.

The choice of the employed features is also significant as it highlights that features such as the slope and the power spectrum of the ECoG signal are better than the previously described P1 peak for the prediction of the location of the stimuli that elicited said signal, which was unknown before this study.

Developing algorithms that automatically detect small changes in the cortical signal, such as the regression model of the patterned stimulation condition, will be crucial in the evaluation of new optic nerve implant prototypes and the aforementioned elaborate image reconstruction algorithms they likely will use. Furthermore, such algorithms could have additional applications, such as being involved in a later stage in the—at least partial—automatization of the calibration of the optic nerve prosthesis in patients. This is desirable as one may expect this process to involve the optimization of a large number of stimulation parameters, which may prove to be too time-consuming and strenuous for the patient to be conducted fully manually by pointing to the location and outline the shape of each phosphene elicited by the different combinations of stimulation parameters.

4.2 Future developments

This thesis has been focussed on the demonstration of the feasibility of using intraneural electrical stimulation of the evoking distinctly cortical activation patterns. After having successfully demonstrated it, several improvements related to the experimental setup, data analysis protocols, and design of the implant can be considered.

4.2.1 Mapping of the optic nerve

The body of knowledge on the rabbit's visual system is mostly concentrated on the physiology and the organization of its retina and its primary visual cortex, but it is relatively sparse concerning its optic nerve. One can assume that rabbits have a different internal organization of the optic nerve than primates since their eyes have a visual streak instead of a fovea. This would possibly result in an only vertically magnified representation of the optic nerve's visual streak, as can be expected since the visual streak is already known to be magnified in a similar fashion in V1, but this is purely speculative¹⁰². Answering this question and generally aiming to obtain a better understanding of the rabbit visual system appears like one of the first priorities at this stage of the development of this project. Indeed, having a retinotopic mapping of the organization of the axonal fibers of the optic nerve paired with the optic nerve model would allow us to better estimate what types of cortical patterns of activation we can expect our electrical stimulation protocols to elicit, which seems crucial to help us better interpret our results.

This could be achieved by several approaches; a first approach could consist of the topical application of dyes on tiny portions of the rabbit's retina, followed by the imaging of the histological slices of the fixed optic nerve, which would allow the distinction of the axons corresponding to the stained portion of the retina. An

alternative approach could consist of the recording of the neural activity in the nerve while the rabbit has been presented with visual patterns similar to the one used in chapter 3 of the thesis, but here spread over the whole visual field instead of only its central portion. An array of penetrating electrodes could be used in order to pair the portion of the visual field being stimulated with the portion of the optic nerve with the highest compound action potential. Alternatively, electrical impedance tomography, an imaging technique that detects transient impedance changes in the neural tissue caused by the opening of ionic channels during the propagation of action potentials, could be used to image the activated portion of the optic nerve that corresponds to the portion of the visual field that is stimulated.

Optimally, such mapping of each pair of coordinates of the cross-section to a pair of coordinates of the visual field should be obtained for each position along the length of the optic nerve, which could be used to determine implantation location along the optic nerve that would give rise to the optimally discriminable cortical pattern, and could further prove to be useful in the future if we were to use stimulation sites that are not limited to a fixed cross-section plane of the nerve but could be spread at different locations amongst the nerve length.

4.2.2 Assessment of the OpticSELINE position inside the optic nerve

The OpticSELINE is assumed to be implanted horizontally through the central portion of the nerve, but knowledge of its precise position inside the nerve is currently missing. The surgical implantation is conducted in a tiny opening in the brain and without clear anatomical landmarks indicating the nerve orientation. In such conditions, it is fair to assume an important degree of variation in the OpticSELINE's implantation orientation and position, as well as in the degree of its wing, which could greatly modify the portions of the nerve being activated by the stimulation.

The retinotopic mapping of the optic nerve alone is not enough in order to better estimate the expected cortical activation patterns elicited by our electrical stimulation if it is not paired with the knowledge of the exact position of the OpticSELINE inside the nerve and the angles of the opening of its wing. Therefore, investigating approaches that would allow assessing these implantation parameters appears like a second useful step to better predict what portion of the nerve is being activated, and consequently, what resulting cortical activation patterns that one should expect. This could be achieved by using a high-resolution CT-scan to image the position of the electrode inside the explanted nerve.

4.2.3 Assessment of the ECoG array electrodes RFs

In chapter 3, even for the furthest apart visual stimulation patterns, which are approximately 11 degrees apart and non-overlapping, there was no visible shift in the almost identical cortical maps (with a correlation coefficient of 97%). This could be explained by the fact that the ECoG electrodes could have a broad RF; they could detect cortical activity originating from the presentation of visual stimuli over a very large portion of the visual field). This would be coherent with the fact that ECoG electrodes are known to integrate neural signals originating from a quite large volume of the cortex. If that would prove to be the case, the two furthest apart visual stimulation patterns could still be too close from one another, and therefore both of them would fall in the same region the ECoG electrodes RFs, resulting in the observed very similar cortical maps. This could be verified in parallel in a similar fashion as the internal mapping of the optic nerve; white rectangle visual stimuli (or other visual patterns such as Gabor stimuli) could be presented at

different coordinates spanning the whole visual field while recording the resulting visual activity. This would allow delimiting the outline of the ECoG electrodes RFs as described in more detailed Dubay and Ray, 2019³³⁷.

While spatial shifts of the cortical activity are not visible in patterned visual stimulation, it seems there could be one in electrical stimulation with the flat OpticSELINE (chapter 3), as evidenced by the cortical maps and shift of their centroid, and according to the preliminary corrected cortical maps obtained from data originating from the stimulation with a standard (with open wings) OpticSELINE (Figure 4-1a-e). Conducting such RF mapping prior to a recording could allow us to approximately associate the spatial location of the cortical activation with the portion of the optic nerve that is stimulated.

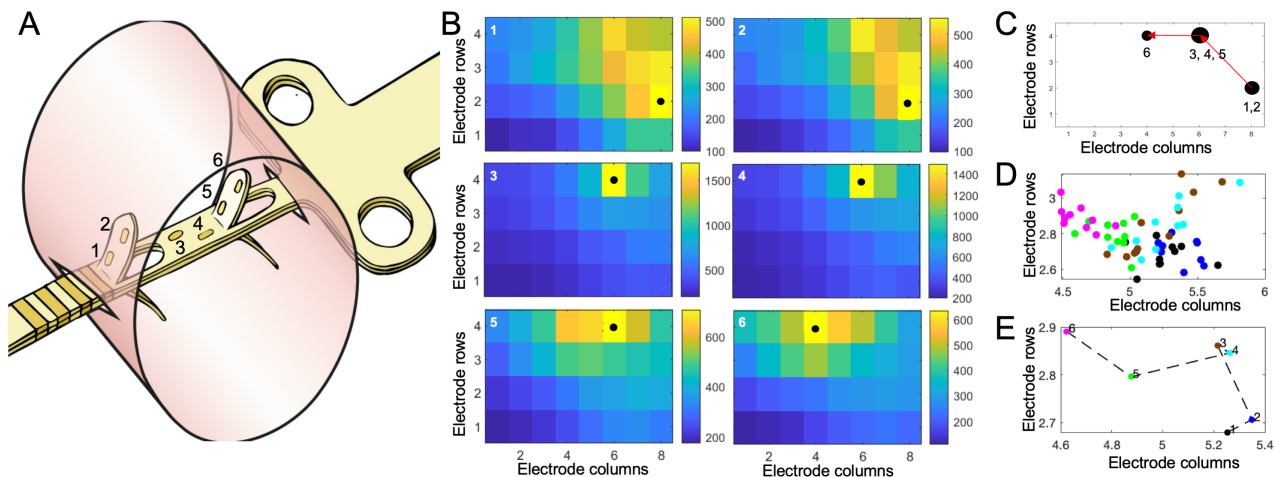


Figure 4-1 | Representative shift of the cortical activity in normal OpticSELINE stimulation. (a) Sketch of the OpticSELINE inserted into the left optic nerve from medial to lateral, with the electrode numbers indicated. (b) Averaged activity maps among the 30 repetitions obtained for each electrode upon electrical stimulation at $750 \mu\text{A}$. In each map, the number in the upper left corner indicates the electrode, while the black circle indicates the leading channel. (c) Map of the channels identified as leading channels upon electrical stimulation at $750 \mu\text{A}$. The black circles' size is proportional to the number of times the electrode is identified as the leading channel. The numbers next to the circles correspond to the stimulation electrodes leading to the recording electrode being identified as the leading channel. The red arrows identify the shift of the leading channel. (d) Distributions of the centres of the activity map upon electrical stimulation at $750 \mu\text{A}$. Each circle corresponds to a single activity map upon one electric stimulus (30 circles for each electrode). Each colour corresponds to one stimulus location as in (e). (e) Shifts of the average centre of the activity map upon electrical stimulation at $750 \mu\text{A}$. Each circle is the average of the centres originating from one electrode. The numbers correspond to the electrode associated with a colour code.

4.2.4 Alternative cortical activity recording methods

It appears that the cortical activity is spread over a large portion of the ECoG array, while the shift in the peak activity often appears to be only a fraction of this spread, making it likely that the ECoG array is only able to detect very large changes in the activated portion of the optic nerve. Multi-unit activity recorded by a penetrating microelectrode array is known to be a more local signal, so replacing the ECoG array with such type of array could potentially allow us to detect finer changes in the cortical activation pattern, which is desirable since the number of stimulating sites of the implant will be increased in the future, resulting in closer electrodes and therefore less easily distinguishable cortical activation patterns³³⁷. A more drastic change of the recording device could consist of recording the resulted neural activity elicited by the electrical stimulation from the nerve itself instead of from the cortex, which would potentially allow us to obtain a more direct and precise quantification of the activation taking place in the optic nerve. Additionally, this could provide useful information to confirm or disconfirm the validity of certain assumption made in the hybrid model, such as the fact that the optic nerve volume in the model is made out only of axons, while in

reality, the optic nerve also contains connective tissue that may impair the propagation of the current inside the nerve, and therefore help to make the model more realistic overall.

While the optic nerve itself is too short to allow the implantation of both a stimulating and recording device, this could be done by recording the neural activity from the optic tract instead, taking advantage that each optic tract is made out of 90% or more axons originating from the contralateral optic nerve. Accessing and implanting both the optic nerve and the more caudally located optic tract may prove to be surgically challenging, making it advantageous to conduct the recording on an explanted eye, optic nerve, and optic tract, with the two latter maintained in a nutrient solution, and the latter in a separate compartment filled with oil for recording. The choice of recording device is up for debate, but the aforementioned EIT imaging technique could prove to be an attractive choice, as it was showed to be able to image single fascicular activity in the upper portion of the rat's sciatic nerve, which has a similar diameter as the rabbit's optic nerve, following the electrical stimulation of the already separated fascicules of the nerve. This requires the prior knowledge of the retinotopic organization of the rabbit's optic tract, which can be obtained in the same manner as the optic nerve's one.

4.2.5 Machine learning algorithm improvement

The regression model and classifier both use features that are extracted individually from the signal of each ECoG electrode which is treated independently and therefore not explicitly related to the spatial location of the cortical activity. As evidenced by the noticeable shift in the centroid location of the electrical stimulation cortical maps, it appears that the addition of features related to the spatial location of the highest cortical activity, such as the horizontal and vertical coordinates of the centroid of the cortical map for instance, or some more elaborate feature, could complement the already selected types of feature and possibly improve the performances of both algorithms.

While the linear regression appears to be an appropriate approximation in the patterned condition due to the close proximity of the visual stimuli that remain located in a small and central portion of the visual field, this approximation seems less appropriate for the electrical stimulation where the stimulation sites are located through the whole width of the optic nerve. This is supported by the higher error in the excluded electrode stimulation control condition, suggesting that the model is less robust and can less easily classify data that were not used for its training. We selected this regression model for its simplicity and its ease of use, and while it still proved very satisfactory, replacing it with a more complex machine-learning algorithm such as convolutional neural networks that would not impose linearity could potentially represent a more fitting choice of model, especially for the electrical stimulation condition.

4.2.6 Animal model

The rabbit is an attractive animal model as its housing is relatively inexpensive. However, its visual system is significantly different from human's one both in terms of dimensions and organization, which will ultimately limit its usefulness to test more advanced optic nerve implants.

Moving to a non-human primate animal model will eventually be a second essential step toward bringing optic nerve stimulation for artificial vision toward the clinic. Monkeys are an attractive animal model for several reasons; their similarity in their optic nerve organization, such as the magnification of the center of the visual field, would make an implant optimized for the monkey optic nerve much more easily translated to human than one optimized for a rabbit optic nerve. Secondly, their visual cortex is larger than the one of

rabbits, making it easier to discriminate which portion of it is being activated by a particular stimulation of the optic nerve. Finally, monkeys can be trained on behavior tasks, such as pointing to the location of a light spot appearing in their visual field. They will continue conducting the task upon the appearance of a phosphene instead of an actual real light spot, and therefore can be effectively trained to reveal key information about the hypothetical phosphene elicited by electrical stimulation of the optic nerve, such as their coordinates, size, and appearance, which will be very valuable to finalize the implant testing and provide a strong confirmation of the types of phosphene we can expect it would elicit in humans.

4.2.7 Increasing the number of stimulation sites

Perhaps the most important challenge that needs to be solved to bring electrical stimulation of the optic nerve for artificial vision closer to large clinical trials in humans consists of finding ways to increase the number of stimulating sites of the implant. While the OpticSELINE was perfectly suited for the type of proof-of-concept validation study described in this thesis thanks to its already established selectivity and biocompatibility, it was adapted from an implant initially though for the stimulation of the rat sciatic nerve, an application requesting a much smaller number of stimulating sites than what would be needed to restore a meaningful degree of vision in patients.

Thanks to its larger dimensions, this seems more realistic to achieve in the human optic nerve than in the rabbit one. Indeed, its wider diameter of 3-4 mm instead of 1.5 mm would allow to at least double the number of stimulating sites of the current OpticSELINE design if the pitch and electrode dimension is kept the same. Furthermore, with the anterior half of the intra-orbital segment and the whole length of the intracranial segment available for implantation, one can imagine implanting several OpticSELINEs in a single nerve and bring the total number of stimulating sites in the range of the number of stimulating sites of the Argus II, which was the first retinal implant authorized for clinical trials³⁴². The natural shift of axons originating from the macular area from the temporal side of the optic nerve in the intra-orbital segment to its center in the pre-chiasmatic area would ensure that similarly implanted devices would stimulate axons corresponding to different portions of the visual field.

However, simulation studies suggest that a visual prosthesis should be able to elicit a minimal number of phosphenes in the 500 to 1000 range in order to allow the patient to read, while others suggest that at least 3,000 are necessary for object recognition^{343,344}. Hence, the implantation of multiple OpticSELINEs would likely not be able to sufficiently increase the number of stimulating sites by itself and will require to be combined with complementary solutions. Innovative micro-fabrication techniques such as the design of electrodes using graphene-oxide are currently being investigated in our group to bring down the diameter of the stimulation sites. Alternatively, rethinking the whole design of the implant to incorporate a higher density of electrode per unit of volume, taking inspiration from the design of the Utah slanted electrode array, for instance, could also need to be considered²⁶⁵.

4.2.8 Field shaping stimulation strategies

A parallel approach to the modification of the implant's design is the development of new stimulation protocols that take advantage of field-shaping strategies, which in addition to the modulation of the stimulating current amplitude discussed in the second chapter of this thesis, could be used to modify the shape of the activated portion of the optic nerve.

The first field shaping strategy that could be used is current steering. This approach involves combining two individually under-threshold current pulses in order that the combined change of voltage they elicit activates the portion of the nerve in-between the two electrodes. This can be used to create an additional "virtual" electrode between two real physical ones. By changing the ratio of the current pulses, the activated area can be steered toward one of the two electrodes, hence the name of the approach.

A second field shaping strategy that can be explored is current focusing, which involves combining standard cathodic stimulating pulses with anodic pulses. This approach takes advantage of the fact that anodic current pulses have a much larger stimulation threshold than cathodic ones. Hence, they can be used to cancel the negative electrical field produced by the cathodic pulse, and therefore two anodic pulses flanking a central cathodic pulse could be used to focus the stimulation of the cathodic pulse to a more compact and controlled portion of the nerve for instance. This approach is currently being investigated in our lab by the addition of an annular return electrode around each central circular electrode of the OpticSELINE, which allows to synchronously deliver an anodic pulse in addition to the cathodic stimulating pulse to greatly control the spread of the activated portion of the nerve by modulating the ratio between the cathodic and anodic pulses (Figure 4-2a-g).

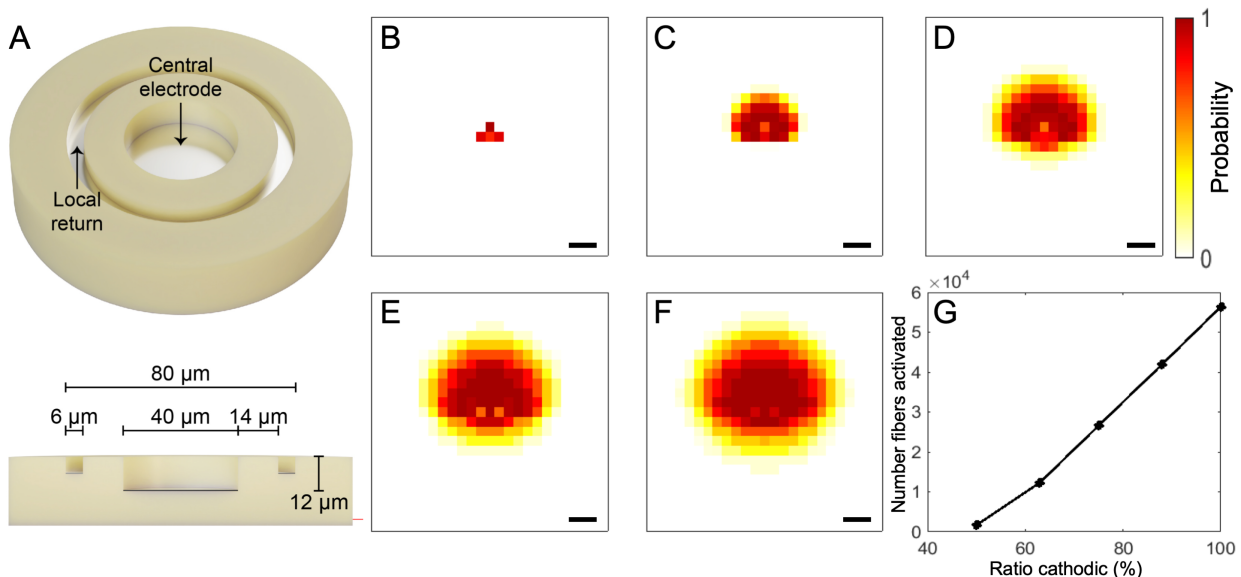


Figure 4-2 | New OpticSELINE probability activation map of different cathodic ratios. (a) Top and side view of the design of a stimulating site of the new OpticSELINE design with the added annular return electrode. Panel reproduce from E. Borda unpublished work. (b-f) Maps of the probability of activation of the optic nerve for a total current injected (sum of the magnitude of the cathodic current pulse injected through the central electrode and the anodic pulse injected through the annular return electrode) of 150 μA at different cathodic ratios. The indicated ratio corresponds to the fraction of the total injected current made out of the cathodic pulse; for instance, a 50% ratio corresponds to a 75 μA cathodic pulse and a 75 μA anodic pulse, and a 100% ratio corresponds to a 150 μA cathodic pulse and a 0 μA anodic pulse. The probability of activation corresponds to the probability that a given pair of coordinates of the optic nerve cross-section contains a fiber that is activated (an action potential travels its whole length) by the injected current. The scale bars are 150 μm . (g) Quantification of the number of fibers activated as a function of the cathodic ratio based on a fiber density of 0.19 fibers per μm^2 . The larger the cathodic ratio, the more axonal fibers are activated.

A third field-shaping strategy similar to the second one that could be tested only with several implants along the length of the optic nerve would consist of delivering anodic pulses downstream of the stimulation to effectively locally hyperpolarize the membrane of the axons and therefore potentially block the propagation of upstream action potential, providing an additional way to modulate the activated portion of the nerve.

4.3 Outlook

While the principle of optic nerve stimulation for artificial vision is similar to epiretinal implants in terms of target cells, it is markedly different in terms of the shape and dimension of the anatomical structure it targets, and therefore involves the development of unique technological solutions to overcome its specific limitations. Even if this approach may appear challenging, we believe that it still provides several distinct advantages that make it worth exploring. The field of intraneural optic nerve stimulation is still in its infancy, so the possibility of bringing it to the clinic remains speculative. Regardless, as it is initially inspired by peripheral nerve stimulation, this approach has the advantage that any advances developed for it may very easily translate back and find useful applications in the field of peripheral nerve stimulation, such as delivering enhanced sensory feedback to improve the control of a robotic arm prosthesis for instance.

Like any other visual prostheses, optic nerve stimulation has some inherent limitations; indeed, unless future technological developments allow reaching single-cell stimulation levels of selectivity, visual prostheses are bound to stimulate several cells at once, simultaneously recruiting both ON and OFF cells. This may ultimately limit how naturalistic the restored vision may be and relies on the plasticity and training of the cortex to make sense of what may initially appear as incongruous physiological stimulation. While promising more biologically oriented alternatives to visual prosthesis are currently being explored, such as autologous stem cell transplants or gene therapy, that may restore a more naturalistic and higher resolution vision, they are still in an early stage of development^{345–350}. In the meantime, visual prosthesis appears as a useful intermediate solution, with the potential to drastically improve the daily life of millions of people worldwide.

References

1. Kolb, H. Gross Anatomy of the Eye. in *Webvision: The Organization of the Retina and Visual System* (eds. Kolb, H., Fernandez, E. & Nelson, R.) (University of Utah Health Sciences Center, 1995).
2. Ehrlich, R., Harris, A., Wentz, S. M., Moore, N. A. & Siesky, B. A. Anatomy and Regulation of the Optic Nerve Blood Flow☆. in *Reference Module in Neuroscience and Biobehavioral Psychology* (Elsevier, 2017). doi:10.1016/B978-0-12-809324-5.01301-8.
3. Armstrong, R. A. & Cubbidge, R. C. 1 - The Eye and Vision: An Overview. in *Handbook of Nutrition, Diet, and the Eye (Second Edition)* (eds. Preedy, V. R. & Watson, R. R.) 3–14 (Academic Press, 2019). doi:10.1016/B978-0-12-815245-4.00001-6.
4. Strauss, O. The Retinal Pigment Epithelium in Visual Function. *Physiological Reviews* **85**, 845–881 (2005).
5. Strauss, O. The retinal pigment epithelium in visual function. *Physiol Rev* **85**, 845–881 (2005).
6. Mirochnik, R. M. & Pezaris, J. S. Contemporary approaches to visual prostheses. *Military Med Res* **6**, 19 (2019).
7. Goetz, G. A. & Palanker, D. V. Electronic Approaches to Restoration of Sight. 57.
8. Euler, T., Haverkamp, S., Schubert, T. & Baden, T. Retinal bipolar cells: elementary building blocks of vision. *Nature Reviews Neuroscience* **15**, 507–519 (2014).
9. CAJAL, S. R. La retine des vertebres. *Cellule* **9**, 119–255 (1893).
10. Photoreception - Structure and function of photoreceptors. *Encyclopedia Britannica* <https://www.britannica.com/science/photoreception>.
11. Cao, D. Chapter 10 - Color Vision and Night Vision. in *Retina (Fifth Edition)* (eds. Ryan, S. J. et al.) 285–299 (W.B. Saunders, 2013). doi:10.1016/B978-1-4557-0737-9.00010-2.
12. Curcio, C. A., Sloan, K. R., Packer, O., Hendrickson, A. E. & Kalina, R. E. Distribution of cones in human and monkey retina: individual variability and radial asymmetry. *Science* **236**, 579–582 (1987).
13. Zhang, T. *et al.* Variability in human cone topography assessed by adaptive optics scanning laser ophthalmoscopy. *Am J Ophthalmol* **160**, 290-300.e1 (2015).
14. Curcio, C. A., Sloan, K. R., Kalina, R. E. & Hendrickson, A. E. Human photoreceptor topography. *J Comp Neurol* **292**, 497–523 (1990).
15. *Webvision: The Organization of the Retina and Visual System*. (University of Utah Health Sciences Center, 1995).
16. Osterberg, G. *Topography of the Layer of Rods and Cones in the Human Retina*. (A. Busck, 1935).
17. Bowmaker, J. K. & Dartnall, H. J. Visual pigments of rods and cones in a human retina. *J Physiol* **298**, 501–511 (1980).

18. Brown, P. K. & Wald, G. Visual Pigments in Single Rods and Cones of the Human Retina. *Science* **144**, 45–52 (1964).
19. Ahnelt, P. K., Kolb, H. & Pflug, R. Identification of a subtype of cone photoreceptor, likely to be blue sensitive, in the human retina. *J Comp Neurol* **255**, 18–34 (1987).
20. Curcio, C. A. *et al.* Distribution and morphology of human cone photoreceptors stained with anti-blue opsin. *J Comp Neurol* **312**, 610–624 (1991).
21. Cicerone, C. M. & Nerger, J. L. The relative numbers of long-wavelength-sensitive to middle-wavelength-sensitive cones in the human fovea centralis. *Vision Res* **29**, 115–128 (1989).
22. Roorda, A. & Williams, D. R. The arrangement of the three cone classes in the living human eye. *Nature* **397**, 520–522 (1999).
23. Dacey, D. M. Primate retina: cell types, circuits and color opponency. *Prog Retin Eye Res* **18**, 737–763 (1999).
24. Dowling, J. E., Boycott, B. B. & Wells, G. P. Organization of the primate retina: electron microscopy. *Proceedings of the Royal Society of London. Series B. Biological Sciences* **166**, 80–111 (1966).
25. Boycott, B. B. & Wässle, H. Morphological Classification of Bipolar Cells of the Primate Retina. *Eur J Neurosci* **3**, 1069–1088 (1991).
26. Kolb, H., Linberg, K. A. & Fisher, S. K. Neurons of the human retina: a Golgi study. *J Comp Neurol* **318**, 147–187 (1992).
27. Wässle, H. & Boycott, B. B. Functional architecture of the mammalian retina. *Physiol Rev* **71**, 447–480 (1991).
28. Dacey, D. M. Primate retina: cell types, circuits and color opponency. *Progress in Retinal and Eye Research* **18**, 737–763 (1999).
29. Verweij, J., Dacey, D. M., Peterson, B. B. & Buck, S. L. Sensitivity and dynamics of rod signals in H1 horizontal cells of the macaque monkey retina. *Vision Research* **39**, 3662–3672 (1999).
30. Dacey, D. M. Parallel pathways for spectral coding in primate retina. *Annu Rev Neurosci* **23**, 743–775 (2000).
31. MacNeil, M. A. & Masland, R. H. Extreme diversity among amacrine cells: implications for function. *Neuron* **20**, 971–982 (1998).
32. Zrenner, E. Fighting blindness with microelectronics. *Sci Transl Med* **5**, 210ps16 (2013).
33. Dacey, D. M., Peterson, B. B., Robinson, F. R. & Gamlin, P. D. Fireworks in the Primate Retina: In Vitro Photodynamics Reveals Diverse LGN-Projecting Ganglion Cell Types. *Neuron* **37**, 15–27 (2003).
34. Perry, V. H., Oehler, R. & Cowey, A. Retinal ganglion cells that project to the dorsal lateral geniculate nucleus in the macaque monkey. *Neuroscience* **12**, 1101–1123 (1984).
35. Dreher, B., Fukada, Y. & Rodieck, R. W. Identification, classification and anatomical segregation of

- cells with X-like and Y-like properties in the lateral geniculate nucleus of old-world primates. *J Physiol* **258**, 433–452 (1976).
36. Li, P. H. *et al.* Anatomical identification of extracellularly recorded cells in large-scale multielectrode recordings. *J Neurosci* **35**, 4663–4675 (2015).
37. De Monasterio, F. M. & Gouras, P. Functional properties of ganglion cells of the rhesus monkey retina. *J Physiol* **251**, 167–195 (1975).
38. Dacey, D. M. & Petersen, M. R. Dendritic field size and morphology of midget and parasol ganglion cells of the human retina. *Proc Natl Acad Sci U S A* **89**, 9666–9670 (1992).
39. Kaplan, E. & Shapley, R. M. The primate retina contains two types of ganglion cells, with high and low contrast sensitivity. *Proc Natl Acad Sci U S A* **83**, 2755–2757 (1986).
40. Livingstone, M. & Hubel, D. Segregation of form, color, movement, and depth: anatomy, physiology, and perception. *Science* **240**, 740–749 (1988).
41. Sun, H., Rüttiger, L. & Lee, B. B. The spatiotemporal precision of ganglion cell signals: a comparison of physiological and psychophysical performance with moving gratings. *Vision Res* **44**, 19–33 (2004).
42. Field, G. D. & Chichilnisky, E. J. Information processing in the primate retina: circuitry and coding. *Annu Rev Neurosci* **30**, 1–30 (2007).
43. Dacey, D. M. The mosaic of midget ganglion cells in the human retina. *J Neurosci* **13**, 5334–5355 (1993).
44. Watanabe, M. & Rodieck, R. W. Parasol and midget ganglion cells of the primate retina. *J Comp Neurol* **289**, 434–454 (1989).
45. Nassi, J. J. & Callaway, E. M. Parallel processing strategies of the primate visual system. *Nat Rev Neurosci* **10**, 360–372 (2009).
46. Larabi, M.-C., Rosselli, V. & Fernandez-Maloigne, C. Image Compression Standards and their HVS-Based Optimization : Application to Digital Cinema Profile of JPEG 2000. /paper/Image-Compression-Standards-and-their-HVS-Based-%3A-Larabi-Rosselli/a891022f61cfa744e496abb5714a1f3bf4cefc2 (2009).
47. Trifonov, I. U. [Study of synaptic transmission between photoreceptor and horizontal cell by electric stimulations of the retina]. *Biofizika* **13**, 809–817 (1968).
48. Pulagam, L. P. & Palczewski, K. Phototransduction: Rhodopsin. in *Encyclopedia of the Eye* (ed. Dartt, D. A.) 403–412 (Academic Press, 2010). doi:10.1016/B978-0-12-374203-2.00183-4.
49. Purves, D. Phototransduction. in *Neuroscience 2nd edition* (2001).
50. Hsu, Y.-T. & Molday, R. S. Modulation of the cGMP-gated channel of rod photoreceptor cells by calmodulin. *Nature* **361**, 76–79 (1993).
51. Arshavsky, V. Y., Lamb, T. D. & Pugh, E. N. G Proteins and Phototransduction. *Annu. Rev. Physiol.* **64**, 153–187 (2002).

-
52. Tomita, T. Electrophysiological study of the mechanisms subserving color coding in the fish retina. *Cold Spring Harb Symp Quant Biol* **30**, 559–566 (1965).
53. Eagle, R. C. Eye Pathology: An Atlas and Text, 2nd Edition. *Neuropathology and Applied Neurobiology* **38**, 395–395 (2012).
54. Zurak, N. *Border Archetype, second English edition*. (2018).
55. Werblin, F. S. & Dowling, J. E. Organization of the retina of the mudpuppy, *Necturus maculosus*. II. Intracellular recording. *J Neurophysiol* **32**, 339–355 (1969).
56. Kaneko, A. Physiological and morphological identification of horizontal, bipolar and amacrine cells in goldfish retina. *J Physiol* **207**, 623–633 (1970).
57. Mangel, S. C. Analysis of the horizontal cell contribution to the receptive field surround of ganglion cells in the rabbit retina. *J Physiol* **442**, 211–234 (1991).
58. Packer, O. S. & Dacey, D. M. Receptive field structure of H1 horizontal cells in macaque monkey retina. *J Vis* **2**, 272–292 (2002).
59. Schubert, T. *et al.* Development of presynaptic inhibition onto retinal bipolar cell axon terminals is subclass-specific. *J Neurophysiol* **100**, 304–316 (2008).
60. van Wyk, M., Wässle, H. & Taylor, W. R. Receptive field properties of ON- and OFF-ganglion cells in the mouse retina. *Vis Neurosci* **26**, 297–308 (2009).
61. Ströh, S. *et al.* Eliminating Glutamatergic Input onto Horizontal Cells Changes the Dynamic Range and Receptive Field Organization of Mouse Retinal Ganglion Cells. *J Neurosci* **38**, 2015–2028 (2018).
62. Fahey, P. K. & Burkhardt, D. A. Center-surround organization in bipolar cells: symmetry for opposing contrasts. *Vis Neurosci* **20**, 1–10 (2003).
63. Nelson, R. & Kolb, H. Synaptic patterns and response properties of bipolar and ganglion cells in the cat retina. *Vision Res* **23**, 1183–1195 (1983).
64. Slaughter, M. M. & Miller, R. F. An excitatory amino acid antagonist blocks cone input to sign-conserving second-order retinal neurons. *Science* **219**, 1230–1232 (1983).
65. Nawy, S. & Copenhagen, D. R. Multiple classes of glutamate receptor on depolarizing bipolar cells in retina. *Nature* **325**, 56–58 (1987).
66. Slaughter, M. M. & Miller, R. F. 2-amino-4-phosphonobutyric acid: a new pharmacological tool for retina research. *Science* **211**, 182–185 (1981).
67. Casagrande, V. A. The First Steps in Seeing, by Robert W. Rodieck. *Trends in Neurosciences* **22**, 327–328 (1999).
68. Salazar, J. J. *et al.* Anatomy of the Human Optic Nerve: Structure and Function. *Optic Nerve* (2018) doi:10.5772/intechopen.79827.
69. Forrester, J. V., Dick, A. D., McMenemy, P. G., Roberts, F. & Pearlman, E. *The Eye E-Book: Basic*

Sciences in Practice. (Saunders Ltd., 2015).

70. Hayreh, S. S. The sheath of the optic nerve. *Ophthalmologica* **189**, 54–63 (1984).
71. MD, M. Y. & MHA, J. W. S. M. *Ocular Pathology*. (Elsevier, 2019).
72. Huxley, A. F. & Stämpfli, R. Evidence for saltatory conduction in peripheral myelinated nerve fibres. *J Physiol* **108**, 315–339 (1949).
73. Purves, D. *et al*. Increased Conduction Velocity as a Result of Myelination. *Neuroscience. 2nd edition* (2001).
74. Ramírez, J. M., Triviño, A., Ramírez, A. I., Salazar, J. J. & García-Sánchez, J. Structural specializations of human retinal glial cells. *Vision Res* **36**, 2029–2036 (1996).
75. Di Polo, A., Aigner, L. J., Dunn, R. J., Bray, G. M. & Aguayo, A. J. Prolonged delivery of brain-derived neurotrophic factor by adenovirus-infected Müller cells temporarily rescues injured retinal ganglion cells. *Proc Natl Acad Sci U S A* **95**, 3978–3983 (1998).
76. Dreyer, E. B., Zurakowski, D., Schumer, R. A., Podos, S. M. & Lipton, S. A. Elevated glutamate levels in the vitreous body of humans and monkeys with glaucoma. *Arch Ophthalmol* **114**, 299–305 (1996).
77. Perry, V. H., Bell, M. D., Brown, H. C. & Matyszak, M. K. Inflammation in the nervous system. *Current Opinion in Neurobiology* **5**, 636–641 (1995).
78. Gehrmann, J., Matsumoto, Y. & Kreutzberg, G. W. Microglia: Intrinsic immune effector cell of the brain. *Brain Research Reviews* **20**, 269–287 (1995).
79. Aloisi, F. Immune function of microglia. *Glia* **36**, 165–179 (2001).
80. Gallego, B. I. *et al*. IOP induces upregulation of GFAP and MHC-II and microglia reactivity in mice retina contralateral to experimental glaucoma. *J Neuroinflammation* **9**, 92 (2012).
81. Dandona, L., Quigley, H. A., Brown, A. E. & Enger, C. Quantitative regional structure of the normal human lamina cribrosa. A racial comparison. *Arch Ophthalmol* **108**, 393–398 (1990).
82. Maeda, H., Nakamura, M. & Yamamoto, M. Morphometric features of laminar pores in lamina cribrosa observed by scanning laser ophthalmoscopy. *Jpn J Ophthalmol* **43**, 415–421 (1999).
83. Jonas, J. B., Königsreuther, K. A. & Naumann, G. O. Optic disc histomorphometry in normal eyes and eyes with secondary angle-closure glaucoma. II. Parapapillary region. *Graefes Arch Clin Exp Ophthalmol* **230**, 134–139 (1992).
84. Morgan-Davies, J. *et al*. Three dimensional analysis of the lamina cribrosa in glaucoma. *Br J Ophthalmol* **88**, 1299–1304 (2004).
85. Jeffery, G. *et al*. The human optic nerve: fascicular organisation and connective tissue types along the extra-fascicular matrix. *Anat Embryol (Berl)* **191**, 491–502 (1995).
86. Balcer, L. J. & Prasad, S. ABNORMALITIES OF THE OPTIC NERVE AND RETINA. 14.

87. Barham, H. P., Ramakrishnan, V. R. & Kingdom, T. T. Chapter 19 - Optic Nerve Decompression. in *Atlas of Endoscopic Sinus and Skull Base Surgery (Second Edition)* (eds. Chiu, A. G., Palmer, J. N. & Adappa, N. D.) 157–164 (Elsevier, 2019). doi:10.1016/B978-0-323-47664-5.00019-5.
88. Kline, L. B. *Neuro-Ophthalmology Review Manual*. (Slack Incorporated, 2012).
89. Trattler, W. B., Kaiser, P. K. & Friedman, N. J. *Review of Ophthalmology: Expert Consult - Online and Print*. (Saunders, 2012).
90. Leventhal, A. G., Vitek, D. J. & Creel, D. J. Abnormal visual pathways in normally pigmented cats that are heterozygous for albinism. *Science* **229**, 1395–1397 (1985).
91. Hoffmann, M. B., Tolhurst, D. J., Moore, A. T. & Morland, A. B. Organization of the Visual Cortex in Human Albinism. *J. Neurosci.* **23**, 8921–8930 (2003).
92. Guillery, R. W. Why do albinos and other hypopigmented mutants lack normal binocular vision, and what else is abnormal in their central visual pathways? *Eye* **10**, 217–221 (1996).
93. Banihani, S. M. Loss of binocular vision as direct cause for misrouting of temporal retinal fibers in albinism. *Medical Hypotheses* **85**, 458–462 (2015).
94. Creel, D. J. & Sheridan, C. L. Monocular acquisition and interocular transfer in albino rats with unilateral striate ablations. *Psychon Sci* **6**, 89–90 (1966).
95. Guillery, R. W. *et al.* Abnormal central visual pathways in the brain of an albino green monkey (*Cercopithecus aethiops*). *J Comp Neurol* **226**, 165–183 (1984).
96. Gayer, N. S., Horsburgh, G. M. & Dreher, B. Developmental changes in the pattern of retinal projections in pigmented and albino rabbits. *Brain Res Dev Brain Res* **50**, 33–54 (1989).
97. Fitzgibbon, T. & Taylor, S. F. Retinotopy of the human retinal nerve fibre layer and optic nerve head. *J Comp Neurol* **375**, 238–251 (1996).
98. Minckler, D. S. Nerve fiber layer of the macaque retina: Retinotopic organization. *Survey of Ophthalmology* **28**, 138–139 (1983).
99. Ogden, T. E. Nerve fiber layer of the owl monkey retina: retinotopic organization. *Invest. Ophthalmol. Vis. Sci.* **24**, 265–269 (1983).
100. Naito, J. Retinogeniculate projection fibers in the monkey optic nerve: A demonstration of the fiber pathways by retrograde axonal transport of WGA-HRP. *J. Comp. Neurol.* **284**, 174–186 (1989).
101. Campbell, W. W. & DeJong, R. N. *DeJong's the Neurologic Examination*. (Lippincott Williams & Wilkins, 2005).
102. Hughes, A. Topographical relationships between the anatomy and physiology of the rabbit visual system. *Doc Ophthalmol* **30**, 33–159 (1971).
103. Oyster, C. W., Takahashi, E. S. & Hurst, D. C. Density, soma size, and regional distribution of rabbit retinal ganglion cells. *J Neurosci* **1**, 1331–1346 (1981).

104. Lashley, K. S. The mechanism of vision. VII. The projection of the retina upon the primary optic centers in the rat. *J. Comp. Neurol.* **59**, 341–373 (1934).
105. Brouwer, B. Experimentelle- anatomische Untersuchungen ueber die Projektion der Retina auf die primaren Opticuszentren. *Schweiz. Arch. f. Neurol. u. Psychiat.*, 118–137.
106. Tsuruga, H. Retinotopy in the Optic Nerve Using CFP-Expressing Transgenic Mouse | IOVS | . in (2009).
107. Mikelberg, F. S., Drance, S. M., Schulzer, M., Yidegiligne, H. M. & Weis, M. M. The normal human optic nerve. Axon count and axon diameter distribution. *Ophthalmology* **96**, 1325–1328 (1989).
108. Vaney, D. I. & Hughes, A. The rabbit optic nerve: fibre diameter spectrum, fibre count, and comparison with a retinal ganglion cell count. *J Comp Neurol* **170**, 241–251 (1976).
109. Drenhaus, U., von Gunten, A. & Rager, G. Classes of axons and their distribution in the optic nerve of the tree shrew (*Tupaia belangeri*). *Anat Rec* **249**, 103–116 (1997).
110. Rodieck, R. W., Binmoeller, K. F. & Dineen, J. Parasol and midget ganglion cells of the human retina. *J Comp Neurol* **233**, 115–132 (1985).
111. FitzGibbon, T. & Taylor, S. F. Mean retinal ganglion cell axon diameter varies with location in the human retina. *Jpn J Ophthalmol* **56**, 631–637 (2012).
112. Perry, V. H., Oehler, R. & Cowey, A. Retinal ganglion cells that project to the dorsal lateral geniculate nucleus in the macaque monkey. *Neuroscience* **12**, 1101–1123 (1984).
113. Conley, M. & Fitzpatrick, D. Morphology of retinogeniculate axons in the macaque. *Visual Neuroscience* **2**, 287–296 (1989).
114. Leventhal, A. G., Rodieck, R. W. & Dreher, B. Retinal ganglion cell classes in the Old World monkey: morphology and central projections. *Science* **213**, 1139–1142 (1981).
115. Perry, V. H. & Cowey, A. The morphological correlates of X- and Y-like retinal ganglion cells in the retina of monkeys. *Exp Brain Res* **43**, 226–228 (1981).
116. Schiller, P. H. & Malpeli, J. G. Functional specificity of lateral geniculate nucleus laminae of the rhesus monkey. *J Neurophysiol* **41**, 788–797 (1978).
117. Hendry, S. H. C. & Reid, R. C. The koniocellular pathway in primate vision. *Annual review of neuroscience* **23**, 127–153 (2000).
118. Hubel, D. H. & Wiesel, T. N. Laminar and columnar distribution of geniculocortical fibers in the macaque monkey. *Journal of Comparative Neurology* **146**, 421–450 (1972).
119. Schneider, K. A., Richter, M. C. & Kastner, S. Retinotopic Organization and Functional Subdivisions of the Human Lateral Geniculate Nucleus: A High-Resolution Functional Magnetic Resonance Imaging Study. *J. Neurosci.* **24**, 8975–8985 (2004).
120. Hubel, D. H. & Wiesel, T. N. Integrative action in the cat's lateral geniculate body. *J Physiol* **155**, 385–398 (1961).

-
121. Brodmann, K. *Vergleichende Lokalisationslehre der Grosshirnrinde in ihren Prinzipien dargestellt auf Grund des Zellenbaues von Dr. K. Brodmann ...* (J.A. Barth, 1909).
122. Blasdel, G. G. & Fitzpatrick, D. Physiological organization of layer 4 in macaque striate cortex. *J. Neurosci.* **4**, 880–895 (1984).
123. Blasdel, G. G. & Lund, J. S. Termination of afferent axons in macaque striate cortex. *J Neurosci* **3**, 1389–1413 (1983).
124. Chatterjee, S. & Callaway, E. M. Parallel colour-opponent pathways to primary visual cortex. *Nature* **426**, 668–671 (2003).
125. Hendrickson, A. E., Wilson, J. R. & Ogren, M. P. The neuroanatomical organization of pathways between the dorsal lateral geniculate nucleus and visual cortex in Old World and New World primates. *J Comp Neurol* **182**, 123–136 (1978).
126. Hendry, S. H. & Yoshioka, T. A neurochemically distinct third channel in the macaque dorsal lateral geniculate nucleus. *Science* **264**, 575–577 (1994).
127. Livingstone, M. S. & Hubel, D. H. Thalamic inputs to cytochrome oxidase-rich regions in monkey visual cortex. *Proc Natl Acad Sci U S A* **79**, 6098–6101 (1982).
128. Tootell, R. B. *et al.* Functional analysis of primary visual cortex (V1) in humans. *Proc Natl Acad Sci U S A* **95**, 811–817 (1998).
129. Duncan, R. O. & Boynton, G. M. Cortical magnification within human primary visual cortex correlates with acuity thresholds. *Neuron* **38**, 659–671 (2003).
130. Daniel, P. M. & Whitteridge, D. The representation of the visual field on the cerebral cortex in monkeys. *J Physiol* **159**, 203–221 (1961).
131. Weymouth, F. W. Visual Sensory Units and the Minimal Angle of Resolution*. *American Journal of Ophthalmology* **46**, 102–113 (1958).
132. Bauer, R., Dow, B. M. & Vautin, R. G. Laminar distribution of preferred orientations in foveal striate cortex of the monkey. *Exp Brain Res* **41**, 54–60 (1980).
133. Bullier, J. & Henry, G. H. Ordinal position and afferent input of neurons in monkey striate cortex. *J Comp Neurol* **193**, 913–935 (1980).
134. Hubel, D. H. & Wiesel, T. N. Receptive fields of single neurones in the cat's striate cortex. *J Physiol* **148**, 574–591 (1959).
135. Hubel, D. H. & Wiesel, T. N. Receptive fields, binocular interaction and functional architecture in the cat's visual cortex. *J Physiol* **160**, 106–154 (1962).
136. Mountcastle, V. B. Modality and topographic properties of single neurons of cat's somatic sensory cortex. *J Neurophysiol* **20**, 408–434 (1957).
137. Hubel, D. H. & Wiesel, T. N. Receptive fields and functional architecture of monkey striate cortex. *J*

Physiol **195**, 215–243 (1968).

138. Hubel, D. H. & Wiesel, T. N. Sequence regularity and geometry of orientation columns in the monkey striate cortex. *J Comp Neurol* **158**, 267–293 (1974).
139. Wiesel, T. N., Hubel, D. H. & Lam, D. M. Autoradiographic demonstration of ocular-dominance columns in the monkey striate cortex by means of transneuronal transport. *Brain Res* **79**, 273–279 (1974).
140. Bonhoeffer, T. & Grinvald, A. Iso-orientation domains in cat visual cortex are arranged in pinwheel-like patterns. *Nature* **353**, 429–431 (1991).
141. Blasdel, G., Obermayer, K. & Kiorpes, L. Organization of ocular dominance and orientation columns in the striate cortex of neonatal macaque monkeys. *Vis Neurosci* **12**, 589–603 (1995).
142. Paulun, L., Wendt, A. & Kasabov, N. A Retinotopic Spiking Neural Network System for Accurate Recognition of Moving Objects Using NeuCube and Dynamic Vision Sensors. *Front Comput Neurosci* **12**, 42 (2018).
143. Sadeh, S. & Rotter, S. Statistics and geometry of orientation selectivity in primary visual cortex. *Biol Cybern* **108**, 631–653 (2014).
144. Blasdel, G. G. & Salama, G. Voltage-sensitive dyes reveal a modular organization in monkey striate cortex. *Nature* **321**, 579–585 (1986).
145. Oster, A. M. & Bressloff, P. C. A developmental model of ocular dominance column formation on a growing cortex. *Bull Math Biol* **68**, 73–98 (2006).
146. Hubel, D. H. & Wiesel, T. N. Ferrier lecture. Functional architecture of macaque monkey visual cortex. *Proc R Soc Lond B Biol Sci* **198**, 1–59 (1977).
147. Malvoyance et handicaps visuels. *SNOF* <https://www.snof.org/public/conseiller/malvoyance-et-handicaps-visuels>.
148. The Eyecare Trust - Registering As Blind or Partially Sighted. https://www.eyecaretrust.org.uk/view.php?item_id=56.
149. The Situation of the Blind and Visually Impaired in Germany — An Overview | American Council of the Blind. <https://acb.org/situation-blind-and-visually-impaired-germany>.
150. Lee, S. Y. & Mesfin, F. B. Blindness. in *StatPearls* (StatPearls Publishing, 2021).
151. Rovner, B. W., Casten, R. J. & Tasman, W. S. Effect of depression on vision function in age-related macular degeneration. *Arch Ophthalmol* **120**, 1041–1044 (2002).
152. Berman, K. & Brodaty, H. Psychosocial effects of age-related macular degeneration. *Int Psychogeriatr* **18**, 415–428 (2006).
153. Owsley, C. & McGwin, G. Bidirectionality of the Association of Vision Impairment With Depression and Anxiety. *JAMA Ophthalmol* **137**, 801 (2019).
154. Foster, A., Gilbert, C. & Johnson, G. Changing patterns in global blindness: 1988–2008. 3.

155. Bourne, R. R. A. *et al.* Causes of vision loss worldwide, 1990-2010: a systematic analysis. *Lancet Glob Health* **1**, e339-349 (2013).
156. Bourne, R. R. A. *et al.* Magnitude, temporal trends, and projections of the global prevalence of blindness and distance and near vision impairment: a systematic review and meta-analysis. *Lancet Glob Health* **5**, e888–e897 (2017).
157. Lambertus, S. *et al.* Highly sensitive measurements of disease progression in rare disorders: Developing and validating a multimodal model of retinal degeneration in Stargardt disease. *PLoS One* **12**, (2017).
158. Lim, L. S., Mitchell, P., Seddon, J. M., Holz, F. G. & Wong, T. Y. Age-related macular degeneration. *The Lancet* **379**, 1728–1738 (2012).
159. Wong, W. L. *et al.* Global prevalence of age-related macular degeneration and disease burden projection for 2020 and 2040: a systematic review and meta-analysis. *Lancet Glob Health* **2**, e106-116 (2014).
160. Klein, R., Peto, T., Bird, A. & Vannewkirk, M. R. The epidemiology of age-related macular degeneration. *Am J Ophthalmol* **137**, 486–495 (2004).
161. Zarbin, M. A. Current concepts in the pathogenesis of age-related macular degeneration. *Arch Ophthalmol* **122**, 598–614 (2004).
162. Allikmets, R. *et al.* Mutation of the Stargardt disease gene (ABCR) in age-related macular degeneration. *Science* **277**, 1805–1807 (1997).
163. Boon, C. J. F. *et al.* Basal laminar drusen caused by compound heterozygous variants in the CFH gene. *Am J Hum Genet* **82**, 516–523 (2008).
164. Cameron, D. J. *et al.* HTRA1 variant confers similar risks to geographic atrophy and neovascular age-related macular degeneration. *Cell Cycle* **6**, 1122–1125 (2007).
165. Chen, H. *et al.* Association of HTRA1 polymorphism and bilaterality in advanced age-related macular degeneration. *Vision Res* **48**, 690–694 (2008).
166. Cremers, F. P. *et al.* Autosomal recessive retinitis pigmentosa and cone-rod dystrophy caused by splice site mutations in the Stargardt's disease gene ABCR. *Hum Mol Genet* **7**, 355–362 (1998).
167. Thornton, J. *et al.* Smoking and age-related macular degeneration: a review of association. *Eye* **19**, 935–944 (2005).
168. Dasari, B., Prasanthi, J. R., Marwarha, G., Singh, B. B. & Ghribi, O. Cholesterol-enriched diet causes age-related macular degeneration-like pathology in rabbit retina. *BMC Ophthalmol* **11**, 22 (2011).
169. Denniss, J., Baggaley, H. C., Brown, G. M., Rubin, G. S. & Astle, A. T. Properties of Visual Field Defects Around the Monocular Preferred Retinal Locus in Age-Related Macular Degeneration. *Invest Ophthalmol Vis Sci* **58**, 2652–2658 (2017).
170. Tarita-Nistor, L., González, E. G., Markowitz, S. N., Lillakas, L. & Steinbach, M. J. Increased role of peripheral vision in self-induced motion in patients with age-related macular degeneration. *Invest Ophthalmol Vis Sci* **49**, 3253–3258 (2008).

171. Mathenge, W. Age-related macular degeneration. *Community Eye Health* **27**, 49–50 (2014).
172. Acton, J. H., Gibson, J. M. & Cubbidge, R. P. Quantification of visual field loss in age-related macular degeneration. *PLoS One* **7**, e39944 (2012).
173. Yue, L., Weiland, J. D., Roska, B. & Humayun, M. S. Retinal stimulation strategies to restore vision: Fundamentals and systems. *Prog Retin Eye Res* **53**, 21–47 (2016).
174. Parvini, M. *et al.* Human pluripotent stem cell-derived retinal pigmented epithelium in retinal treatment: from bench to bedside. *Mol Neurobiol* **50**, 597–612 (2014).
175. Maladies de la rétine. *SNOF* <https://www.snof.org/encyclopedie/maladies-de-la-r%C3%A9tine-0>.
176. Fariss, R. N., Li, Z. Y. & Milam, A. H. Abnormalities in rod photoreceptors, amacrine cells, and horizontal cells in human retinas with retinitis pigmentosa. *Am J Ophthalmol* **129**, 215–223 (2000).
177. Hamel, C. Retinitis pigmentosa. *Orphanet Journal of Rare Diseases* **1**, 40 (2006).
178. Hartong, D. T., Berson, E. L. & Dryja, T. P. Retinitis pigmentosa. *Lancet* **368**, 1795–1809 (2006).
179. Daiger, S. P., Bowne, S. J. & Sullivan, L. S. Perspective on Genes and Mutations Causing Retinitis Pigmentosa. *Arch Ophthalmol* **125**, 151–158 (2007).
180. Ferrari, S. *et al.* Retinitis pigmentosa: genes and disease mechanisms. *Curr Genomics* **12**, 238–249 (2011).
181. RetNet - Retinal Information Network. <https://sph.uth.edu/retnet/>.
182. Massof, R. W. & Finkelstein, D. Two forms of autosomal dominant primary retinitis pigmentosa. *Doc Ophthalmol* **51**, 289–346 (1981).
183. Grover, S., Fishman, G. A. & Brown, J. Patterns of visual field progression in patients with retinitis pigmentosa. *Ophthalmology* **105**, 1069–1075 (1998).
184. Birch, D. G., Anderson, J. L. & Fish, G. E. Yearly rates of rod and cone functional loss in retinitis pigmentosa and cone-rod dystrophy. *Ophthalmology* **106**, 258–268 (1999).
185. Kim, S. Y. *et al.* Morphometric analysis of the macula in eyes with geographic atrophy due to age-related macular degeneration. *Retina* **22**, 464–470 (2002).
186. Santos, A. *et al.* Preservation of the inner retina in retinitis pigmentosa. A morphometric analysis. *Arch Ophthalmol* **115**, 511–515 (1997).
187. Humayun, M. S. *et al.* Morphometric analysis of the extramacular retina from postmortem eyes with retinitis pigmentosa. *Invest Ophthalmol Vis Sci* **40**, 143–148 (1999).
188. Horváth, Á. C. *et al.* Infrared neural stimulation and inhibition using an implantable silicon photonic microdevice. *Microsystems & Nanoengineering* **6**, 1–12 (2020).
189. Rossini, P. M. *et al.* Stump nerve signals during transcranial magnetic motor cortex stimulation recorded in an amputee via longitudinal intrafascicular electrodes. *Exp Brain Res* **210**, 1–11 (2011).

190. Peterman, M. C. *et al.* The Artificial Synapse Chip: a flexible retinal interface based on directed retinal cell growth and neurotransmitter stimulation. *Artif Organs* **27**, 975–985 (2003).
191. Hodgkin, A. L. & Huxley, A. F. Action Potentials Recorded from Inside a Nerve Fibre. *Nature* **144**, 710–711 (1939).
192. Hodgkin, A. L. & Huxley, A. F. A quantitative description of membrane current and its application to conduction and excitation in nerve. *J Physiol* **117**, 500–544 (1952).
193. Kandel, E. R. *et al.* *Principles of Neural Science, Fifth Edition*. (McGraw-Hill Education / Medical, 2012).
194. Rattay, F. Ways to approximate current-distance relations for electrically stimulated fibers. *Journal of Theoretical Biology* **125**, 339–349 (1987).
195. Rattay, F. Modeling the excitation of fibers under surface electrodes. *IEEE Trans Biomed Eng* **35**, 199–202 (1988).
196. Rattay, F. Analysis of models for extracellular fiber stimulation. *IEEE Trans. Biomed. Eng.* **36**, 676–682 (1989).
197. Rattay, F. The basic mechanism for the electrical stimulation of the nervous system. *Neuroscience* **89**, 335–346 (1999).
198. Bickel, C. S., Gregory, C. M. & Dean, J. C. Motor unit recruitment during neuromuscular electrical stimulation: a critical appraisal. *Eur J Appl Physiol* **111**, 2399–2407 (2011).
199. Second Sight Medical Products - Life in a New Light. *Second Sight* <https://secondsight.com/>.
200. Dagnelie, G. *et al.* Performance of real-world functional vision tasks by blind subjects improves after implantation with the Argus® II retinal prosthesis system. *Clin Exp Ophthalmol* **45**, 152–159 (2017).
201. Guo, F., Yang, Y. & Gao, Y. Optimization of Visual Information Presentation for Visual Prosthesis. *Int J Biomed Imaging* **2018**, (2018).
202. Sharmili, N., Swapna, N. & Ramakrishna, G. Comparative analysis of image processing algorithms for visual prosthesis. in *2017 International Conference on Communication and Signal Processing (ICCSP)* 1120–1124 (2017). doi:10.1109/ICCSP.2017.8286551.
203. Löwenstein, K. & Borchardt, M. Symptomatologie und elektrische Reizung bei einer Schußverletzung des Hinterhauptlappens. *Deutsche Zeitschrift f. Nervenheilkunde* **58**, 264–292 (1918).
204. Krause, F. Die Sehbahn in Chirurgischer Beziehung und die Faradische Reizung des Sehzentrumms. *Klin Wochenschr* **3**, 1260–1265 (1924).
205. Spector, R. H. Visual Fields. in *Clinical Methods: The History, Physical, and Laboratory Examinations* (eds. Walker, H. K., Hall, W. D. & Hurst, J. W.) (Butterworths, 1990).
206. Lewis, P. M., Ackland, H. M., Lowery, A. J. & Rosenfeld, J. V. Restoration of vision in blind individuals using bionic devices: a review with a focus on cortical visual prostheses. *Brain Res* **1595**, 51–73 (2015).
207. Fernandes, R. A. B., Diniz, B., Ribeiro, R. & Humayun, M. Artificial vision through neuronal stimulation.

Neuroscience Letters **519**, 122–128 (2012).

208. Opie, N. L., Burkitt, A. N., Meffin, H. & Grayden, D. B. Heating of the eye by a retinal prosthesis: modeling, cadaver and in vivo study. *IEEE Trans Biomed Eng* **59**, 339–345 (2012).
209. Lakhanpal, R. R. *et al.* Advances in the development of visual prostheses. *Curr Opin Ophthalmol* **14**, 122–127 (2003).
210. Weitz, A. C. *et al.* Improving the spatial resolution of epiretinal implants by increasing stimulus pulse duration. *Sci Transl Med* **7**, 318ra203 (2015).
211. Shepherd, R. K., Shivdasani, M. N., Nayagam, D. A. X., Williams, C. E. & Blamey, P. J. Visual prostheses for the blind. *Trends Biotechnol* **31**, 562–571 (2013).
212. Yue, L. *et al.* Ten-Year Follow-up of a Blind Patient Chronically Implanted with Epiretinal Prosthesis Argus I. *Ophthalmology* **122**, 2545-2552.e1 (2015).
213. Ahuja, A. K. & Behrend, M. R. The Argus™ II retinal prosthesis: factors affecting patient selection for implantation. *Prog Retin Eye Res* **36**, 1–23 (2013).
214. Luo, Y. H.-L. & da Cruz, L. The Argus(®) II Retinal Prosthesis System. *Prog Retin Eye Res* **50**, 89–107 (2016).
215. Hadjinicolaou, A. E., Meffin, H., Maturana, M. I., Cloherty, S. L. & Ibbotson, M. R. Prosthetic vision: devices, patient outcomes and retinal research. *Clin Exp Optom* **98**, 395–410 (2015).
216. Bareket, L., Barriga-Rivera, A., Zapf, M. P., Lovell, N. H. & Suaning, G. J. Progress in artificial vision through suprachoroidal retinal implants. *J Neural Eng* **14**, 045002 (2017).
217. Zrenner, E. *et al.* Can subretinal microphotodiodes successfully replace degenerated photoreceptors? *Vision Res* **39**, 2555–2567 (1999).
218. Fujikado, T. *et al.* One-Year Outcome of 49-Channel Suprachoroidal-Transretinal Stimulation Prosthesis in Patients With Advanced Retinitis Pigmentosa. *Invest Ophthalmol Vis Sci* **57**, 6147–6157 (2016).
219. Kanda, H. *et al.* Electrophysiological studies of the feasibility of suprachoroidal-transretinal stimulation for artificial vision in normal and RCS rats. *Invest Ophthalmol Vis Sci* **45**, 560–566 (2004).
220. Ferlauto, L. *et al.* Design and validation of a foldable and photovoltaic wide-field epiretinal prosthesis. *Nat Commun* **9**, 992 (2018).
221. Lorach, H. *et al.* Photovoltaic restoration of sight with high visual acuity. *Nat Med* **21**, 476–482 (2015).
222. Stingl, K. *et al.* Subretinal Visual Implant Alpha IMS--Clinical trial interim report. *Vision Res* **111**, 149–160 (2015).
223. Stingl, K. *et al.* Interim Results of a Multicenter Trial with the New Electronic Subretinal Implant Alpha AMS in 15 Patients Blind from Inherited Retinal Degenerations. *Front. Neurosci.* **11**, (2017).
224. Stingl, K. *et al.* Artificial vision with wirelessly powered subretinal electronic implant alpha-IMS. *Proc Biol Sci* **280**, 20130077 (2013).

225. Veraart, C. *et al.* Visual sensations produced by optic nerve stimulation using an implanted self-sizing spiral cuff electrode. *Brain Res* **813**, 181–186 (1998).
226. Veraart, C., Wanet-Defalque, M.-C., Gérard, B., Vanlierde, A. & Delbeke, J. Pattern recognition with the optic nerve visual prosthesis. *Artif Organs* **27**, 996–1004 (2003).
227. Brelén, M. E. *et al.* Intraorbital implantation of a stimulating electrode for an optic nerve visual prosthesis. Case report. *J Neurosurg* **104**, 593–597 (2006).
228. Brelén, M. E., Duret, F., Gérard, B., Delbeke, J. & Veraart, C. Creating a meaningful visual perception in blind volunteers by optic nerve stimulation. *J Neural Eng* **2**, S22–28 (2005).
229. Sakaguchi, H. *et al.* Artificial vision by direct optic nerve electrode (AV-DONE) implantation in a blind patient with retinitis pigmentosa. *J Artif Organs* **12**, 206–209 (2009).
230. Badia, J. *et al.* Comparative analysis of transverse intrafascicular multichannel, longitudinal intrafascicular and multipolar cuff electrodes for the selective stimulation of nerve fascicles. *J Neural Eng* **8**, 036023 (2011).
231. Raspopovic, S. *et al.* Neural signal recording and processing in somatic neuroprosthetic applications. A review. *Journal of Neuroscience Methods* **337**, 108653 (2020).
232. Cutrone, A. *et al.* A three-dimensional self-opening intraneural peripheral interface (SELINe). *J. Neural Eng.* **12**, 016016 (2015).
233. Sun, J. *et al.* Spatiotemporal properties of multip peaked electrically evoked potentials elicited by penetrative optic nerve stimulation in rabbits. *Invest Ophthalmol Vis Sci* **52**, 146–154 (2011).
234. Lu, Y. *et al.* Electrical stimulation with a penetrating optic nerve electrode array elicits visuotopic cortical responses in cats. *J. Neural Eng.* **10**, 036022 (2013).
235. Jones, B. W. *et al.* Retinal remodeling in human retinitis pigmentosa. *Exp Eye Res* **150**, 149–165 (2016).
236. Jones, B. W. *et al.* Retinal remodeling. *Jpn J Ophthalmol* **56**, 289–306 (2012).
237. Jones, B. W. *et al.* Retinal remodeling triggered by photoreceptor degenerations. *J Comp Neurol* **464**, 1–16 (2003).
238. Watt, C. B., Jones, B. W., Yang, J.-H., Marc, R. E. & LaVail, M. M. Complex Rewiring In Retinal Remodeling. *Invest. Ophthalmol. Vis. Sci.* **45**, 777–777 (2004).
239. Marc, R. E. & Jones, B. W. Retinal remodeling in inherited photoreceptor degenerations. *Mol Neurobiol* **28**, 139–147 (2003).
240. Hickey, P. & Stacy, M. Deep Brain Stimulation: A Paradigm Shifting Approach to Treat Parkinson’s Disease. *Front Neurosci* **10**, 173 (2016).
241. Pezaris, J. S. & Reid, R. C. Demonstration of artificial visual percepts generated through thalamic microstimulation. *PNAS* **104**, 7670–7675 (2007).

242. Pezaris, J. S. & Eskandar, E. N. Getting signals into the brain: visual prosthetics through thalamic microstimulation. *Neurosurg Focus* **27**, E6 (2009).
243. Panetsos, F., Sanchez-Jimenez, A., Cerio, E. D., Diaz-Guemes, I. & Sanchez, F. M. Consistent phosphenes generated by electrical microstimulation of the visual thalamus. An experimental approach for thalamic visual neuroprostheses. *Front Neurosci* **5**, 84 (2011).
244. Mullen, K. T., Dumoulin, S. O. & Hess, R. F. Color responses of the human lateral geniculate nucleus: [corrected] selective amplification of S-cone signals between the lateral geniculate nucleus and primary visual cortex measured with high-field fMRI. *Eur J Neurosci* **28**, 1911–1923 (2008).
245. Brindley, G. S. & Lewin, W. S. The sensations produced by electrical stimulation of the visual cortex. *J Physiol* **196**, 479–493 (1968).
246. Dobelle, W. H. & Mladejovsky, M. G. Phosphenes produced by electrical stimulation of human occipital cortex, and their application to the development of a prosthesis for the blind. *J Physiol* **243**, 553–576.1 (1974).
247. Dobelle, W. H., Mladejovsky, M. G., Evans, J. R., Roberts, T. S. & Girvin, J. P. ‘Braille’ reading by a blind volunteer by visual cortex stimulation. *Nature* **259**, 111–112 (1976).
248. Dobelle, W. H., Quest, D. O., Antunes, J. L., Roberts, T. S. & Girvin, J. P. Artificial vision for the blind by electrical stimulation of the visual cortex. *Neurosurgery* **5**, 521–527 (1979).
249. Pollen, D. A. Responses of single neurons to electrical stimulation of the surface of the visual cortex. *Brain Behav Evol* **14**, 67–86 (1977).
250. Schmidt, E. M. *et al.* Feasibility of a visual prosthesis for the blind based on intracortical microstimulation of the visual cortex. *Brain* **119 (Pt 2)**, 507–522 (1996).
251. Maynard, E. M., Nordhausen, C. T. & Normann, R. A. The Utah Intracortical Electrode Array: A recording structure for potential brain-computer interfaces. *Electroencephalography and Clinical Neurophysiology* **102**, 228–239 (1997).
252. Margalit, E. *et al.* Retinal prosthesis for the blind. *Surv Ophthalmol* **47**, 335–356 (2002).
253. Maynard, E. M. Visual prostheses. *Annu Rev Biomed Eng* **3**, 145–168 (2001).
254. del Valle, J. & Navarro, X. Interfaces with the peripheral nerve for the control of neuroprostheses. *Int Rev Neurobiol* **109**, 63–83 (2013).
255. Reichert, W. M. *Indwelling Neural Implants: Strategies for Contending with the In Vivo Environment*. (CRC Press, 2007).
256. Hoffer, J. & Kallesoe, K. How to Use Nerve Cuffs to Stimulate, Record or Modulate Neural Activity. in *Neural Prostheses for Restoration of Sensory and Motor Function* (2000). doi:10.1201/9781420039054.ch5.
257. Tyler, D. J. & Durand, D. M. Functionally selective peripheral nerve stimulation with a flat interface nerve electrode. *IEEE Trans Neural Syst Rehabil Eng* **10**, 294–303 (2002).

258. Tyler, D. J. Chapter 20 - Electrodes for the Neural Interface. in *Neuromodulation (Second Edition)* (eds. Krames, E. S., Peckham, P. H. & Rezai, A. R.) 239–274 (Academic Press, 2018). doi:10.1016/B978-0-12-805353-9.00020-6.
259. Malagodi, M. S., Horch, K. W. & Schoenberg, A. A. An intrafascicular electrode for recording of action potentials in peripheral nerves. *Ann Biomed Eng* **17**, 397–410 (1989).
260. Lago, N., Yoshida, K., Koch, K. P. & Navarro, X. Assessment of Biocompatibility of Chronically Implanted Polyimide and Platinum Intrafascicular Electrodes. *IEEE Transactions on Biomedical Engineering* **54**, 281–290 (2007).
261. Boretius, T. *et al.* A transverse intrafascicular multichannel electrode (TIME) to interface with the peripheral nerve. *Biosensors and Bioelectronics* **26**, 62–69 (2010).
262. Badia, J., Raspopovic, S., Carpaneto, J., Micera, S. & Navarro, X. Spatial and Functional Selectivity of Peripheral Nerve Signal Recording With the Transversal Intrafascicular Multichannel Electrode (TIME). *IEEE Transactions on Neural Systems and Rehabilitation Engineering* **24**, 20–27 (2016).
263. Cutrone, A., Sergi, P. N., Bossi, S. & Micera, S. Modelization of a self-opening peripheral neural interface: A feasibility study. *Medical Engineering & Physics* **33**, 1254–1261 (2011).
264. Cutrone, A., Bossi, S. & Micera, S. Development of a Self-Opening Neural Interface. *Journal of Medical Devices* **7**, (2013).
265. Branner, A., Stein, R. B. & Normann, R. A. Selective stimulation of cat sciatic nerve using an array of varying-length microelectrodes. *J Neurophysiol* **85**, 1585–1594 (2001).
266. Wark, H. A. C. *et al.* A new high-density (25 electrodes/mm²) penetrating microelectrode array for recording and stimulating sub-millimeter neuroanatomical structures. *J. Neural Eng.* **10**, 045003 (2013).
267. Moshayedi, P. *et al.* The relationship between glial cell mechanosensitivity and foreign body reactions in the central nervous system. *Biomaterials* **35**, 3919–3925 (2014).
268. Christensen, M. B., Wark, H. A. C. & Hutchinson, D. T. A histological analysis of human median and ulnar nerves following implantation of Utah slanted electrode arrays. *Biomaterials* **77**, 235–242 (2016).
269. Wurth, S. *et al.* Long-term usability and bio-integration of polyimide-based intra-neural stimulating electrodes. *Biomaterials* **122**, 114–129 (2017).
270. Bourne, R. R. A. *et al.* Causes of vision loss worldwide, 1990-2010: a systematic analysis. *Lancet Glob Health* **1**, e339-349 (2013).
271. Brindley, G. S. & Lewin, W. S. The sensations produced by electrical stimulation of the visual cortex. *J Physiol* **196**, 479–493 (1968).
272. Dobbelle, W. H., Mladejovsky, M. G. & Girvin, J. P. Artificial vision for the blind: electrical stimulation of visual cortex offers hope for a functional prosthesis. *Science* **183**, 440–444 (1974).
273. Ghezzi, D. Retinal prostheses: progress toward the next generation implants. *Front Neurosci* **9**, 290 (2015).

274. da Cruz, L. *et al.* Five-Year Safety and Performance Results from the Argus II Retinal Prosthesis System Clinical Trial. *Ophthalmology* **123**, 2248–2254 (2016).
275. Ayton, L. N. *et al.* First-in-human trial of a novel suprachoroidal retinal prosthesis. *PLoS One* **9**, e115239 (2014).
276. Brelén, M. E., Vince, V., Gérard, B., Veraart, C. & Delbeke, J. Measurement of evoked potentials after electrical stimulation of the human optic nerve. *Invest Ophthalmol Vis Sci* **51**, 5351–5355 (2010).
277. Normann, R. A. *et al.* Toward the development of a cortically based visual neuroprosthesis. *J Neural Eng* **6**, 035001 (2009).
278. Merabet, L. B., Rizzo, J. F., Amedi, A., Somers, D. C. & Pascual-Leone, A. What blindness can tell us about seeing again: merging neuroplasticity and neuroprostheses. *Nat Rev Neurosci* **6**, 71–77 (2005).
279. Antognazza, M. R. *et al.* Shedding Light on Living Cells. *Adv Mater* **27**, 7662–7669 (2015).
280. Maya-Vetencourt, J. F. *et al.* A fully organic retinal prosthesis restores vision in a rat model of degenerative blindness. *Nat Mater* **16**, 681–689 (2017).
281. Antognazza, M. R. *et al.* Characterization of a Polymer-Based, Fully Organic Prosthesis for Implantation into the Subretinal Space of the Rat. *Adv Healthc Mater* **5**, 2271–2282 (2016).
282. Duret, F. *et al.* Object localization, discrimination, and grasping with the optic nerve visual prosthesis. *Restor Neurol Neurosci* **24**, 31–40 (2006).
283. Science, T. L. I. for I. in V. & Science, T. L. I. for I. in V. Chapter 1 - Restoring Vision to the Blind: The New Age of Implanted Visual Prostheses. *Trans. Vis. Sci. Tech.* **3**, 3–3 (2014).
284. Yan, Y. *et al.* Electrically Evoked Responses in the Rabbit Cortex Induced by Current Steering With Penetrating Optic Nerve Electrodes. *Invest Ophthalmol Vis Sci* **57**, 6327–6338 (2016).
285. Sun, J., Chen, Y., Chai, X., Ren, Q. & Li, L. Penetrating electrode stimulation of the rabbit optic nerve: parameters and effects on evoked cortical potentials. *Graefes Arch Clin Exp Ophthalmol* **251**, 2545–2554 (2013).
286. Raspopovic, S. *et al.* Restoring natural sensory feedback in real-time bidirectional hand prostheses. *Sci Transl Med* **6**, 222ra19 (2014).
287. Oddo, C. M. *et al.* Intra-neural stimulation elicits discrimination of textural features by artificial fingertip in intact and amputee humans. *Elife* **5**, e09148 (2016).
288. Raspopovic, S., Capogrosso, M., Badia, J., Navarro, X. & Micera, S. Experimental Validation of a Hybrid Computational Model for Selective Stimulation Using Transverse Intrafascicular Multichannel Electrodes. *IEEE Trans. Neural Syst. Rehabil. Eng.* **20**, 395–404 (2012).
289. Hukins, D. W. L., Mahomed, A. & Kukureka, S. N. Accelerated aging for testing polymeric biomaterials and medical devices. *Med Eng Phys* **30**, 1270–1274 (2008).
290. Howlader, M. M. R., Doyle, T. E., Mohtashami, S. & Kish, J. R. Charge transfer and stability of

- implantable electrodes on flexible substrate. *Sensors and Actuators B: Chemical* **178**, 132–139 (2013).
291. Giolli, R. A. & Guthrie, M. D. The primary optic projections in the rabbit. An experimental degeneration study. *J Comp Neurol* **136**, 99–126 (1969).
292. Delorme, A., Palmer, J., Onton, J., Oostenveld, R. & Makeig, S. Independent EEG sources are dipolar. *PLoS One* **7**, e30135 (2012).
293. Menicucci, D. *et al.* Brain responses to emotional stimuli during breath holding and hypoxia: an approach based on the independent component analysis. *Brain Topogr* **27**, 771–785 (2014).
294. Artoni, F. *et al.* Unidirectional brain to muscle connectivity reveals motor cortex control of leg muscles during stereotyped walking. *Neuroimage* **159**, 403–416 (2017).
295. Bell, A. J. & Sejnowski, T. J. An information-maximization approach to blind separation and blind deconvolution. *Neural Comput* **7**, 1129–1159 (1995).
296. Delbeke, J., Oozeer, M. & Veraart, C. Position, size and luminosity of phosphenes generated by direct optic nerve stimulation. *Vision Res* **43**, 1091–1102 (2003).
297. Li, M. *et al.* A simulation of current focusing and steering with penetrating optic nerve electrodes. *J Neural Eng* **10**, 066007 (2013).
298. Ghezzi, D. *et al.* A polymer optoelectronic interface restores light sensitivity in blind rat retinas. *Nat Photonics* **7**, 400–406 (2013).
299. Mathieson, K. *et al.* Photovoltaic Retinal Prosthesis with High Pixel Density. *Nat Photonics* **6**, 391–397 (2012).
300. Mandel, Y. *et al.* Cortical responses elicited by photovoltaic subretinal prostheses exhibit similarities to visually evoked potentials. *Nat Commun* **4**, 1980 (2013).
301. Tang, J. *et al.* Nanowire arrays restore vision in blind mice. *Nat Commun* **9**, 786 (2018).
302. Boinagrov, D., Pangratz-Fuehrer, S., Goetz, G. & Palanker, D. Selectivity of direct and network-mediated stimulation of the retinal ganglion cells with epi-, sub- and intraretinal electrodes. *J Neural Eng* **11**, 026008 (2014).
303. Weiland, J. D., Walston, S. T. & Humayun, M. S. Electrical Stimulation of the Retina to Produce Artificial Vision. *Annu Rev Vis Sci* **2**, 273–294 (2016).
304. Nirenberg, S. & Pandarinath, C. Retinal prosthetic strategy with the capacity to restore normal vision. *Proc Natl Acad Sci U S A* **109**, 15012–15017 (2012).
305. Piedade, M., Gerald, J., Sousa, L. A., Tavares, G. & Tomas, P. Visual neuroprosthesis: a non invasive system for stimulating the cortex. *IEEE Transactions on Circuits and Systems I: Regular Papers* **52**, 2648–2662 (2005).
306. Sieu, L.-A. *et al.* EEG and functional ultrasound imaging in mobile rats. *Nat Methods* **12**, 831–834 (2015).

307. Demene, C. *et al.* Functional ultrasound imaging of brain activity in human newborns. *Sci Transl Med* **9**, (2017).
308. Blaize, K. *et al.* Functional ultrasound imaging of deep visual cortex in awake nonhuman primates. *Proc Natl Acad Sci U S A* **117**, 14453–14463 (2020).
309. Artoni, F., Menicucci, D., Delorme, A., Makeig, S. & Micera, S. RELICA: a method for estimating the reliability of independent components. *Neuroimage* **103**, 391–400 (2014).
310. Goodall, E. V., Kosterman, L. M., Holsheimer, J. & Struijk, J. J. Modeling study of activation and propagation delays during stimulation of peripheral nerve fibers with a tripolar cuff electrode. *IEEE Transactions on Rehabilitation Engineering* **3**, 272–282 (1995).
311. Chintalacharuvu, R. R., Ksienski, D. A. & Mortimer, J. T. A Numerical Analysis Of The Electric Field Generated By A Nerve Cuff Electrode. in *Proceedings of the Annual International Conference of the IEEE Engineering in Medicine and Biology Society Volume 13: 1991* 912–913 (1991). doi:10.1109/IEMBS.1991.684258.
312. Struijk, J. J., Holsheimer, J., Barolat, G., He, J. & Boom, H. B. K. Paresthesia thresholds in spinal cord stimulation: a comparison of theoretical results with clinical data. *IEEE Transactions on Rehabilitation Engineering* **1**, 101–108 (1993).
313. Bossetti, C. A., Birdno, M. J. & Grill, W. M. Analysis of the quasi-static approximation for calculating potentials generated by neural stimulation. *J Neural Eng* **5**, 44–53 (2008).
314. McIntyre, C. C. & Grill, W. M. Extracellular stimulation of central neurons: influence of stimulus waveform and frequency on neuronal output. *J Neurophysiol* **88**, 1592–1604 (2002).
315. Raspopovic, S., Capogrosso, M. & Micera, S. A Computational Model for the Stimulation of Rat Sciatic Nerve Using a Transverse Intrafascicular Multichannel Electrode. *IEEE Trans. Neural Syst. Rehabil. Eng.* **19**, 333–344 (2011).
316. Oozeer, M., Veraart, C., Legat, V. & Delbeke, J. A model of the mammalian optic nerve fibre based on experimental data. *Vision Research* **46**, 2513–2524 (2006).
317. Prévot, P.-H. *et al.* Behavioural responses to a photovoltaic subretinal prosthesis implanted in non-human primates. *Nat Biomed Eng* **4**, 172–180 (2020).
318. Ronzani, C. *et al.* High-Frequency Stimulation of Normal and Blind Mouse Retinas Using TiO₂ Nanotubes. *Advanced Functional Materials* **28**, (2018).
319. Bloch, E., Luo, Y. & da Cruz, L. Advances in retinal prosthesis systems. *Ophthalmol Eye Dis* **11**, 251584141881750 (2019).
320. Ayton, L. N. *et al.* An update on retinal prostheses. *Clinical Neurophysiology* **131**, 1383–1398 (2020).
321. Mills, J. O., Jalil, A. & Stanga, P. E. Electronic retinal implants and artificial vision: journey and present. *Eye (Lond)* **31**, 1383–1398 (2017).
322. da Cruz, L. *et al.* The Argus II epiretinal prosthesis system allows letter and word reading and long-

- term function in patients with profound vision loss. *Br J Ophthalmol* **97**, 632–636 (2013).
323. Medeiros, N. E. & Curcio, C. A. Preservation of ganglion cell layer neurons in age-related macular degeneration. *Invest Ophthalmol Vis Sci* **42**, 795–803 (2001).
324. Gargini, C., Terzibasi, E., Mazzoni, F. & Strettoi, E. Retinal organization in the retinal degeneration 10 (rd10) mutant mouse: a morphological and ERG study. *J Comp Neurol* **500**, 222–238 (2007).
325. Mazzoni, F., Novelli, E. & Strettoi, E. Retinal Ganglion Cells Survive and Maintain Normal Dendritic Morphology in a Mouse Model of Inherited Photoreceptor Degeneration. *J. Neurosci.* **28**, 14282–14292 (2008).
326. Jones, B. W. & Marc, R. E. Retinal remodeling during retinal degeneration. *Exp Eye Res* **81**, 123–137 (2005).
327. Margolis, D. & Detwiler, P. Cellular Origin of Spontaneous Ganglion Cell Spike Activity in Animal Models of Retinitis Pigmentosa. *Journal of ophthalmology* **2011**, (2011).
328. Goetz, G. A. & Palanker, D. V. Electronic approaches to restoration of sight. *Rep Prog Phys* **79**, 096701 (2016).
329. Chenais, N. A. L., Airaghi Leccardi, M. J. I. & Ghezzi, D. Naturalistic spatiotemporal modulation of epiretinal stimulation increases the response persistence of retinal ganglion cell. *J Neural Eng* (2020) doi:10.1088/1741-2552/abcd6f.
330. Fang, X. *et al.* Electrophysiological and histological studies of chronically implanted intrapapillary microelectrodes in rabbit eyes. *Graefes Arch Clin Exp Ophthalmol* **244**, 364–375 (2006).
331. Fang, X. *et al.* Direct stimulation of optic nerve by electrodes implanted in optic disc of rabbit eyes. *Graefes Arch Clin Exp Ophthalmol* **243**, 49–56 (2005).
332. Cha, K., Horch, K. W. & Normann, R. A. Mobility performance with a pixelized vision system. *Vision Res* **32**, 1367–1372 (1992).
333. Thorn, J. T., Migliorini, E. & Ghezzi, D. Virtual reality simulation of epiretinal stimulation highlights the relevance of the visual angle in prosthetic vision. *J Neural Eng* **17**, 056019 (2020).
334. Lohmann, T. K. *et al.* The very large electrode array for retinal stimulation (VLARS)-A concept study. *J Neural Eng* **16**, 066031 (2019).
335. Chenais, N., Airaghi Leccardi, M. & Ghezzi, D. *Single-pixel epiretinal stimulation with a wide-field and high-density retinal prosthesis for artificial vision.* (2020). doi:10.1101/2020.08.21.261461.
336. Gaillet, V. *et al.* Spatially selective activation of the visual cortex via intraneural stimulation of the optic nerve. *Nature Biomedical Engineering* **4**, 181–194 (2020).
337. Dubey, A. & Ray, S. Cortical Electrocorticogram (ECoG) Is a Local Signal. *J Neurosci* **39**, 4299–4311 (2019).
338. Fischer, B., Schander, A., Kreiter, A. K., Lang, W. & Wegener, D. Visual epidural field potentials possess

- high functional specificity in single trials. *Journal of Neurophysiology* **122**, 1634–1648 (2019).
339. Thompson, J. M., Woolsey, C. N. & Talbot, S. A. Visual areas i and ii of cerebral cortex of rabbit. *Journal of Neurophysiology* **13**, 277–288 (1950).
340. Choudhury, B. P. Visual cortex in the albino rabbit. *Exp Brain Res* **66**, 565–571 (1987).
341. Wong, Y. T. *et al.* Spectral distribution of local field potential responses to electrical stimulation of the retina. *J Neural Eng* **13**, 036003 (2016).
342. Luo, Y. H.-L. & da Cruz, L. The Argus(®) II Retinal Prosthesis System. *Prog Retin Eye Res* **50**, 89–107 (2016).
343. Fornos, A. P., Sommerhalder, J., Rappaz, B., Safran, A. B. & Pelizzone, M. Simulation of Artificial Vision, III: Do the Spatial or Temporal Characteristics of Stimulus Pixelization Really Matter? *Invest. Ophthalmol. Vis. Sci.* **46**, 3906–3912 (2005).
344. Jung, J.-H., Aloni, D., Yitzhaky, Y. & Peli, E. Active confocal imaging for visual prostheses. *Vision Research* **111**, 182–196 (2015).
345. Li, Y. *et al.* Long-term safety and efficacy of human-induced pluripotent stem cell (iPS) grafts in a preclinical model of retinitis pigmentosa. *Mol Med* **18**, 1312–1319 (2012).
346. Bassuk, A. G., Zheng, A., Li, Y., Tsang, S. H. & Mahajan, V. B. Precision Medicine: Genetic Repair of Retinitis Pigmentosa in Patient-Derived Stem Cells. *Scientific Reports* **6**, 19969 (2016).
347. Latella, M. C. *et al.* In vivo Editing of the Human Mutant Rhodopsin Gene by Electroporation of Plasmid-based CRISPR/Cas9 in the Mouse Retina. *Mol Ther Nucleic Acids* **5**, e389 (2016).
348. Yu, W. *et al.* Nr1 knockdown by AAV-delivered CRISPR/Cas9 prevents retinal degeneration in mice. *Nature Communications* **8**, 14716 (2017).
349. Moreno, A. M. *et al.* In Situ Gene Therapy via AAV-CRISPR-Cas9-Mediated Targeted Gene Regulation. *Mol Ther* **26**, 1818–1827 (2018).
350. Vagni, P. *et al.* Gene Editing Preserves Visual Functions in a Mouse Model of Retinal Degeneration. *Front Neurosci* **13**, (2019).

Curriculum Vitae

Vivien Gaillet

30 years old • Swiss

Mobile: 079/961 77 08 • Email: vi.gaillet@gmail.com

Address: Avenue du Rond-Point 1B, 1006 Lausanne (VD), Switzerland

EDUCATION AND TRAINING

- 10.2016 – 04.2021 **PhD, Electrical engineering**
Campus Biotech Genève
- 09.2013 – 08.2015 **Master in Bioengineering, regenerative medicine track**
EPFL Lausanne
- 08.2010 – 07.2013 **Bachelor in life sciences and technology**
EPFL Lausanne
- 10.2009 – 03.2010 **Sanitary soldier & Red-Cross health auxiliary**
École de recrue SAN42, Airolo
- 08.2006 – 07.2009 **“Maturité gymnasiale” in biology-chemistry option**
Gymnase intercantonal de la Broye, Payerne

PROJECTS AND INTERNSHIPS

- 02.2015 – 08.2015 **Master Thesis: Design and optimization of a hydrogel for bowel tissue engineering, Institute of Child Health, University College London**
This project involved tissue decellularization and sterilization, tissue stainings, proteins and biomolecules component quantification, spectrometry and rheological analysis.
- 09.2014 – 12.2014 **Lab Immersion: Epidural electrical stimulation of the spinal cord in spinal rats Translational neural engineering lab, EPFL Lausanne**
This project involved Matlab and LabVIEW programming, animal care, locomotion analysis, acute and chronic animal experiments, and COMSOL and NEURON softwares handling.
- 02.2014 – 06.2014 **Semester Project: Influence of poly-Q length on the Huntingtin aggregation dynamic, Lab of molecular and chemical biology of neurodegeneration, EPFL Lausanne.**

This project involved protein production and purification, peptide synthesis and ligation, UPLC analysis, and mass spectrometer and electrical microscope handling.
- 07.2013 – 09.2013 **Internship in CHUV: Analysis of functional MRI data for new drug validation in ADHD treatment, CHUV Lausanne**

This project involved MRI data treatment and analysis, Matlab scripting, and statistical analysis.

- 02.2013 – 07.2013 **Bachelor Project: 3D-protein structure reconstruction using evolutionary inferred correlations**
Laboratory of biomolecular modeling, EPFL Lausanne
 This project involved different sequencing and proteomic softwares handling and Matlab programming.

WORK EXPERIENCE

- 07.2016 – 08.2016 **Internship in Volumina: *In vitro* and *in ovo* experiments for the validation of a new hydrogel**
 Volumina start-up, LMIS4 laboratory, EPFL Lausanne
- 10.2015 – 01.2016 **Service civil: Analysis of the long-term implantation of an electrical stimulating device**
 Chair in spinal cord repair, EPFL Lausanne
- 08.2014 – 10.2014 **Scientific literature review for Dorphan start-up**
 Innovation Park, EPFL Lausanne
- 09.2014 – 12.2014 **Teaching assistant in Analysis I and II (mathematics)**
 09.2012 – 07.2013 EPFL Lausanne
- 03.2012 – 05.2012 **Substitute teacher in mathematics**
 Secondary school of Payerne

PERSONAL SKILLS AND COMPETENCES

Languages

French: first language • German: B1 • English: C1-
 C2

IT skills

Matlab • C++

LIST OF PUBLICATIONS

Gaillet, V., Cutrone, A., Artoni, F. et al. Spatially selective activation of the visual cortex via intraneural stimulation of the optic nerve. *Nat Biomed Eng* 4, 181–194 (2020). <https://doi.org/10.1038/s41551-019-0446-8>

Gaillet, V., et al. A machine-learning algorithm correctly classifies cortical evoked potentials from both natural retinal stimulation and electrical stimulation of the optic nerve. Accepted in the *Journal of Neural Engineering*.